NTNU

Norwegian University of
Science and Technology

Oedometer Tests for Assessing Possible Impact of Fluid-Shale Interactions on a Shale Barrier Formation

Celine Marie Knudtzon Brun-Lie

Petroleum Geoscience and Engineering
Submission date: July 2017
Supervisor: Rune Martin Holt, IGP

Norwegian University of Science and Technology
Department of Geoscience and Petroleum

Preface

This Master Thesis marks the closing of five years of studying within the field of Petroleum Engineering and Applied Geophysics at the Norwegian University of Science and Technology. The report was written in the spring 2017 in cooperation with SINTEF Petroleum Research, which has provided equipment and facilities for the experiment, as well as guidance on this relevant topic.

The report consists of a short literature review and several experiments within shale as a barrier. A more thorough literature study was done for the associated Specialization Project in the Fall 2016 (Brun-Lie, 2016). It is assumed that the reader has some knowledge of basic concepts within the petroleum industry.

I would like to thank my supervisor Rune Martin Holt for the help writing this thesis and good conversations conserning this topic. I would also like to thank Jørn Stenebråten at SINTEF Petroleum for all the help with the preparations and execution of the work in the laboratory. Erling Fjær, Idar Larsen, Sigurd Bakheim and Eyvind Sønstebø from SINTEF Petroleum also deserve gratitude for help and council during my work in the laboratory.

Celine Brun-Lie

Trondheim, July 2017

Introduction

At the end of a well's lifetime, the hole must be permanently plugged and abandoned (PP&A). Regulations require that the annulus is properly sealed off so that no migration of hydrocarbons to the surface will occur at any time in the future. Under operation, a well is generally sealed off by pumping cement through the casing shoe and up to a certain length of the annulus. However, when permanently plugging and abandoning a well, stricter requirements apply to make sure the well will not leak at any time in the future.

Through the NORSOK Standard for plug and abandonment (P&A), Norwegian authorities have outlined requirements for sealing barriers in P&As on the Norwegian Continental Shelf (NCS). A minimum of two independent barriers in addition to the surface/environmental barrier must be in place, requiring a full cross-sectional barrier also for the annulus. To be qualified as a barrier, the material in use must have specific characteristics. These requirements make the operation both costly and time-consuming. More than 3000 existing wells on the NCS, in addition to new wells drilled in the future, are to be plugged and abandoned in the near future. By using the existing technology, it has been estimated that 15 rigs will be needed for approximately 40 years of full time operation in order to meet the NORSOK Standard (Straume, 2014).

Due to these prospects there has recently been a focus on further developing the existing standard procedures for PP&A. Attention has been drawn towards shale in sections where the annulus is not filled with cement. In several cases, shale formations have moved towards the casing and created a natural barrier. As shales are known to be a good, impermeable cap rock for reservoirs, it is possible that such shale barriers are even more efficient than cement barriers. Cement tends to deteriorate over time, possibly causing older wells to leak (Lashkaripour and Dusseault, 1993). This indicates that shales could be a better long term alternative than cement. This natural sealing process could also eliminate a significant portion of work involved in creating an artificial permanent barrier, resulting in enormous cost savings while minimizing the environmental impact.

It is believed that this self-sealing effect can potentially fulfil the PP&A requirements for a barrier, as the rock meets all the requirements of NORSOK Standard. It is not yet well understood what mechanisms generate such shale barriers or what can be done to stimulate the creation of a barrier when it does not occur naturally.

Several studies have been outlined in recent years and the time-delayed deformation of the shale is most likely related to consolidation and creep (Williams et al., 2009).

The objective of this Master thesis has been to investigate a specific shale that has been proven to creep in the field. At the request of the company providing the shale material it has been decided that the shale in focus should be held confidential. It will from now on be referred to as "the shale", "the sample" or "the material". In cooperation with the Norwegian University of Science and Technology (NTNU) and SINTEF Petroleum, experiments have been conducted using a dead weight frame and an oedometer cylinder to simulate creep while an axial stress was applied to the sample within the cylinder. Several parameters were recorded and a special focus was put in the investigation of the change in acoustic responses when load was added, as well as the deformation rate when different circulations of fluids were used. A Micro CT Scan of each sample was also done in order to quantify the samples heterogeneity and to detect potential natural and induced fractures.

The study revealed that KCl fractured the material more under axial stress than NaCl and fresh water. All samples went through transient creep, reaching steady state creep in the very end of each test. The permeability of each sample was reduced as a result of fluid exposure and axial stress. Each sample swelled in the beginning of each test, but the samples exposed to NaCl and KCl started to shrink after a while. The sample exposed to fresh water showed continuous swelling. The ultrasound measurements showed good correlation with the triaxial measurements, confirming the stepwise compaction of the samples. An S-wave may have been found for the samples exposed to KCl and fresh water but it is debatable.

In the fall 2016, a specialization project (Brun-Lie, 2016) on the same topic as this thesis was done by the same author. It was done as a preparation for this thesis to get familiar with the principles of creep and with the experiment procedures. Parts of the work done in the specialization project will be included in this report, either directly copied or as modified sections.

Sammendrag

Denne master oppgaven ble gjennomført som en del av prosjektet "Skifer som Barriere". Når en brønn har produsert ferdig og skal forlates, må den plugges permanent (PP&A). Strenge forskrifter krever at annulusen er ordentlig forseglet slik at ingen migrasjon av karbohydrater til overflaten vil skje på noe tidspunkt i fremtiden. Norske myndigheter har gjennom NORSOK Standards for plugging og forlating (P&A) av brønner bestemt at et minimum av to uavhengige barrierer, i tillegg til overflate/miljø barrieren, må være på plass. Disse kravene gjør at prosessen er både dyr og tidkrevende. Med dagens teknologi har det blitt estimert at 15 fulltidsopererende rigger vil bruke 40 år på å plugge eksisterende brønner på den Norske Kontinental Sokkelen (Straume, 2014). På grunn av disse framtidsutsiktene har det i senere tid blitt rettet mer fokus på seksjoner i annulusen som ikke er fylt med sement, der skifer har beveget seg mot casingen og dannet en naturlig barriere. Flere studier er blitt utført og indikerer at den forsinkede deformasjonsprosessen mest sannsynlig er relatert til konsolidering og kryp (Williams et al., 2009).

Tre triaksielle tester med forskjellige fluider (3.5% NaCl, 20% KCl of ferskvann) ble gjennomført for å se hvordan et skifermateriale oppførte seg når aksiell spenning ble påført. De forskjellige fluidene ble brukt for å se hvordan materialet ville oppføre seg forskjellig til forskjellig fluider. Aksiell deformasjon, radielt stress, temperatur og trykktestmålinger ble utført for å kvalifiser og kvantifisere oppførselen til materialet. Ultralyd var også koblet til oppsettet for å se om eksisterende logging verktøy kan bli brukt for å evaluere naturlige barrierer.

De største funnene fra eksperimentene som ble utført i denne masteroppgaven viser at skifermaterialet som ble testet kryper når det blir utsatt for NaCl, KCl og ferskvann. Mer aksiell spenning må til for at prøven utsatt for NaCl og KCl skal krype enn for prøven utsatt for ferskvann. Prøven som ble utsatt for KCl viser flere brudd etter testing enn de to andre prøvene. Permeabiliteten for hver prøve synker når de blir utsatt for aksiell spenning og fluider, men prøven utsatt for NaCl viser en høyere sluttpermeabilitet enn de to andre prøvene. Ultralyd målingene bekrefter resultatene funnet i de triaksielle testene og kan brukes til å se om det er kontakt mellom skiferen og casingen. P-bølgehastigheten fra prøven utsatt for KCl er høyere enn for de to andre prøvene. En S-bølge ble sannsynligvis funnet for to av testene. Noen elastiske egenskaper kan bli funnet på bakgrunn av hastighetsanalyser men vanskeligheten i å lokalisere S-bølgen kompliserer utregningene.

Contents

List of Figures

List of Tables

Chapter 1

Shale as a Barrier

The oil and gas industry is one of the most important industries in our lifetime. Human kind is dependent on the oil that is produced and the industry plays a huge economical role in societies throughout the world.

In order to define safe economical design and processes in the petroleum industry, International (ISO/IEC) and European standards (CEN/CENELEC) have been developed. They form a basis for all petroleum activities, and Norwegian companies participate heavily in this development. However, due to the climate conditions and safety framework on the Norwegian Continental Shelf (NCS), additional and supplementary standards to the ISO and CEN have been required (Industry, 2004). Therefore, the NORSOK standards have been developed to improve international standards by ensuring adequate safety, value adding and cost effectiveness for existing and future developments in Norway.

Chapter 9 of NORSOK D-010 (drilling) describes the requirements for permanent well barriers during sidetrack, suspension and abandonment operations. The permanent well barriers must extend across the full cross-section of the well so that it seals both horizontally and vertically. Operators can choose any barrier material as long as its properties meet all the requirements (Williams et al., 2009):

- Impermeable
- Long term integrity
- Non shrinking

- Ductile (non brittle) able to withstand mechanical loads/impact
- Resistance to different chemicals/substances (H2S, CO2 and hydrocarbons)
- Wetting, to ensure bonding to steel

Cement has traditionally been used to permanently seal the annulus. This is a time consuming and costly operation and recently a new focus has been put in the research for better technology to save both time and money. One approach that has caught interest and is accepted as a potential barrier is the use of the pre-existing shale. Shale makes up between 50-75% of the geological column (Kristiansen, 2015), which makes it a very attractive alternative to the conventional methods. For a shale to be qualified, the following requirements must be satisfied (Williams et al., 2009):

- The barrier must be proved shale through electrical logs or cutting description logs
- The maximum expected pressure that could apply to the rock must be the required strength of the rock, it is thus important that the maximum reservoir pressure that could be exerted on the barrier is not higher than the maximum horizontal stress, σ_H
- The displacement mechanism of the shale must be suitable to preserve the well barrier properties
- The barrier must extend and seal over the full circumference of the casing and over a suitable interval along the well, which can be verified using wireline ultrasonic bond logging tools

For a formation to act as a good barrier, it must have certain physical properties. Such properties include sufficient rock strength and extremely low permeability to fluids. Shale is believed to meet the characteristics to generate a self-sealing barrier, but it is important to understand its properties to be able to investigate how they may affect the self-sealing process. The shales displacement mechanisms are also important to investigate. Fjær et al. (2016) found that the best candidates are shales with a high ability to sustain large plastic deformations and with a low threshold for plastic flow. These topics were explored in the authors work "Shale as Barrier: Literature Study and Initial Laboratory Experiments on Sele Formation" in the fall of 2016 and will be partially rendered in the following sections.

1.1 Shale Properties

Shale is classified as a mudstone, and is the most common sedimentary rock on earth. The framework is composed of approximately 40% clay minerals, in combination with microscopic fragments of minerals like quartz and calcite (Table 1.1). Shales can be described as a fine-grained, clastic sedimentary rock. The clay and silt minerals are naturally occurring sediments produced by the decomposition of various rocks through weathering and chemical decomposition. Types of shales differ widely in purity and composition but essentially consist of silica, alumina or magnesia, or both, and water (Weems, 1903).

Mineral	**Average Content (%)**
Clay	39
Quartz	37
Feldspar	7.3
Carbonate	8.9
Pyrite	3.2

Table 1.1: Average mineral content of shales (Modified from Weems (1903))

1.1.1 Clay structure

Chemically, clay minerals are hydrous aluminum silicates that are composed of tetrahedral and octahedral silicate sheets, as shown in Figure 1.1. Together they create layers, where two or more layers are intermixed in vertical stacking sequences within a single crystal. The bonding is strong within each layer but it is weak in between them. Clay can have different combinations of minerals (Weems, 1903), and they generally become plastic when wet (UCL, 2017).

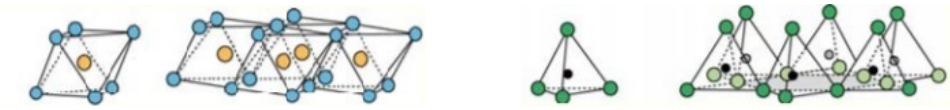

(a) Octahedral sheet (b) Tetrahedral sheet

Figure 1.1: Building blocks of clay minerals (Modified from (Eslinger and Pevear, 1988))

The most common clay minerals in shales are smectite, kaolinite, illite and chlorite. Kaolinite has the most basic structure with only one tetrahedral and one octahedral

sheet linked together (Figure 1.2). Illite is composed of two tetrahedral sheets and one octahedral sheet, linked together in a sandwich-like structure. Potassium (K) acts as glue that connects the layers. Smectite and chlorite have the same sandwich-structure, but with water and an octaherdal sheet linking the layers together.

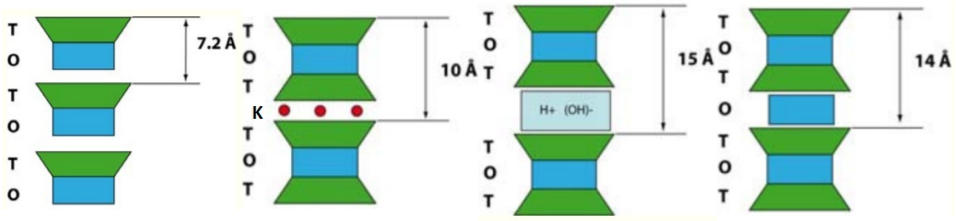

(a) Kaolinite (b) Illite (c) Smectite (d) Chlorite

Figure 1.2: Building blocks of clay minerals (Modified from Eslinger and Pevear (1988))

1.1.2 Clay Hydration

Depending on the composition of the shale, it may swell or shrink when exposed to different brines. During drilling, shale swelling causes problems like reduction in wellbore diameter and disintegration of shales. A lot of research has been done on this topic as borehole collapse is very costly for the oil industry.

Swelling, or clay hydration, is an increase in surface volume that occurs when the pore fluid chemistry changes or the confining stress is below the swelling pressure (Lyu et al., 2015). The clay minerals absorb water as the negative surface charge on the clay platelets attracts the water molecules that are dipolar. Different clay minerals have different degrees of swelling, meaning the composition of the shale decides how much water it will absorb, as well as the concentration of the salinity of the brine exposed (Sønstebø and Holt, 2001). Since clay minerals have a special platelet structure it is very common to have hydration in shales.

Different theories have been presented when describing swelling and shrinking in shales. The theory of osmosis is generally believed to explain the chemically induced instabilities by the existence of a semi-permeable membrane that rejects ionic flow but permits water flow between two regions. Shale is believed to act as a semi-permeable membranes (Schlemmer et al., 2003). It is thought that some shales may

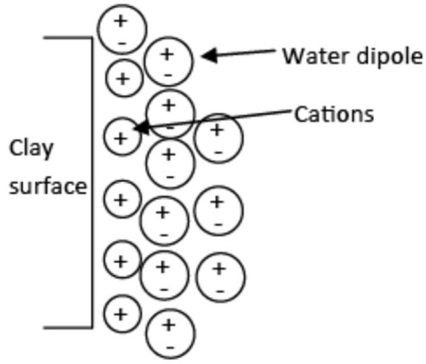

Figure 1.3: Clay hydration: water adsorption by ion hydration

absorb water from the drilling fluid if the chemical potential of the drilling fluid is higher than the fluid within the pore fluid of the shale (Sherwood and Bailey, 1994). Low mud activity generally means high salinity. Water may then be sucked out of the shale to create a chemical equilibrium. This reaction results in a decrease in pore pressure near the borehole wall and has a stabilizing effect.

It is uncertain, however, if the shale actually acts as a semi-permeable membrane. Ions often move through shale at almost the same rate as water (Sønstebø and Holt, 2001). Membrane efficiency is therefore introduced to the calculation of the osmotic potential to compensate for the efficiency of the membrane. If the efficiency is very low, for example when ionic interaction happen with the shale, the concept of osmosis becomes insufficient.

According to Ballard et al. (1994), there are two main mechanisms by which fluid can pass into the rock matrix: diffusion and advection. Diffusion results from thermal agitation of the water molecules and is independent of pressure. Advection on the other hand occurs when enough pressure is applied to create flow. Unlike diffusion, advection may result in actual mass flow.

Smectite is characteristic for its ability to absorb water and swell (Dusseault, 2011a). This is due to strong attractive forces of polar molecules that force themselves in between the silicate layers. This swelling is possible as the connection between the individual layers is very weak (Weems, 1903). These weak layers may sometimes have the ability to strongly modify the flow behaviour of liquids (Odom, 1984). Kaolinite, in contrast to smectite, has a strong connection between the individual layers that effectively prevents fluid from entering in between them. Illite

has a stronger bonding than smectite, which prevents hydration, but has weaker bonds than the kaolinite. Chlorite has very strong bonds resulting in no swelling (Skjerve, 2013).

1.1.3 Anisotropy

Shales have different degrees of anisotropy and strength due to a range of different factors. This anisotropy and strength can vary due to differences in depositional environment, deformation history, degree of cementation and the amount of non-clay minerals present. In general, shale structures are strongly anisotropic due to their plate-like structure (Fjær et al., 2008). This can often be seen through a plane of weakness. It is along this plane of weakness that the shale can easily separate and break apart.

Since shales contain water that is structurally bounded, it is often difficult to measure the elastic properties of the solid material it contains. The different degree of swelling greatly affects the rock strength. For example shales with low smectite content are generally more brittle than those with high smectite content. Increased percentage of smectite by volume enhances the plastic behaviour of a shale as it bounds more water molecules in its structure (UCL, 2017).

The small particle size of the clay generally results in an extremely good compaction. Due to the way the clay minerals are compacted, shales generally have very low permeability. Ultimately this results in small pore sizes but the porosity may vary from very small to quite high (a few % up to 70%) (Fjær et al., 2008). Shales have very large specific surface areas that are negatively charged and attract cations from the pore water. This large surface area results in the attachment of hydrated ions to the mineral surface.

1.2 Displacement Mechanisms

The self-sealing deformation of shales is known to have occurred in several parts of the world. Diameters in specific zones of the wells have been observed to shrink during rapid or slow processes, indicating that the formation behind the casing has deformed. Several displacement mechanisms are believed to occur in this process.

According to Williams et al. (2009) the displacement mechanisms are most likely related to:

- Thermal expansion
- Chemical Effects
- Shear or tensile failure
- Compaction failure
- Creep and Consolidation

These mechanisms were studied more thoroughly during the associated Specialization Project (Brun-Lie, 2016) and can be found in Appendix A. Based on these mechanisms, creep is believed to best describe the observations of diameter reduction in the wellbores (Williams et al., 2009). Therefore creep will be more thoroughly described here.

Consolidation and creep are time-dependent deformation, meaning the deformation of the rock may occur long after the change in stress state occurred (Fjær et al., 2008). It is sometimes difficult to separate the two effects. While consolidation is related to pore pressure diffusion, creep is a consequence of viscoelastic processes in the formations framework.

Creep

Creep is a time-dependent deformation that occurs in materials under constant stress. It is related to visco-elastic behaviour in the solid framework, meaning it can occur in both saturated and dry rocks (Fjær et al., 2008). Creep is defined as an irreversible deformation in time without fracturing. It is mainly observed in soft rocks like salt and coal, but occur in all rocks given appropriate amount of time (Cristescu and Hunsche, 1998).

While drilling, creep is usually seen as a negative deformation, as it may cause borehole collapse. To keep a hole stable, a drilling mud with a certain density is used to equalize the pressure. This is to maintain stability in the borehole. If the mud weight is kept marginally above the lower limit of stability for a long time, a material may be brought to its yield point. If this is the case the material may creep to failure and as a result the borehole may collapse (Fjær et al., 2008).

However, creep of shale may work to an economic and environmental advantage. If the displacement mechanism is kept under control during drilling and then initiated after the casing is in place, it may create a natural barrier that is very beneficial for future operations. It would reduce the amount of cement jobs that needs to be done and the time saved would result in great cost savings. It would also have a positive environmental impact. Since the operations involving cement jobs would not be necessary the risk of cement spill will be eliminated, along with other potential unforeseen effects of using cement as a barrier.

As creep is suggested to be the deformation process that best describes the hydraulic way a shale formation is thought to be moving (Williams et al., 2009), the deformation process will be described in greater detail.

Stages of Creep

Both experimental results and those from material sciences provide an important foundation in the description of creep. To best describe the creep phenomena, creep has been divided into three stages: transient creep, steady state creep and acceleration creep. A more thorough description is given below:

- **Transient (primary) creep**:
  In this primary stage, the rate of deformation decreases with time. Hardening and recovery are not in equilibrium, meaning the rate of creep varies with time (Cristescu and Hunsche, 1998). The rock tends to behave elastically, as the deformation eventually will decrease to zero if the applied stress ends during this primary stage. If this is the case, the deformation process will not move into the two following stages of creep, as the material returns to its original state. There might be a minor spreading of "stable" microfractures at a decreasing rate (Fjær et al., 2008).

- **Steady state (secondary) creep:**
  This secondary stage happens when the loading conditions are kept constant and the deformation rate approaches a constant positive value (Cristescu and Hunsche, 1998). In this case, hardening of the rock is in equilibrium with the recovery. This implies a permanent deformation of the material. If the applied stress ends during this stage, the deformation will not vanish completely unlike during the transient phase. As a result the material will have permanently deformed. The behaviour is therefore said to be inelastic.

- **Acceleration (tertiary) state:**
  The tertiary stage comes after secondary creep or directly after primary creep (Cristescu and Hunsche, 1998). The rate of deformation increases with time, the material has increasing damage and it ends with creep rupture. The process is associated with rapid spreading of "unstable" fractures, meaning the rock will eventually fail.

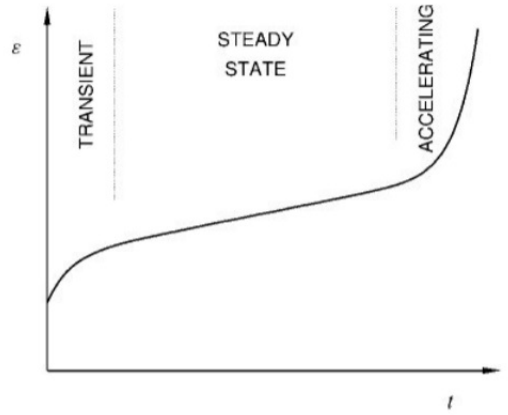

Figure 1.4: Stages of creep (Modified from Fjær et al. (2008))

Figure 1.4 shows the relationship between strain and time for a material that is under constant stress. The curve is characteristic for its S-shape that can be divided into the three stages of creep. There is an initial increase in strain when load is applied, before the strain stabilizes. At the end it reaches failure and the strain increases fast.

The magnitude of the applied stress regime defines the actual behaviour of creep in a rock (Figure 1.5). For low and moderate stresses, the rock may stabilize after the transient creep stage. When high stresses are applied, the rock might go through all stages of creep rapidly and cause failure (Fjær et al., 2008). In cases with intermediate stress regimes, each stage of creep might vary over a wide range of time, and are therefore difficult to identify individually.

The fact that creep is a molecular process and that the time scale depends on temperature, means that the process generally speeds up when the temperature increases (Fjær et al., 2008). As even steady state creep eventually results in failure, it suggests that formations that are loaded with a weight below its ultimate

strength may fail if the load is maintained over a longer period of time.

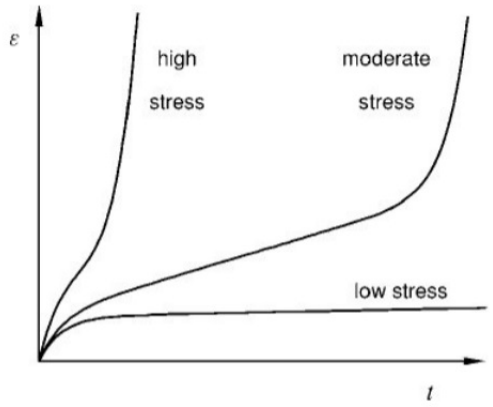

Figure 1.5: Creep development for different applied stresses (Modified from Fjær et al. (2008))

1.3 Laboratory testing of shales

Direct measurements of static mechanical parameters and rock strength are generally conducted in the laboratory by using cores (Xu et al., 2016). Unfortunately, cores are expensive and time consuming to retrieve and are only available from specific areas of the well which may just represent the formation in and near the borehole. In general, it is important to have a thorough coring plan that addresses its objectives and the handling of the samples (STEP and API, 1998).

Although not to the same extent as other sedimentary rocks, studies of shales have been made related to top seal evaluation and overburden prediction, as well as wellbore stability. In recent years, more studies have been carried out on shales in relation to unconventional reservoirs (Josh et al., 2012).

Due to its low permeability, shales have slow pore pressure equilibrium. This means that shale is an extremely time-consuming rock to test mechanically in the laboratory. Furthermore, cores taken out of the earth will not give a perfect representation of the *in situ* shale. Tensile failure occurring during core retrieval will damage the samples, and temperature, stress distribution and pore pressure, among others, will not be the same in the atmosphere as in the lithosphere. According to Fjær et al. (2008), the best results in the laboratory are obtained when the pore

pressure is enforced, or measured, as a response to applied stress.

Lashkaripour and Dusseault (1993) found that shales unconfined strength increases with decreasing porosity, and suggested the following relationship:

$$C_0 = 193\phi^{-1.14} \tag{1.1}$$

where C_0 is the unconfined strength in MPa and ϕ is the porosity given in %. The majority of shale porosity tested in their study were below 20%. They formulated a relationship between strength and stiffness, resulting in the ratio $\frac{E}{C_0}$, where E is the Young's modulus and C_0 the unconfined strength.

Horsrud (2001) studied shales from the North Sea. Although the results showed that the porosity measurements were higher in this area than in the area Lashkaripour and Dusseault (1993) studied (between $30 - 55\%$) he confirmed a proportionality between Young's modulus and unconfined strength. Both studies show that the P-wave velocity measurements have a good correlation with shale strength. This is important in the way that sonic measurements for both log and seismic data thus can be related to shale strength. Horsrud (2001) developed the relationship:

$$C_0 = 0.77v_p^{2.93} \tag{1.2}$$

for the unconfined strength, where v_p is the P-wave velocity given in km/s.

In the Mohr-Coulomb failure criterion, the failure angle *beta* is a required parameter to complete the stability evaluation. As good correlations between failure angle and other parameters have not yet been established, trends have been found. Although poor estimates, failure angle seems to increase with shale strength and P-wave velocity while it seems to decrease with increasing clay-mineral content (Horsrud, 2001). Thus, when porosity and fluid content decreases when compaction and consolidation takes place, the shale develops a greater failure angle. According to Horsrud (2001), the failure angle in most tests with high porosity shale is very low, typically $10° - 20°$.

Chapter 2

Acoustic Application

Cement is used during several operations in a well, for example to prevent migration of fluids in the annulus. To qualify the cement job, cement evaluations have to be done. One of the primary ways to determine if a cement job has been successful or not is the use of wireline tools (Tiomin et al., 2014). The wirelines have acoustic logging which today is the most efficient and widely used method when evaluating cement jobs (Allouche et al., 2005). Generally, these wirelines send out pulses of different frequencies to measure the bond between the casing and the material behind it in the annulus.

Several logging techniques are currently available for measuring the cement quality and there is a strong drive from both academia and industry to see if some of these techniques can be used to qualify the sealing ability of shale. In the situation where the formation wall lies against the casing, the wave signal received will be different from the ones received from contact with cement, mud or casing (DeBruijn et al., 2016). This would therefore be a good indication as to whether there is contact or not between a formation and the casing. Unfortunately, not many studies have been done regarding this topic, but the recent interest has enhanced the demand for such studies.

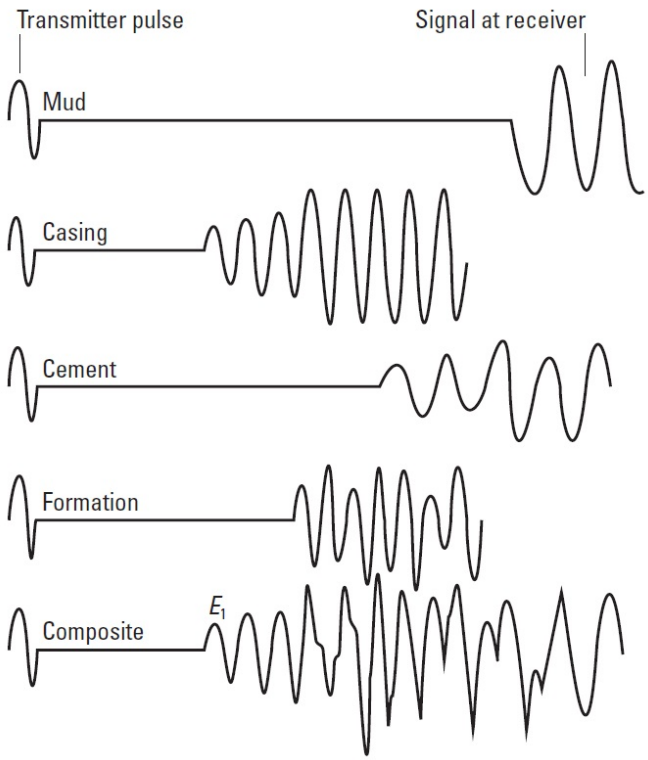

Figure 2.1: Examples of sonic wave paths (Modified from Allouche et al. (2005))

Through acoustic log interpretation in the field it is possible to relate the tool response with the material behind the casing. The response varies with the acoustic properties of the surrounding environment (Figure 2.1) and so does the quality of the acoustic coupling between the casing and material behind (Allouche et al., 2005). According to Holt et al. (1996), acoustic measurement techniques have also proven to monitor ionic diffusion. This indicates that a change in measured velocities resulting from fluid exposure may be indicative of mechanical property changes of the material.

The experiments in this project were done to simulate shale creep and to see how the shale behaves under different stress conditions as well as different fluid exposures. Ultrasonic measurements were done for each test to see how the responses changed. The process was carried out to see if the method was applicable for qualifying contact between the shale and the casing, which in this case was a oedometer cylinder.

To be able to fully interpret the acoustic logs it is important to perform the analysis carefully. Several parameters can affect the log response. The next section will give a short description of the basic acoustic theory and how it can be related to the elastic properties of a material.

2.1 Acoustic Properties

In logging, acoustics relate to the propagation of sound waves through a material. For solids, sound propagation is the periodic squeezing and stretching of the grain fabric. In liquid or gas it is the periodic compression and rarefaction of molecules (Allouche et al., 2005). Several types of waves exist and they are classified into different categories. The fastest waves are the body waves and the two main body waves are celled P- and S-waves. These waves were recorded in this project and will be part of the focus of this report.

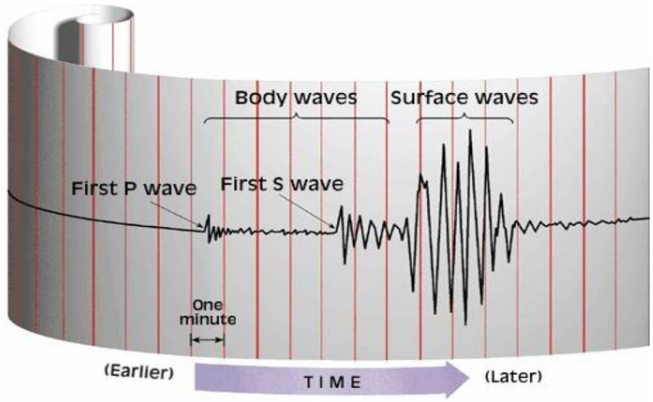

Figure 2.2: Examples of first responses for P- and S-waves compared to surface waves (Modified from Renaissance (2009))

The propagation velocities of the waves are a function of elastic stiffness and density of the material. These parameters depend on the materials mechanical composition including porosity, permeability, etc. Therefore the acoustic velocities of a material can provide valuable information about the material it travels through. It is assumed when using these relationships that the theory of elasticity holds.

Primary wave

The P-wave is the primary wave, also called the pressure wave. It is the wave that travels the fastest in any medium and therefore arrives at a specific point before any other wave. A P-wave velocity can vary between 5-10km/h in the earth's crust (Helffrich and Wood, 2001), and it can travel through both solid and liquid material. In shales the P-wave velocity typically ranges between 2.133 to 5.181 m/s (Allouche et al., 2005).

P-waves are compressional waves, meaning they push and pull the medium they move through in the direction of the wave propagation. This indicates that any particle in the medium moves back and forth in the same direction as the wave energy (Stovas and Hao, 2015).

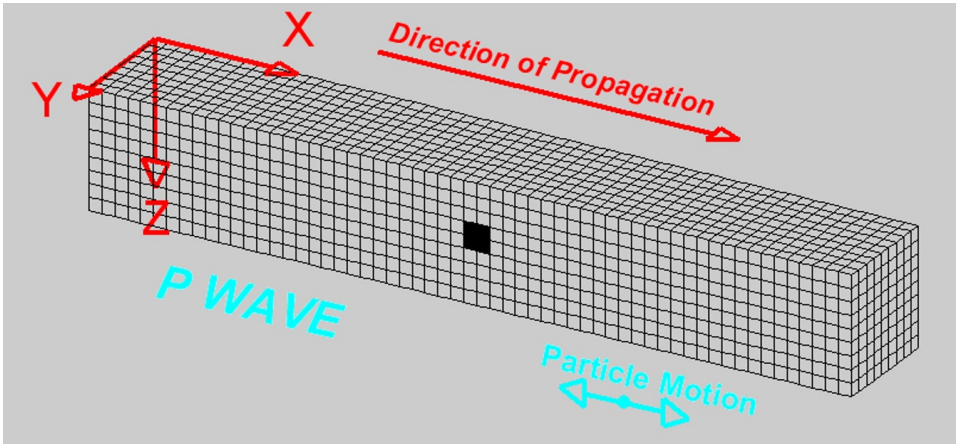

Figure 2.3: Illustration of the P-wave behaviour (Modified from Stovas and Hao (2015))

Secondary wave

Another type of body wave is the secondary wave, also called S- or shear wave. It is the second fastest wave to arrive at a given point, which means it is slower than the P-wave. S-waves travel about 0.6 times the velocity of P-waves and generally have a higher frequency (IRIS and USGS, 2017). It can only move through solid material, so no S-waves will travel between two points if there is no solid connection between them.

The S-wave travels through the particles in the medium it moves through perpendicularly to the wave propagation direction (Stovas and Hao, 2015). S-waves are categorized into SV- and SH-waves depending on if the particle movement is up and down or from side to side, respectively, compared to the propagation direction.

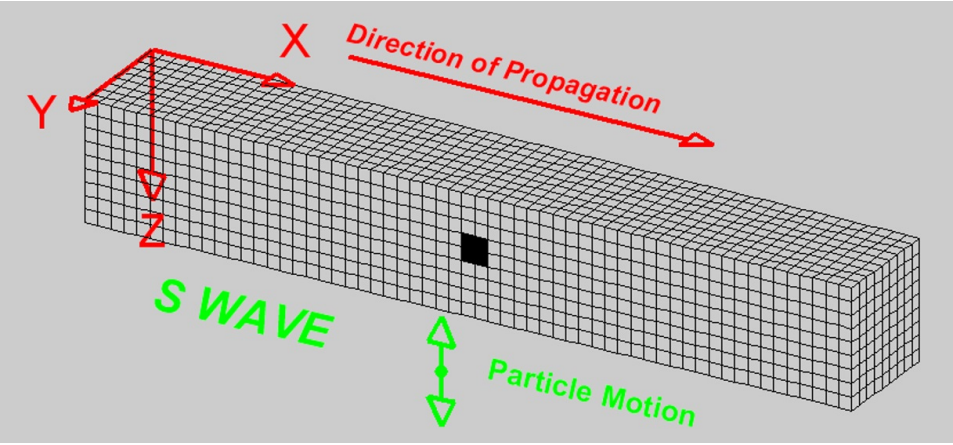

Figure 2.4: Illustration of the SV-wave behaviour (Modified from Stovas and Hao (2015))

2.2 Effects on Velocities

Many parameters are known to affect the wave velocities of a material. Similar material will not have the same homogeneity, isotropic or elastic behaviour. This will affect the measurements in different ways. External parameters like stress, pore fluid and temperature may affect the velocity response in a specific material. It is important to understand which of these parameters influence a material to be able to fully interpret the velocity responses.

The elastic wave response is known to vary with stress. Typically, the velocities will correlate positively with increasing stress but this is not always the case. It may also inversely correlate with velocities. According to Zhao and Roegiers (1995), microcracking resulted from stress can cause a decrease in P-wave velocity. A change in stress state implies that pores may expand or shrink, changing the porosity of a rock. The stress induced therefore changes the crack density, which implies that wave velocities are dependent on stress. For large shear deformations, the velocities are more related to strain than to stress (Fjær, 2006). Microcracking is

one of the processes causing creep and may result in a decrease in the effective Young's modulus.

The elasticity of a porous material may be highly sensitive to the presence of a pore fluid. Poorly consolidated, water saturated rocks tend to have a P-wave velocity several times higher than a dry rock (Fjær et al., 2008). This indicates that the presence of pore fluid provides additional resistance to compression. The effect of saturation in a rock with high confining pressure will be much smaller as the rock stiffness is higher and the pore fluid contribution is reduced (Fjær et al., 2008). The P-wave velocity in a really stiff rock will be reduced due to an increase in saturation. The composition of the pore fluid also affects the measurements. Salt water will increase the P-wave velocity, resulting in a higher velocity through a sample when the salinity is high.

An increase in temperature normally gives a reduction in velocities (Fjær et al., 2008). If the rock components undergo a phase transition within the actual temperature range, such as melting or freezing of pore fluid, the effect is particularly high.

The anisotropy of a material is of great importance. Shale is anisotropic with its many layers. The stiffness of each layer may vary relative to direction, which will affect the acoustic properties of the rock (Fjær et al., 2008). A generalized version of the wave equations and its solutions can take this into account, but it will not be discussed in this report.

A material's heterogeneity also affects the velocity through the material. At each intersection or fracture in the material some wave energy may get lost and the signal gets weaker (Sato et al., 2012). This means that more heterogeneous material will loose more energy than homogeneous material. Some of the S-wave energy may also convert to P-wave energy at intersections and therefore also decrease S-wave energy.

It is important to choose the right frequencies for the purpose of each experiment. Higher frequencies are more accurate than lower frequencies but they get damped more easily. Lower frequencies can also travel further than high frequencies. It can be said that a heterogeneous material will damp high frequencies more than lower frequencies as there are more interfaces. Shales are heterogeneous rocks and therefore it should be safe to say that lower frequencies will give a better response than higher frequencies.

2.3 Empirical Elastic Relationships

Compressional and shear wave velocities are closely related to the elastic properties of the material it travels through and are almost independent of the frequency (Allouche et al., 2005). According to Hooke's law, the elastic properties relate stress to strain in a material. This is why the acoustic velocity measurements can provide valuable information about the material.

Acoustic Impedance

The knowledge of the P-wave velocity through a material gives the possibility to determine the compressional acoustic impedance, Z, of a material (Allouche et al., 2005). For a homogeneous, non-dissipative medium, the acoustic impedance can be given as:

$$Z = \rho V_P \tag{2.1}$$

where ρ is the density of the material (kg/m^3) and V_P is the velocity of the compressional wave (m/s). For this project, it is assumed the material is homogeneous for simplicity. The acoustic impedance describes how much resistance an ultrasound ray encounters as it travels through a material (Weerakkody and Morgan, 2012). The reflection of ultrasound at the boundary between two materials occur because of the difference in impedance of the two materials.

For the material used in this experiment, an approximate impedance would be between 4-10. It would all depend on the porosity of the material as well as the stresses Holt (2016).

Dynamic Moduli

Dynamic moduli of rocks are the moduli calculated from elastic wave velocity and density. It may differ significantly from the static moduli, which are those measured directly from an experiment (Zimmer, 2003)

In general, the body wave velocities have the form (Mavko, 2017a):

$$velocity = \sqrt{\frac{moduli}{density}} \tag{2.2}$$

From this, the P-wave velocity, V_P, and S-wave velocity, V_S, can be expressed as:

$$V_P = \sqrt{\frac{K + \frac{4}{3}\mu}{\rho}} = \sqrt{\frac{\lambda + 2\mu}{\rho}} = \sqrt{\frac{M}{\rho}} \qquad and \qquad V_S = \sqrt{\frac{\mu}{\rho}} \tag{2.3}$$

where
ρ - density
K - bulk modulus = 1/compressibility
μ - shear modulus
λ - Lamé's coefficient
ν - Poisson's ratio
M - P-wave modulus = $K + \frac{4}{3}\mu$

Since most rocks do not show absolutely isotropic, homogeneous or linearly elastic behaviour, these equations are only approximations (Fjær et al., 2008). The big differences within similar formations may complicate the relationship between the elastic moduli and acoustic velocities. The equations 2.3 can however be rearranged to find the moduli (Mavko, 2017a):

$$M = \rho V_P^2 \qquad , \qquad K = \rho(V_P^2 - \frac{4}{3}V_S^2) \qquad and \qquad \mu = \rho V_S^2 \tag{2.4}$$

The expressions of velocities can also be written in terms of Poisson's ratio (ν) and Young's modulus (E)

$$V_P = \sqrt{\frac{E(1-\nu)}{\rho(1-2\nu)(1+\nu)}} \tag{2.5}$$

Equation 2.3 and 2.5 are given in dynamic moduli that may deviate from the static moduli (see Section 2.4). Poisson's ratio establishes a relationship between V_P and V_S as given here (Mavko, 2017a):

$$\frac{V_P^2}{V_S^2} = \frac{2(1-\nu)}{1-2\nu} \qquad and \qquad \nu = \frac{V_P^2 - 2V_S^2}{2(V_P^2 - V_S^2)} \tag{2.6}$$

2.4 Static and Dynamic Moduli

The equations in the previous sections indicate a link between the parameters describing elastic waves and the mechanical properties of the rock. From these acoustic velocities and densities one can obtain the dynamic moduli. However, a range of experimental evidence proves that dynamic moduli may deviate significantly from static moduli, especially at lower stresses (Fjær et al., 2008).

Dynamic moduli are as mentioned obtained from acoustic velocities and densities. The static moduli are obtained from stress and strain measurements in a mechanical rock test that describes its response to strain rates smaller than $10^{-2}s^{-1}$ with large amplitudes. It measures the material response to rapid stress oscillations where the strain typically ranges between $1-10^{-4}s^{-1}$ and the amplitude is small (Fjær, 1999). The biggest difference between static and dynamic measurements is therefore the strain amplitude.

The difference between the two moduli is decreasing as the confinement stress increases (King, 1969), as well as when a sediment is well cemented and strong. The static and dynamic moduli are equal for homogeneous, elastic materials like steel. This is not the case for inhomogeneous formations, indicating that the source of the discrepancy is likely to be linked to the heterogeneous microstructure of the rocks as well as its strength. Pore fluid may also be a reason for the discrepancy between dynamic and static moduli (Fjær et al., 2008).

2.5 Hypothesized Responses

For this experiment some rough calculations of expected responses were made. This was done to get a sense of what velocities could be expected for this setup and so that it would then be easier to interpret and measured data.

P- and S-wave velocities for water, steel and shale (LTD, 2017; Mavko, 2017b) were found to calculate an approximate arrival time for each material. The project supervisor reviewed the velocities (Holt, 2016). The values chosen are believed to be close to the expected values for a typical shale that creeps. The radius of the cylinder was used as the distance the waves would travel in the horizontal direction as well as to calculate the shortest distance the waves would travel in the steel cylinder (circumference = π x diameter). For the vertical calculations the distance

67 mm was used, which is close to the initial length of the samples used in this experiment. The equation:

$$traveltime(\mu s) = \frac{distance(mm)}{velocity(mm/\mu s)} \tag{2.7}$$

was used to calculate the expected travel time for the different materials. The results can be seen in Table 2.1.

	Hor. P-wave Response		Ver. P-wave Response		Ver. S-wave Response	
Material	Velocity (m/s)	Travel Time (μs)	Velocity (m/s)	Travel Time (μs)	Velocity (m/s)	Travel Time (μs)
Water	1480	26.07	1480	45.95	-	-
Steel	5890	10.2	5890	11.38	3250	20.62
Shale	2500	15.12	2500	26.8	800	83.75

Table 2.1: Hypothesized responses to be used for interpretation of the wave responses.

Chapter 3

Laboratory Experiments and Test Procedures

Testing of rock samples in the laboratory is an important part of the research on rock mechanics and mechanical behaviour. As mentioned in Section 1.3 one should ideally transfer the rock material from the ground to the apparatus without disturbance, loading or unloading of stresses. These are difficult, if not impossible, requirements to satisfy in practice and therefore they have to be taken into account.

Several apparatus are available for rock testing depending on the goal of the research. For this research the goal was to see how the shale that has been shown to creep in the field would behave when exposed to different fluids, as well as to see if mechanical properties could be derived from the measurements.

An apparatus with several measurement methods was set up to meet the goals of this report. These will be described in the next sections, as well as the test procedures. Calculation methods for different measurements will be described at the end of this chapter.

3.1 Sample Material

The experiments for this project were carried out on a shale that is considered classified. This shale is currently used in projects at SINTEF Petroleum and it

has been observed to creep in the field, creating a barrier in the annulus. This behaviour makes it a relevant material to test.

The material was extracted from a well using oil based mud during drilling and was packed directly in fiberglass core barrels. To maintain the cores in good condition they were properly packed before transportation. After being tested on the mainland, some material was sent to SINTEF Petroleum in Trondheim for further investigation. There the material has been stored in Marcol Oil in a room temperature controlled box. Marcol Oil is a transparent, colourless purified mixture of liquid saturated hydrocarbons (ExxonMobil, 2003) produced by ExxonMobil, which among other uses is employed to preserve the material and prevent it from drying out.

3.1.1 Sample Preparation

The sample material was taken out from the room temperature controlled box filled with Marcol Oil to be cut into appropriate sized samples for the purpose of this experiment. In total six shale samples were cut out. The samples were collected in the same manner each time in order to prevent additional variables.

The exact length and diameter of each sample was measured prior to testing using a digital sliding caliper. The weight of each sample used was measured using a digital weighting scale. The measurements of the samples that were used for testing can be seen in Table 3.1 below:

	Sample 1	Sample 2	Sample 3
Length (mm)	68.04	67.3	67.3
Diameter (mm)	37.8	37.8	37.8
Weight (g)	179.86	177.63	178.16

Table 3.1: Sample properties

Before each sample was placed in the test cylinder, a cloth was used to dry off as much storage oil as possible. This was not possible to do perfectly as it was difficult to see how much oil was left and one had to be careful not to damage the fragile sample. It should be noted that this might affect the results of the test if too much oil was left on the sample walls. The samples were taken out of the Marcol oil as

close to the start of the tests as possible to ensure they would not dry out before the experiments started. Each sample was carefully placed in the cylinder.

3.1.2 Characterization

A short characterization of the shale tested in this experiment will be displayed here. As mentioned earlier the name and location of where the shale was extracted is confidential. It is still important to understand its properties to better interpret its behaviour during testing.

The material used for this experiment has been characterized for a previous experiment and the results available from these tests will be presented here. The material from both experiments is from the same location and approximately the same depth. The experiment procedure for this report was based on the results found in the previous experiment.

An X-ray diffraction (XRD) analysis was conducted on the material to measure its mineralogy. Seven samples from the same intervals ware used. The results of the composition of the material can be seen in Table 3.2.

Depth	m	2905.9
Quartz	$wt.\%$	25.5
Plagioclase	$wt.\%$	2.3
K-Feldspar	$wt.\%$	1.8
Calcite	$wt.\%$	17.1
Pyrite	$wt.\%$	1.8
Muscovite	$wt.\%$	2.8
I+I/S ML	$wt.\%$	47.7
Chlorite	$wt.\%$	1

Table 3.2: Shale mineralogy of the material in percent

Other petrophysical parameters like porosity, pore water salinity and bulk density were also determined. To determine the activity of the clay mineral surfaces within the samples, a conductometric titration (wet chemistry) method was used to analyze the Cation Exchange Capacity (CEC) measurements of nine samples. Some

uncertainty was found in the actual pore water salinity, fluctuating between 2.1 and 3.5 %. This report chose to use the later pore fluid salinity.

Property	**Unit**	**Value**
Depth	m	2901-2902
Porosity	%	24
Pore water salinity	$wt.\%NaCl$	3.5
Bulk Density	g/cm^3	2.36
CEC	$meq/100g$	27.4

Table 3.3: Petrophysical parameters

An undrained triaxial test was performed to establish some of the shales mechanical properties. All stresses, axial and radial displacements were recorded continuously during the test. The peak axial stress measured on the onset of failure was taken as the compressive strength of the sample at a specific confining pressure. From this peak stress condition, the 2D mean effective stress, p‘, and 2D deviatoric stress, q, were calculated using the relationships:

$$p' = \frac{AxialEffectiveStress + RadialEffectiveStress}{2} \tag{3.1}$$

$$q = \frac{AxialStress - RadialStress}{2} \tag{3.2}$$

By taking the peak stress conditions for multiple samples in the same layer, the friction angle and apparent cohesion was computed. The stress-strain data during active loading from $\frac{1}{3}$ to $\frac{2}{3}$ of the peak deviatoric stress were used to compute Young‘s Modulus, E, and Poisson‘s Ratio, ν. The results have been gathered in Table 3.4:

Inclination	deg	0
Effective cons. pressure	MPa	5.10
Linear cohesion	MPa	2.1
C_0	MPa	7.3
Friction angle	deg	31.1
Poisson's Ratio (unreliable)	-	0.45
Young's Modulus (E)	$GPa4$	

Table 3.4: Shale Properties

The shale formation was described as overall fragile and occasionally splits parallel to the bedding plane. When exposed to tap water, small core pieces immediately disintegrate from the rock. This reaction suggests a clay content that is given to swelling properties.

3.1.3 Material Description

The material used for this experiment consisted of a well laminated sequence of dark black intervals with some alternating lighter grey intervals. The lamination was oriented approximately 90 degrees (horizontal) relative to the length of the sample. It consisted mainly of silty clay. Some samples had visible fractures to the naked eye. This could be natural or may be a result of outer stimulation.

It is difficult to know what may have created the fractures seen on the samples. The material may have been damaged when taken out of a well, during storage or during transportation. The fractures may give the material a weaker strength than what it initially had. This reduction in strength was taken into account when interpreting the results. A CT scan of each sample was done prior and after each experiment to detect possible microfractures and to see how homogeneous the samples were.

Although similar material was used for each test, some specific features that may have affected each test were present. The features seen by the naked eye that were believed to have the most impact on the experiments are listed below and pictures of each sample can be seen in Figure 3.1 and Figure 3.2.

- **Sample 1:** a small fracture approximately 1 cm from one end was seen

parallel to the bedding; micro fractures were observed on both short ends with a different angle than the bedding plane (Figure 3.1 (a) and (b)).

- **Sample 2:** small fractures could be seen on both short ends of the sample with a different angle than the bedding plane (Figure 3.1 (c) and (d)).
- **Sample 3:** small fractures could be seen on both ends of the sample with a different angle than the bedding plane (Figure 3.2 (c) and (d)).

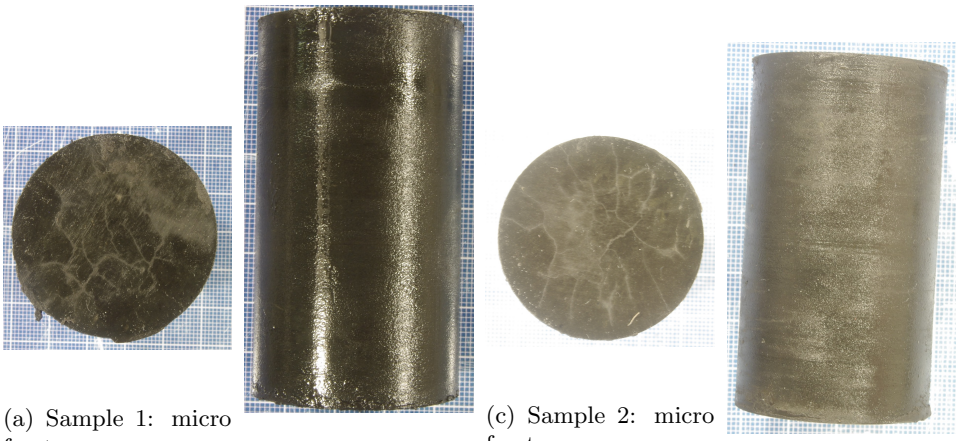

(a) Sample 1: micro fractures

(b) Sample 1: a fracture can be observed close to the upper end of the sample

(c) Sample 2: micro fractures

(d) Sample 2: well laminated

Figure 3.1: Pictures of sample 1 and 2 before testing. Micro fractures on the short ends and the parallel bedding can be observed on both samples.

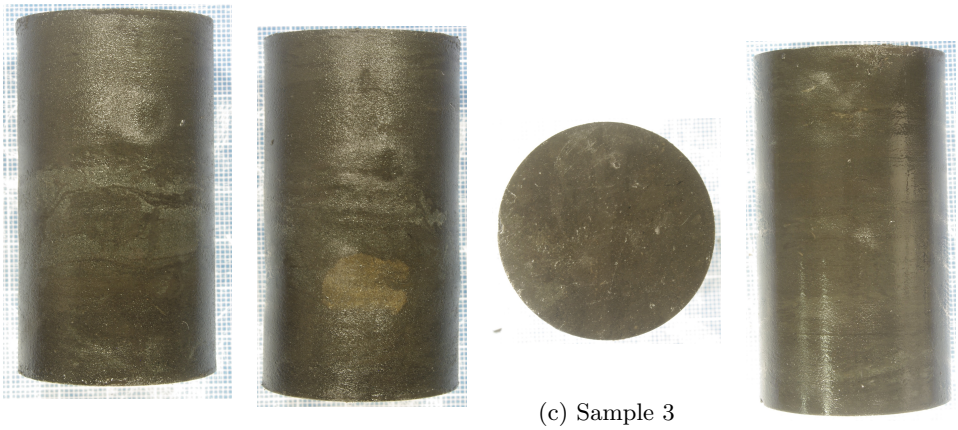

(a) Sample 3a: different layer in the middle of the sample

(b) Sample 3a: distinct clast

(c) Sample 3

(d) Sample 3

Figure 3.2: Figure (a) and (b) show the heterogeneities of the sample initially thought to be used for the third test. It was therefore changed to another sample (c) and (d).

When inspecting the sample that was initially thought to be used for test 3, several heterogeneities were observed (Figure 3.2 (a) and (b)). An approximately 1 cm thick heterogeneity could be seen, which also contained a large distinct clast differing from the rest of the sample. A new sample was therefore inspected and used (Figure 3.2 (c) and (d)) to make sure each sample was as similar as possible.

Despite the fact that the nature of the features was similar in all three samples, the heterogeneity of rocks in general dictates that it may manifest itself differently from sample to sample during testing.

Micro CT Scan

A Micro CT scan was done for each sample after it was tested. Ideally each sample should have been scanned prior as well as after each test, however, due to problems with the CT scan machine, it was not possible to do so. Only sample 3 was scanned before and after test. Sample 3 therefore was the only sample that could be compared prior and after testing.

The purpose of scanning the samples prior and after testing was to see how hetero-

geneous each sample was. This was important for when comparing each test. It was also done to see if there would be any changes in the structure of the material due to stress. Fractures may have been created or closed during the test. It would be interesting to see how and to what extent fractures were created or closed. Every material behaves differently under stress and scanning the samples may provide a better understanding as to how this specific shale reacts under pressure. For the samples that were only scanned after test it was of interest to see how the fractures propagated and how dense they would be.

The CT scan used was located in the Physics building at the Norwegian University of Science and Technology (NTNU) and was performed by Ole Tore Buset. To interpret the images from the CT scan, the software Avizo, developed by FEI Visualization Sciences Group, was used.

3.1.4 Fluid Preparation

Different fluids were introduced into the pore space of each sample. This was done to see how the samples would react when exposed to various minerals within the fluid when stress was applied. The fluids used for the three tests will be described below.

Test 1

A 3.5% sodium chlorite (NaCl) solution was used as fluid for the first test. Adding NaCl solids to distilled water was done to prepare the fluid.

This is believed to be a similar fluid to the natural pore fluid in the formation. Testing the shale properties under as natural conditions as possible gives the best possible indication of how willing the shale is to creep without external influences. As there are some uncertainties as to what the exact pore fluid concentration is, this test may not represent the exact downhole conditions.

Test 2

A 20% potassium chlorite (KCl) solution was used as fluid for the second test. Adding KCl solids to distilled water was done to mix the fluid for the second test.

Laboratory and field studies have demonstrated that potassium cations at sufficient concentrations in water-based drilling fluids can effectively reduce the swelling and dispersive tendencies of clay-containing shales (O'Brien and Chenevert, 1973). Potassium chlorite is therefore often added to drilling fluids when drilling through water-sensitive shales. The K^+ ions reacts and attaches to clay surfaces and lend stability to the shale exposed to the drilling fluids (O'Brien and Chenevert, 1973). KCl is also added to cement slurries when applied in water-sensitive shales and clays as it helps improve the cement bond by preventing swelling (Halliburton, 2017).

It is believed that the shrinking reaction can be reversed if a high enough concentration of KCl brine is used. Holt (2017) has performed consolidated undrained triaxial tests where a 20% KCl solution resulted in a large volumetric expansion. Not many experiments have been done to examine this phenomena and this was a good opportunity to examine this further.

Test 3

For the third test, fresh water was used as fluid. Ideally, deionized water should have been used but the distillation machine was out of order and could therefore not provide it. Room temperate water from the sink was therefore used.

Fresh water has been proved to cause swelling in shales (Sønstebø and Holt, 2001). As water is exposed to shale the difference in chemical potential drives the water into the shale and develop swelling pressures. The water will always flow from the material with the higher chemical potential to the material with the lower chemical potential (Chenevert, 2017). This movement will continue until the total potential is equal. The swelling potential depends on the initial water content in the shale, decreasing with the increasing initial water content (Lyu et al., 2015).

It was of interest to see how this material would react to fresh water and to see if any swelling could result in creep.

3.2 Equipment

A triaxial experiment was conducted on the shale samples using a mechanical loading frame (Figure 3.3) and an oedometer cylinder. The axial force applied to

the sample was increased over time by adding weight to the system. The maximum axial load that could be applied was approximately 30 kN due to weight unit limitations. A sample was placed in a steel cylinder with steel pistons in both ends. Uniaxial deformation sensors were glued to the cylinder wall to measure the horizontal deformation of the sample. Pockets of Peek plastic holders were created in the oedometer cylinder to place ultrasound sensors as close as possible to the sample itself to measure ultrasound horizontally. Ultrasound sensors were also incorporated in the steel pistons to measure ultrasound vertically.

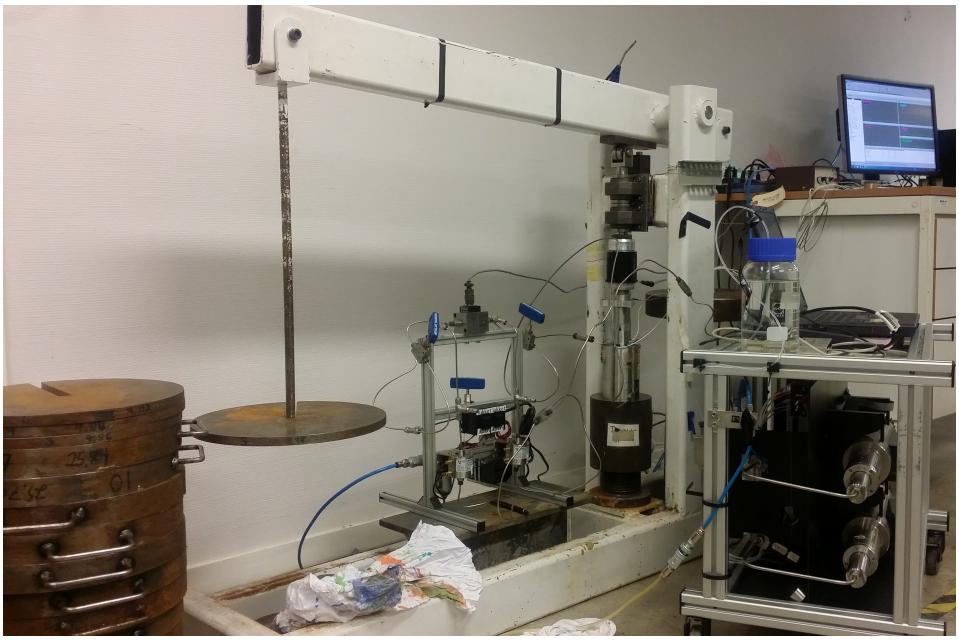

Figure 3.3: Overview of setup used for the experiments.

Placed on top of the upper piston, a linear variable differential transformer (LVDT) measured the axial displacement of the sample. A load cell recorded the axial load applied to the sample and a temperature sensor was set up close to the oedometer cylinder to register the temperature in the laboratory at all times. A transient setup was connected to the oedometer to be able to test the differential pressure of the sample during each test. A pump system was connected to the setup to maintain, change and control pore pressure in the sample. An 8-channel QuantumX MX840B universal amplifier connected the different measurements to the computer. The readings were recorded and analyzed using the computer software CatMan. When the data was extracted from the software, Excel was used for interpretation. To

interpret the ultrasound data, a program called Speedy was used through MatLab.

The main components that were used for the following experiment are described in detail in the next sections. Some of the same equipment was used in the associated Project in the fall 2016 (Brun-Lie, 2016) and will be used again here.

3.2.1 CatMan

During the experiments, a computer software called CatMan AP V4.2.2 was used to record and store the measurements of the samples. The software also enabled visualization and analysis during testing, which was beneficial when parameters were changed underway.

A QuantumX MX840B universal DAQ amplifier (Figure 3.4) was used to connect the test measurements to the computer software. The module enables the measurement of eight different parameters at the same time, using one single device.

The sampling rate was generally set to every 10 seconds. It may have been beneficial to increase the sampling rate but the amount of data this would give would be difficult to work with. For some parts of the experiment, for example when performing a permeability test, the sampling rate was set to every second to record as much information as possible.

Figure 3.4: The 8 channel universal amplifier (Modified from MX840B (2017)).

3.2.2 Dead weight load frame

As seen on the Figure 3.3, the load frame consists of a weight arm where weight units are added to apply axial force to the sample. The weight arm will also make sure the pistons (see section 3.2.3) are kept in place if the pressure in the sample increases. The length of the arm is 1 meter relative to the placement of the sample,

meaning the weight put on the frame will increase by a factor of 10 relative to the sample position.

The load frame is an essential element in the test equipment. The two most important features when testing mechanical properties of rock are the frame stiffness and the ability to operate the system in a constant displacement mode. A build-up was placed under the weight loads to ensure the setup would not be damaged if the sample or oedometer should collapse.

Calibration

Before the experiments started, each weight unit was carefully weighed for accuracy. The load frame was checked prior to testing to make sure everything was placed the right way and to eliminate potential hazards during each test. It was important to make sure the rotating wheel between the weight arm and the oedometer position was correctly faced. If possible it is beneficial if the loading frame is as horizontal as possible. In the case that this is not possible, consistency of angle for all tests is preferable. This will reduce the factors of inequality between each test.

3.2.3 Oedometer Cylinder and Pistons

A hollow oedometer cylinder made of steel was used to house each sample during testing. Two sintered pistons were placed at each end of the cell, having the sample in between them. They are mainly made of steel except for the end in contact with the sample, where a piece of Peek plastic is glued on to get a better ultrasound connection between the sample and the pistons. Both pistons have a crystal inside which disperses the ultrasound pulses across the whole sample area. Both the cell and the pistons have acoustic properties so that acoustic measurements can be performed (see section 3.2.10).

In addition, two plates of stainless steel were placed in between the sample and the pistons to make sure the fluid flow was equally distributed across the whole sample surface. A lubricated O-ring around the piston's circumference prevents leakage. It is important to make sure these lubricated rings are not damaged and to put grease on them prior to setting up the test.

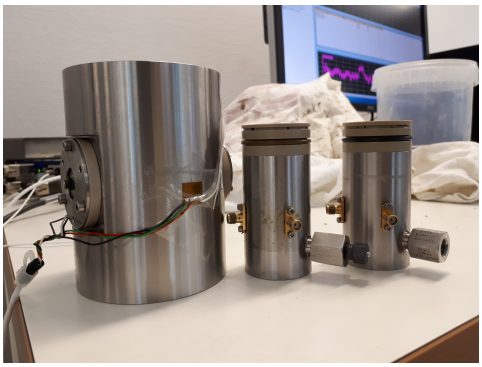

(a) Steel cylinder and pistons

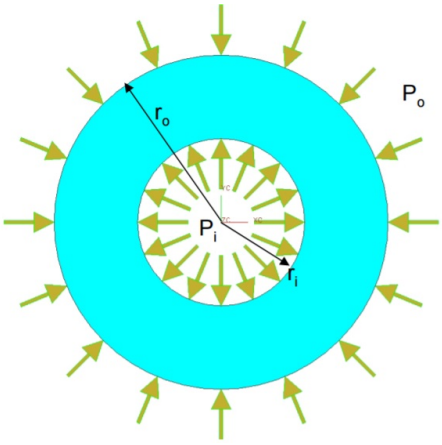

(b) Sketch of cylinder

Figure 3.5: (a) the steel cylinder with corresponding pistons and (b) a sketch of a cylinder under internal and external pressure loading (Modified from of Washington (2017)).

Some limitations to the setup in use are present when simulating creep. In the field, the goal is to make the shale creep towards the casing wall in a cylindrical well. That means the formation creeps inwards to seal off an annulus. In this experiment however the shape of the oedometer cylinder does not fully represent a drilled hole with casing. The cylinder is hollow, meaning that the sample will not have to fill in the gap in the middle but the gap between itself and the inner boundaries of the oedometer cylinder. This means the sample will creep outwards. This must be taken into account when interpreting the data.

Length (mm)	Inner Diameter (mm)
75	38.0

Table 3.5: Oedometer cylinder dimensions.

3.2.4 Pump System

During loading tests of rocks it is very important to be able to control the pore pressure, the drainage of pore water or both. By controlling both pore pressures and total stresses it is possible to control the state of effective stress in the sample

(Atkinson and Bransby, 1978). For this experiment, the pore pressure had to be kept constant. For the pore pressure to remain constant it is important that the brine can flow from and into the sample as the material volume responds to changes of effective stress. As pore pressure remains constant, the changes in total stress and effective stress are identical (Atkinson and Bransby, 1978).

Due to limited access to equipment, different setups were used to control the pore pressure for each test. For the first test, an LC-8A SHIMADZU Preparative Liquid Chromatograph (Figure 3.6) was used to control the pressure in the sample at all times. 10 kgf/cm_2 was set to be the constant pressure (approximately equal to 10 bar or 1 MPa).

For the second test, a volume accumulator was used to control the pressure. The pressure was set with a Quizix Pump to 25 bar, using the software PumpWorks.

For the third test a Quizix Pump was used throughout the whole test and pressure was set to 20 bar. For all three tests an accumulator was used to make sure the pressure was constant at all times. A pressure sensor connected to the accumulator recorded the pressure during each test through CatMan.

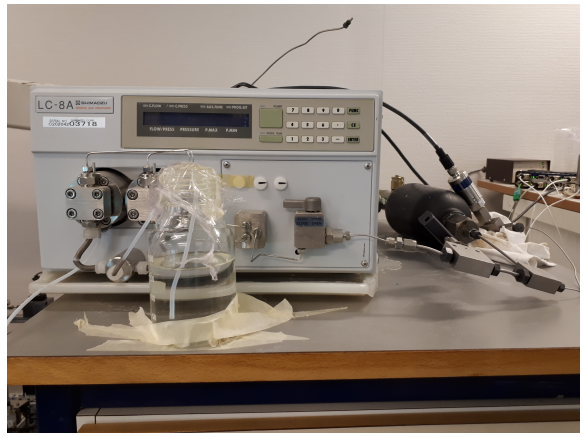

Figure 3.6: The Pump system used in test 1. The accumulator can be observed on the right hand side of the chromatograph.

Calibration

A two point calibration was done on the pressure sensor prior to testing. A Quizix Pump was used to set both pressures which then were registered in CatMan and

calibrated. Different pressures were then set and monitored on CatMan to see if it corresponded with PumpWorks. No leakage or air bubbles were observed that could possibly have an affect on the future measurements.

3.2.5 Uniaxial Deformation Sensors

Strain gauges of the model CEA-06-125UT-120 were used to measure the uniaxial deformation in the sample. A single strain gauge consists of two-element 90 degrees tee rosette and four soldering tab areas (Austbø, 2016). When the internal pressure in the steel cylinder deviates from its initial pressure, the grid areas of the strain gauges alter. This results in an electrical resistance that can be transformed to a signal that is measured. The strain gauges have a gauge factor of 2.090 $\pm 0.5\%$ at $24°C$.

For this experiment two sensors were attached to the outside wall of the oedometer cylinder (Figure 3.5) opposite to each other. They were connected in pair using soldering copper wires. This way the radial stress in one horizontal direction could be measured. Copper wires connected them to the amplifier, which again was connected to the computer. Measurements were recorded and stored in CatMan.

Some issues with the strain gauges presented themselves during the first and second test. They seemed to be very dependent on the temperature in the laboratory and showed unexpected behaviour. New gauges were therefore glued on before each test to try to correct the defects. Different glue was used and for the third test the glue was cured at 80 degrees for one hour to see if the energy transfer between the steel in the oedometer cylinder and the gauges would improve.

Calibration

For the first test, a calibration from the experiment for the Project related to this Master Thesis was used (Brun-Lie, 2016).

For the second test a new tabular calibration was done. Fresh water was used as sample and a Quizix Pump set appropriate pressures. The safety pressure was set to 10 MPa. Before the test started, the system was checked to be sure there was no leakage and that the system was stable. A tabular calibration was then performed manually through CatMan. The readings were taken as accurately as

possible, however, the measurements were taken visually and were therefore subject to human error. The calibration factors were noted and the system was updated. A hysteresis was created from the measurements and can be found in Appendix B.

The third set of strain gauges was calibrated the same way as the second set.

Sand Sample Check

Due to unexpected measurements during the second test, a triaxial test using sand as a sample was performed to see if the strain gauges were calibrated and gave meaningful responses. Only axial load was applied to see how the strain gauges would react to stress.

Sand was used because it shows a hardening behaviour and decrease in volume when exposed to triaxial loading conditions. The radial stress would therefore change as the load applied to the system changes.

The responses showed no deviation in expected response. When a stepwise loading path was applied to the sample the radial stress increased stepwise. When the load was stepwise decreased it showed a stepwise decrease in radial stress, with no deviation from the response measured when loading up.

A new set of strain gauges was glued on the oedometer cylinder for the third test. This time the glue was cured at 80 degrees for one hour to enhance the connection between the oedometer cylinder and strain gauges.

Temperature Correction

Since the sensors seemed to be dependent on the temperature in the laboratory a correction was made for the third test. The oedometer cylinder with a sand sample inside was put in a heat chamber at 29 degrees and at 39 degrees for a period of time. The radial stress and temperature was registered throughout the test. Then an average was taken of both measurements for both temperatures. The slope m and crossing line b was calculated using:

$$m = \frac{y_1 - y_2}{x_1 - x_2} \qquad and \qquad y_n = mx_n + b \tag{3.3}$$

This was then used to correct the radial stress measurements.

3.2.6 Linear Variable Differential Transformer

Linear Variable Differential Transformer (LVDT) is an electrical transformer used to measure uniaxial linear displacement. The LVDT converts a linear displacement from a mechanical reference (null position) into a proportional electrical signal (Fjær et al., 2008), in this case containing amplitude information of the distance of displacement. The LVDT operations do not require an electrical contact between the moving probe and the coil assembly due to its electromagnetic coupling. The LVDT transducers are frictionless, have low hysteresis and have excellent repeatability. This makes the LVDT ideal for this type of testing.

For this project, a MHR500 Shaevits LVDT was used, with a range of $\pm$ 12.7 millimeters (mm). It was placed on top of the upper piston (Figure 3.7) to measure the displacement of the piston relative to the cell as the sample was deformed. The LVDT was connected to the amplifier, which again was connected to the computer. Measurements were then recorded and stored in CatMan.

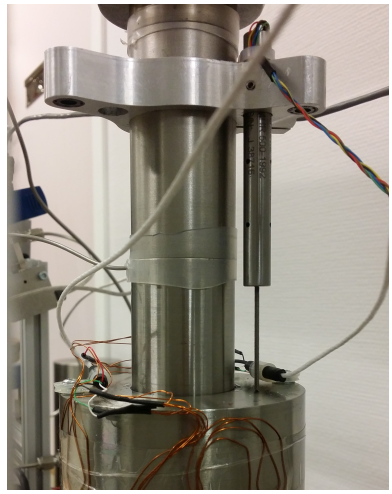

Figure 3.7: A picture of the LVDT in use

Calibration

A tabular calibration of the LVDT was performed using CatMan prior to the experiment for the Project related to this Master Thesis (Brun-Lie, 2016). The same calibration was used for this experiment.

A micrometer was used to hold the LVDT rod in place to take as accurate measurements as possible. Measurements were done approximately every second millimeter and the values were read off of CatMan. The results were then plotted and can be seen in Appendix B. The calibration factor was noted and the system was updated.

3.2.7 Load Cell

A RLMZ 100KN 10 load cell (Figure 3.8) was used to digitally measure the load applied to the sample. Mathematically, the axial force applied to the sample can be expressed as:

$$\sigma = \frac{F * F_{mech}}{A} = \frac{4mgF_{mech}}{\pi d^2} \tag{3.4}$$

where σ is the stress acting on the sample, F is the force applied, A is the cross-sectional area of the sample, m is the mass of the sample, and g is the gravity constant. $F_{mech} = 10$ is the weight factor for this experiment due to the placement of the sample relative to the mechanical loading frame setup.

Figure 3.8: Load cell

The load cell was connected to the amplifier, which again was connected to the computer. Measurements were then recorded and stored in CatMan.

For this experiment, the load cell was placed on top of the upper piston of the cylinder. It is important to make sure it is centered on top of the sample. This is

to prevent the load from being unequally distributed between the weight arm and the sample in the cylinder.

Calibration

A tabular calibration was done prior to testing. The cell was placed in the dead weight frame setup and loads were put on the cell step wise. The measurements were registered through CatMan, the calibration factors were noted and the system was updated. These can be seen in Appendix B.

3.2.8 Differential Pressure Sensor

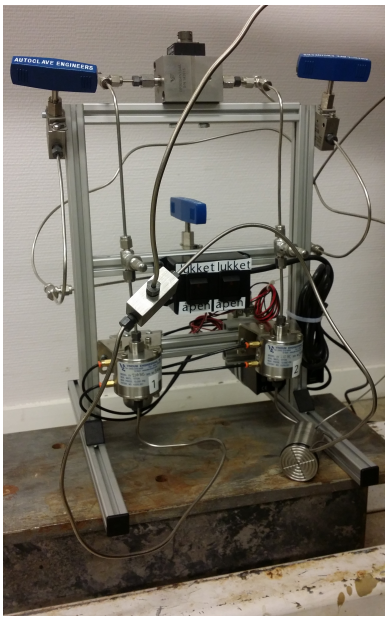

(a)

(b)

Figure 3.9: (a) Transient permeability setup and (b) Validyne Demodulator

A transient permeability setup made by Jørn Stenebråten at SINTEF Petroleum was used to test the permeability of the sample during each test. The setup was connected between the pump setup and the lower and upper pistons of the oedometer cylinder. Thin steel tubes connected them all together. A Validyne, model CD15

Carrier Demodulator (Figure 3.9 (b)), was coupled between the sensor and the amplifier to measure the differential pressure when testing the sample.

An open and close mechanism makes it possible to perform differential pressure tests that later can be used to calculate the permeability of the sample. When closing the switches connecting the sample to the pump, the sample gets isolated. When rotating the needle valves inwards or outwards one circumference, the pressure at both ends of the sample changes. This difference in pressure is measured by the sensor and the time it takes for the sample to stabilize again can be used to calculate the permeability of the sample. The longer it takes to reach pressure equilibrium the less permeable the material is. Both positive and negative differential pressure pulses were taken.

Calibration

Calibration of the setup was done prior to the experiment. To ensure the system was reliable, values were checked using air pressure. The monitoring showed that the system was symmetric and well calibrated. The setup was then checked for air bubbles by circulating 1% NaCl throughout the whole system.

Circulation with fresh water or paraffin was done after each test, as salts can be very corrosive. Prior to each test, circulation with the appropriate fluid was done to ensure that leftover fluids from previous tests were out of the system before the next test. This way the sample would be exposed to the correct fluid from the beginning of each test.

Differential Pressure Test Procedure

Below a short description of the test procedure for the differential pressure tests performed using the transient permeability setup can be found. The amount of time the pressure needed to stabilize changed throughout the test depending on the permeability of the sample at the time of the test.

- close both switches, rotate both the needle valves inwards one revolution and wait until pressure re-stabilizes
- open the switches and let the pressure stabilize for a few minutes

- close both switches, rotate both needle valves outwards one revolution and wait until the pressure re-stabilizes
- open the switches

3.2.9 Temperature

Temperature is thought to have a great impact on creep behaviour. Therefore the temperature of the room was registered during the whole test. A sensor was placed as close as possible to the oedometer cylinder. Temperature registration was also done to see if changes in other measurements could be affected by temperature changes in the laboratory.

The temperature sensor was connected to the amplifier that was in turn connected to the computer. Measurements were recorded and stored in CatMan. The temperature of the sample itself was not monitored as the equipment required was not available.

3.2.10 Ultrasound

Several ultrasound sources and receivers were used to measure the acoustic properties of each sample. They were connected to an ultrasound machine (Figure 3.10) that transmitted and recorded the different pulses through the software Aptrans. Speedy, created by Idar Larsen and used through MatLab, is a program that allows interpretion of the amplitudes and travel times, among other parameters, to better understand the behaviour of the waveforms. Excel was used for interpretation of the data output from Speedy.

Two transducers were placed within the walls of the oedometer cylinder (Figure 3.5a), opposite to each other and as close as possible to the sample itself. A thin holder of Peek plastic that the transducers were held in separated the sample from the transducers. The horizontal P-wave was measured and the response was sent through wires that were connected to the ultrasound machine.

Four transducers were connected to the pistons of the oedometer cylinder (Figure 3.5a), two on the upper and two on the lower. Within the pistons a crystal is located to better disperse the signal sent through the sample. The transducers acted in pairs connecting one from the upper and one from the lower pistons. One

pair transmitted and recorded P-waves while the other transmitted and recorded S-waves. P-waves were therefore measured in both horizontal and vertical direction, while S-waves were only measured in the vertical direction due to limited setup.

The central frequency of the setup was 500 kHz. In general, the closer the frequencies sent out are to the central frequency of the setup the better the response will be. As pulses with different frequencies behave differently and it was not known what frequencies would give the best results for this experiment, several frequencies were transmitted for both horizontal and vertical directions.

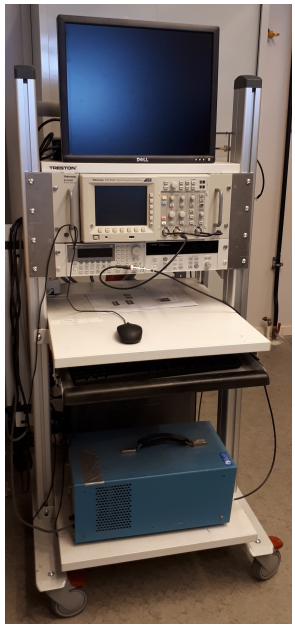

Figure 3.10: The ultrasound setup in use

Table 3.6 shows the different frequencies used during this experiment. As mentioned in Section 2.2, higher frequencies tend to be dampened more easily while lower frequencies may be less accurate. It was also expected to be difficult to find a vertical S-wave due to damping and potential conversion to P-wave.

	Frequencies (kHz)			
	Test 1	Test 2 and 3		
Horizontal P-wave	1000	500	1000	-
Vertical P-wave	500	500	-	-
Vertical S-wave	250	250	125	75

Table 3.6: Frequencies of the transmitted and received pulses in vertical and horizontal direction for the different tests.

Throughout all the three tests a sampling rate between 900 and 3000 seconds was used. More accurate results would have been possible if the sampling rate was higher but the amount of potential data would be difficult to handle. Changes within the sample were assumed to happen slowly and so important data was not believed to have been lost.

Correction

To make sure the measurements were as correct as possible, reference measurements were done to find the delay in the system. For the vertical measurements a sample of Peek was used, while for the horizontal measurements a fresh water sample was used. By knowing the length, diameter and velocities of the reference samples, a correction could be found by taking the average of the measurements and subtracting it from the theoretical measurements calculated by using water and Peek's properties.

Initially the first minimum would be the best pick as first arrival time, but it is not always easy to find. Several picks were therefore taken for each reference in case the output from the actual experiments would be difficult to interpret. A correction for the first maximum arrival time was also made. The zero crossing between the first minimum and first maximum was picked as well for the 75 kHz vertical S-wave. The result from the corrections can be found in Appendix B.

Due to not being able to find an S-wave signal in the first test, the pistons in the oedometer were changed to see if they could give a better response. Different corrections were made for the each test depending on what was required to find an answer.

As sintered disks were placed between the sample and the pistons on each sides of

the sample, a correction in the vertical travel time was made. The P- and S-wave arrival time through the sintered disks were taken prior to the experiment and later subtracted from the arrival time for each test. By recording these times the velocity properties could be calculated for the sample only. The travel time for the different frequencies and picks for the sintered disks can be found in Appendix B.

3.2.11 Bench Top Ultrasonic Setup

Ultrasonic measurements were taken of a sample in its initial state prior to testing. This was done to see how velocity within the sample would change with horizontal direction, which can be used to see how anisotropic the material was.

The setup (Figure 3.11) consists of a transducer/receiver pair that measures the horizontal ultrasound transmitted. A small rotating platform to place the sample on is placed in between the transducer/receiver. For the purpose of this experiment, P-wave measurements were done every 10th degree around the 360 degree sample. The responses were then used to calculate the velocity which was plotted against angle. It was very important to keep the sample hydrated with Marcol Oil at all times as it prevented the sample from drying out and increased the transmission coefficient between the transducers and sample.

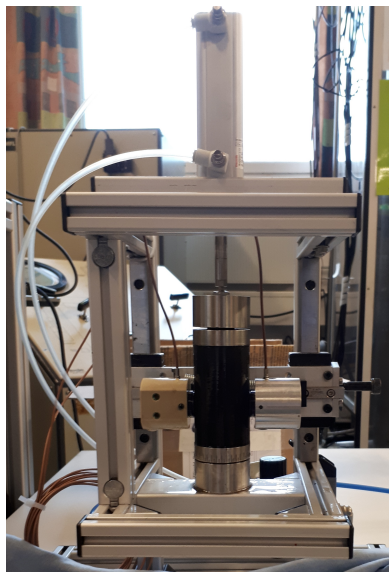

Figure 3.11: The bench top ultrasonic setup.

Correction

A peek sample was used as reference to find the delay in the system. A similar test procedure as used for the material was performed, measuring a P-wave of frequencies 1 MHz and 500 kHz every 10th degree.

The delay in the setup was found by calculating the theoretical travel time using the diameter of the sample and the P-wave velocity in Peek. The measured average value for the Peek was then subtracted from the calculated theoretical value, which gave a correction. The result can be seen in Appendix B. This correction was then added to the measured travel time in the shale.

3.3 Creep Test Procedure

Three creep tests were run with a stepwise loading path to study how each sample would creep under constant load and exposure to different fluids. Weights were added on the load frame when the previous steps uniaxial deformation approximately had stabilized. The general procedure for the creep test is listed below:

- Prepare the sample
- Measure the actual diameter, length and weight of the sample
- Perform Micro CT Scan of the sample (only done for test 3)
- Install the sample in the cylinder and set up all the equipment. Make sure the load cell is centered and that the LVDT is within registration area
- Make sure all the sensors are properly connected to the software and zeroed out
- Start recording the measurements with the computer software and ultrasound
- Add weight on the load frame and set the pump pressure
- Make sure the brine has flowed through the whole sample, then complete the setup circuit by closing the differential pressure setup
- When the uniaxial displacement has stabilized, start to increase the load

- Increase the load step wise until the end of the test, keep the pump pressure constant
- Perform permeability tests for each load increment when axial deformation has stabilized (if possible)
- Perform Micro CT Scan of the sample
- Interpret and analyze the data

It should be observed that a laboratory journal was kept throughout the duration of the experiment.

3.4 Calculations

Strain Calculations

To calculate the axial strain for each load increment, the following equation was used (Atkinson and Bransby, 1978):

$$\epsilon_z = \lim_{\delta Z \to 0} \frac{\delta L}{\delta Z} \tag{3.5}$$

where δL is the axial displacement measured by the LVDT and δZ is the samples initial length. Strain was then plotted against time.

The radial strain is only possible to calculate in the moment the sample is in contact with the cylinder wall as the sample then has sealed the gap and the exact diameter of the sample is known.

$$\epsilon_r = \frac{g(mm)}{d(mm)} \tag{3.6}$$

where g is the initial gap between the sample and the cylinder wall and d is the initial diameter of sample.

Stress Calculations

To calculate the axial stress applied on the sample for each load increment the following equation was used:

$$\sigma_z = \frac{AxialForce(kN)}{Area(mm^2)} \tag{3.7}$$

where the axial force is the force applied on the sample axially and the area is the cross area of the sample.

As it was not possible to know exactly when the sample touched the oedometer cylinder wall, the diameter of the oedometer cylinder was used to calculate the area.

Permeability Calculations

The average of the positive and negative stabilization-time for each differential pressure test was calculated and plotted against time. An exponential trend line was plotted to find the slope α. The permeability k was then found by using the equation:

$$k = \frac{\eta \cdot t \cdot \alpha}{2 \cdot A \cdot K_m} \tag{3.8}$$

where η is the dynamic viscosity (Pa $\cdot$ s), t is the thickness (m), α is the slope (1/s), a is the area of the sample (m^2) and K_m is the stiffness of the setup (Pa/m^2). Assuming the sample touched the wall from the start of each test, the area of the sample was set to 0.001134 m^2 using a diameter of 38.0 mm. The dynamic viscosity used for the different tests can be seen i Table 3.7. The values were found in Haynes (2016).

Test	Dynamic Viscosity (mPa ·s)
1: 3.5 %NaCl	1.060
2: 20% KCl	1.012
3: fresh water	1.002

Table 3.7

Deformation Rate Calculations

Linear trend lines of the strain measurements were used to find the deformation rate for each load increment. Only the last part of the data where the axial deformation had stabilized was used to get an as accurate trend as possible. The accuracy of the calculations was dependent on the time the sample had had to stabilize for each step.

Density Calculations

The density of the sample was found by weighing the sample before the test in combination with calculating its volume by measuring its diameter and length. As the volume of each sample changed during each test it was important to use available measurements to get an accurate calculation of its density at all times. Density is given by:

$$\rho = \frac{m}{V} \tag{3.9}$$

where ρ is the density, m is the weight and V is the volume of the sample.

The samples probably contained a certain amount of pore fluid but unfortunately it was not possible to measure the amount with the equipment available. The pore fluid could therefore not be accounted for in a meaningful way through measurements and was not taken into account when interpreting the results.

Velocities Calculations

The horizontal and vertical P- and S-wave velocities of the sample were found by finding the first arrival travel time and knowing the distance the wave travelled. For the horizontal P-wave measurements the radius of the sample of 38.0 mm was used, while the length of the sample was used for the vertical P- and S-wave measurements. The following equation was used to calculate the velocities:

$$v = \frac{d}{t} \tag{3.10}$$

where t is the first arrival travel time, d is the distance the wave travelled and v is the resulting velocity.

Due to the axial force that was applied to the sample during each test, the length

and diameter changed throughout the tests. For the vertical measurements this was taken into account by using the LVDT measurements to calculate the sample length at all times. For the horizontal measurements it was difficult to know exactly when the sample touched the wall. It was therefore assumed that the radius of the sample was constant.

Geomechanical Property Calculations

Some geomechanical properties were calculated using the results from the velocity calculations. For the calculations of the dynamic moduli the equations can be seen in Section 2.3. The static moduli may be found using the stress and strain results calculated through the measurements through CatMan. Poisson's Ratio may be found using the equation:

$$\Delta\sigma_r = \frac{\nu}{1-\nu}\Delta\sigma_z \tag{3.11}$$

where ν is the Poisson's Ratio and $\Delta\sigma_r$ and $\Delta\sigma_z$ are the change in stress in radial and axial direction, respectively.

The equation:

$$\nu = \frac{\epsilon_r}{\epsilon_z} \tag{3.12}$$

where ϵ_r and ϵ_z are the radial and axial strain, respectively, may also be used to find Poisson's Ratio, ν. Using Equation 3.12 it will only be possible to find the Poisson's Ratio exactly when the sample touches the wall as the radial stress is only possible to find in that moment.

3.5 Risk Assessment

A risk assessment was conducted prior to the laboratory work. This is an important part of the preparations for the experiments, in order to determine the quantitative and qualitative risks related to the activity. Potential hazards were identified and the risks associated with them were evaluated. Countermeasures for the potential hazards were suggested in order to reduce the risks. The assessment can be found in Appendix B.

Chapter 4

Results

The results obtained from the tests will be presented in this section. Only the most relevant results will be displayed. The full results are attached in Appendix C.

Three experiments were executed in order to study the creep behaviour, permeability response, acoustic, mechanical and elastic properties of a shale material when exposed to different fluids. The tests were carried out with a step wise loading path, using different fluids. Strain was calculated to find the deformation rate for each load increment, as well as to study how the creep behaved. Differential pressure tests were conducted to see how permeability was affected by the change in axial force and fluid exposure. Ultrasound measurements were recorded to perform velocity analysis and to find elastic properties of the samples when possible.

The recorded data was processed and analyzed using Excel spreadsheets. The data is mainly presented in graphs, as a function of time or axial stress.

4.1 CT Scan

All three samples were scanned using a CT machine after they had been tested. The sample for the third experiment was also scanned prior to testing. The results are displayed as images of vertical and horizontal cross sections of the samples. More images of each sample can be found in Appendix C.

(a) Vertical cross section

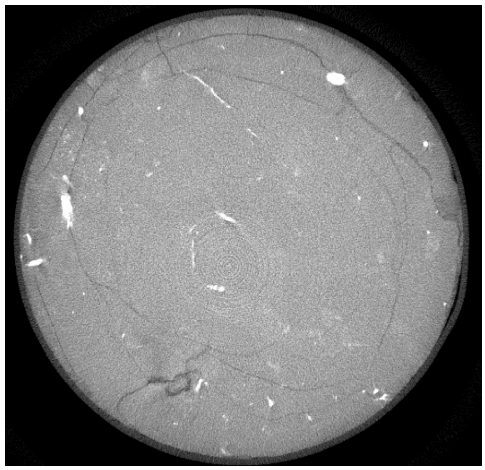

(b) Horizontal cross section

Figure 4.1: CT Scan of sample 1 after testing.

(a) Vertical cross section

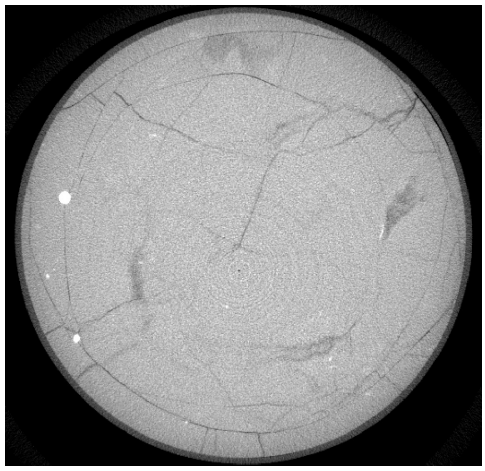

(b) Horizontal cross section

Figure 4.2: CT Scan of sample 2 after testing.

(a) Vertical cross section

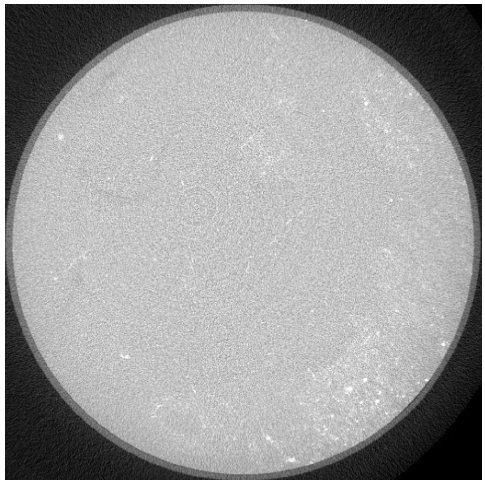

(b) Horizontal cross section

Figure 4.3: CT Scan of sample 3 before testing.

(a) Vertical cross section

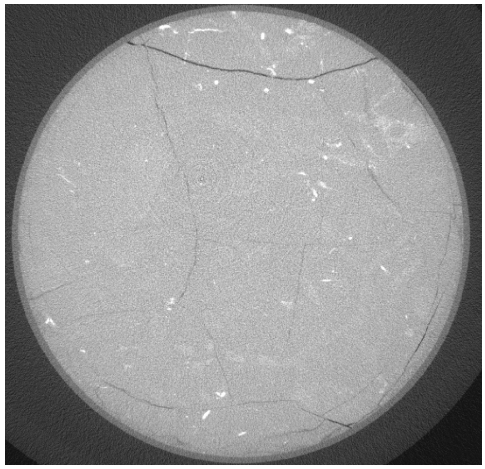

(b) Horizontal cross section

Figure 4.4: CT Scan of sample 3 after testing.

4.2 Anisotropy

The calculated velocity from the bench top acoustic test was plotted against angle in Figure 4.5.

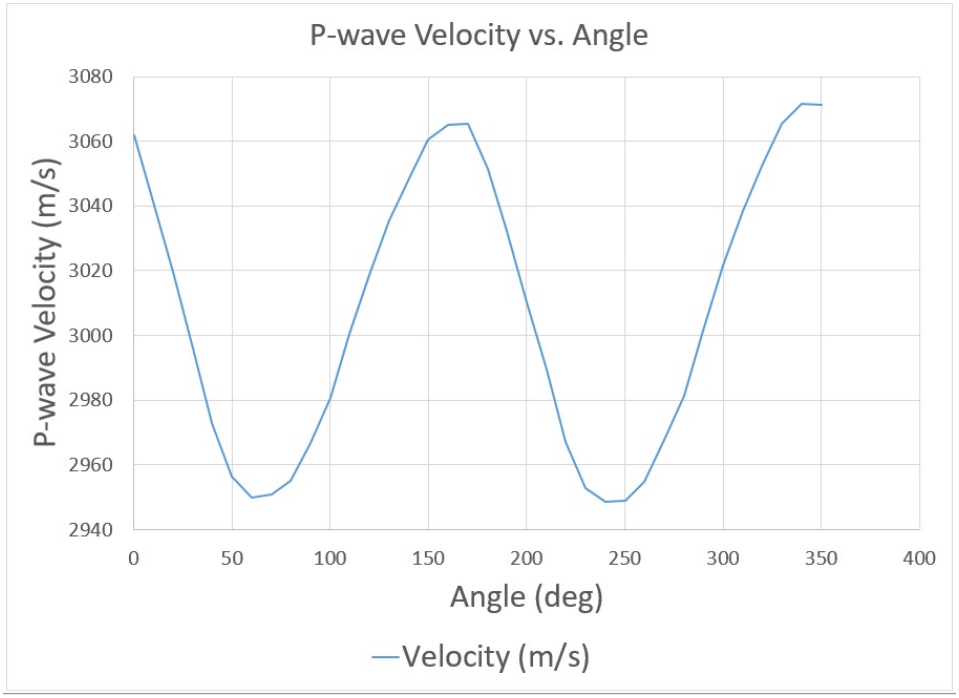

Figure 4.5: The result from the bench top ultrasonic test.

4.3 Creep Test with Stepwise Loading Path

Figures 4.6, 4.7, 4.8 shows an overview of all the data recorded with CatMan from each test as a function of time.

The dark blue line represents the pump data, the yellow line the axial stress applied to the samples, the green line the axial displacement of the samples, the orange line the differential pressure measurements, the grey line the temperature in the laboratory and the light blue line shows the measured radial stress of the samples.

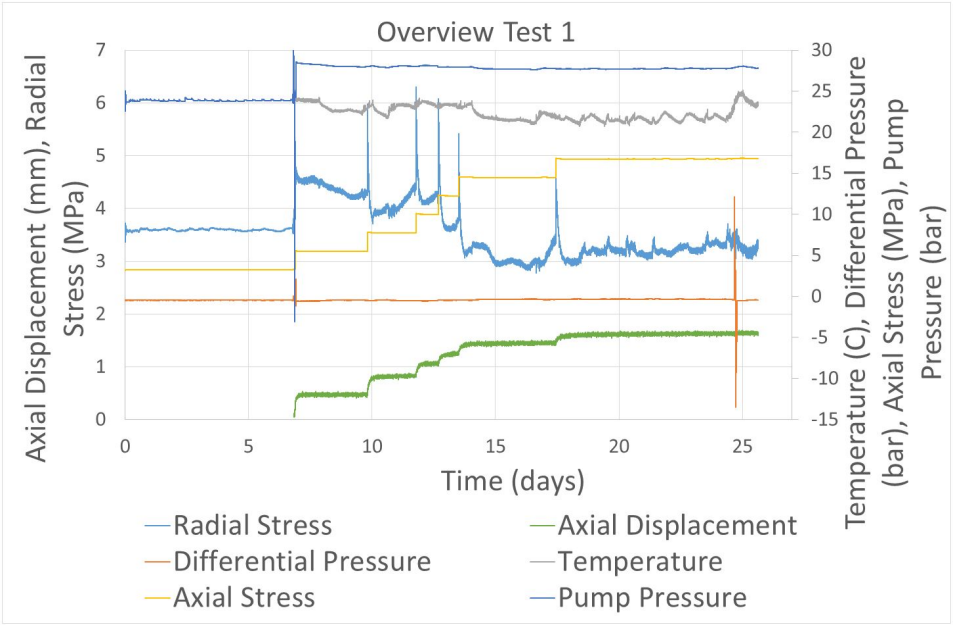

Figure 4.6: Measurements from the first test.

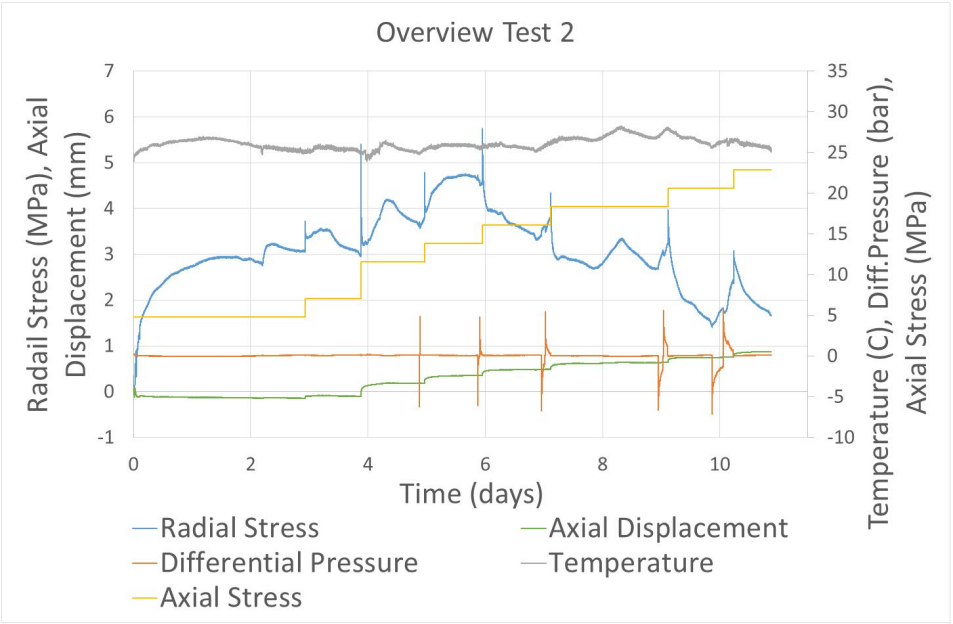

Figure 4.7: Measurements from the second test.

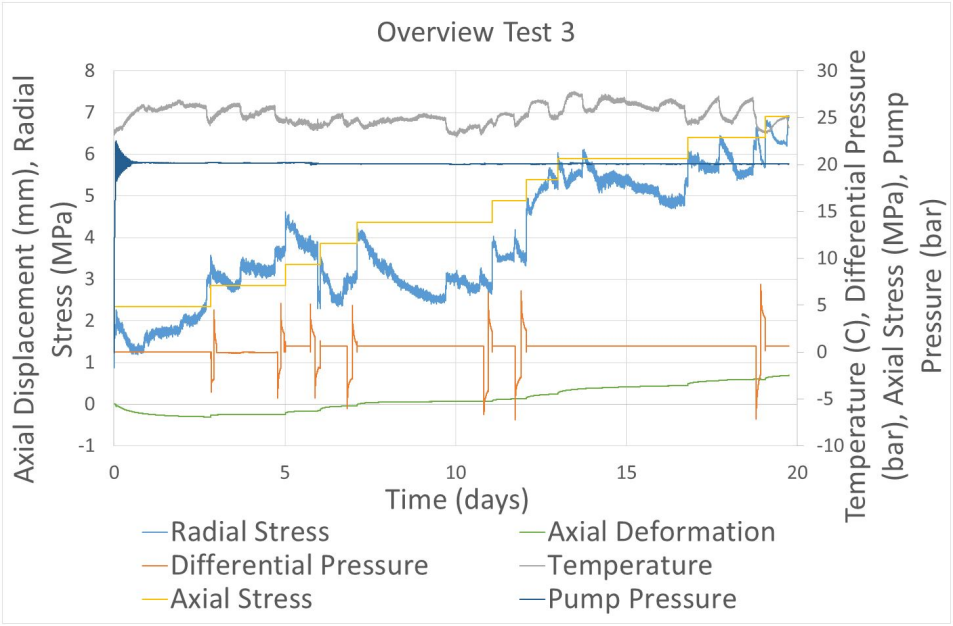

Figure 4.8: Measurements from the third test.

4.4 Strain Measurements

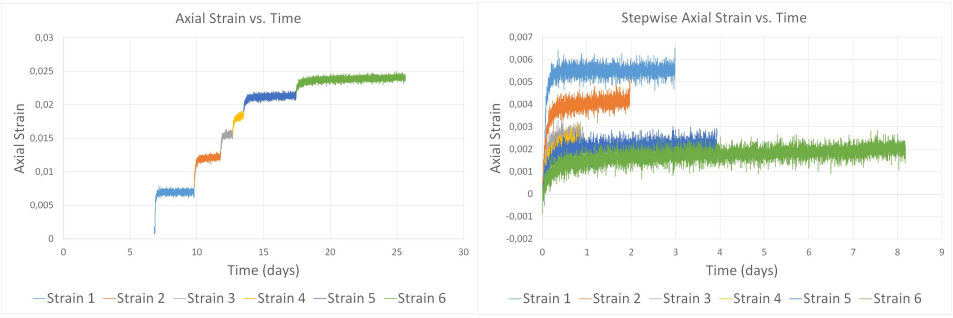

(a) (b)

Figure 4.9: (a) the total stepwise strain as a function of time for the first test; (b) the strain for each load as a function of time for the first test.

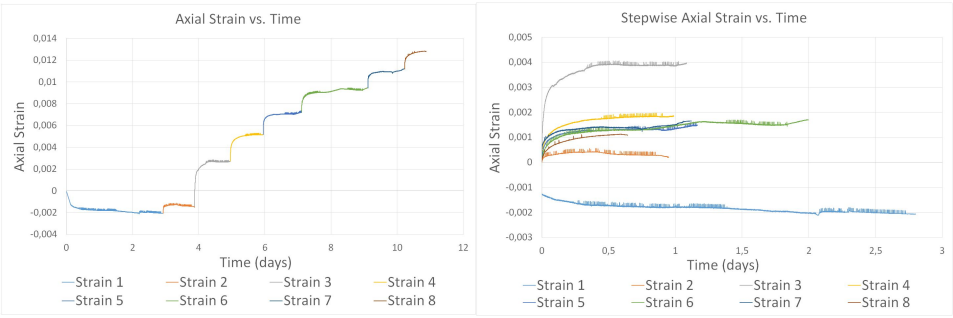

(a) (b)

Figure 4.10: (a) the total stepwise strain as a function of time for the second test; (b) the strain for each load as a function of time for the second test.

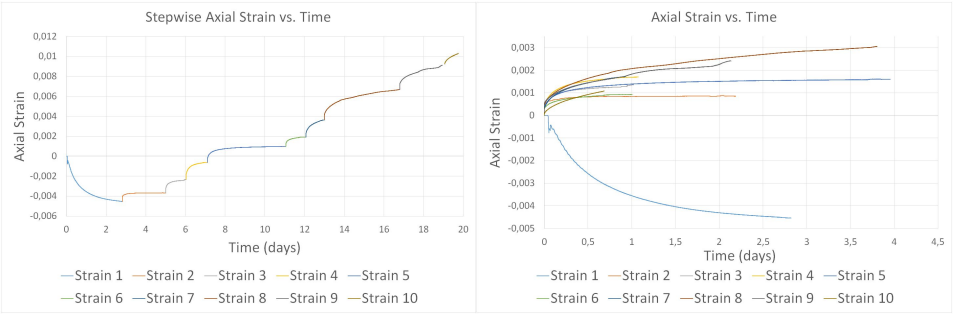

(a) (b)

Figure 4.11: (a) the total stepwise strain as a function of time for the third test; (b) the strain for each load as a function of time for the third test.

Strain was calculated using Equation 3.5. Figure 4.9 (a) shows the total step wise strain of the first test as a function of time, while (b) shows the strain for each load increment as a function of time for the first test. Figure 4.10 and 4.11 shows the same results for the second and third test.

A plot of the axial stress as a function of axial strain for all three tests can be seen in Figure 4.12, as can a plot of radial stress versus axial stress of all three tests in Figure 4.13.

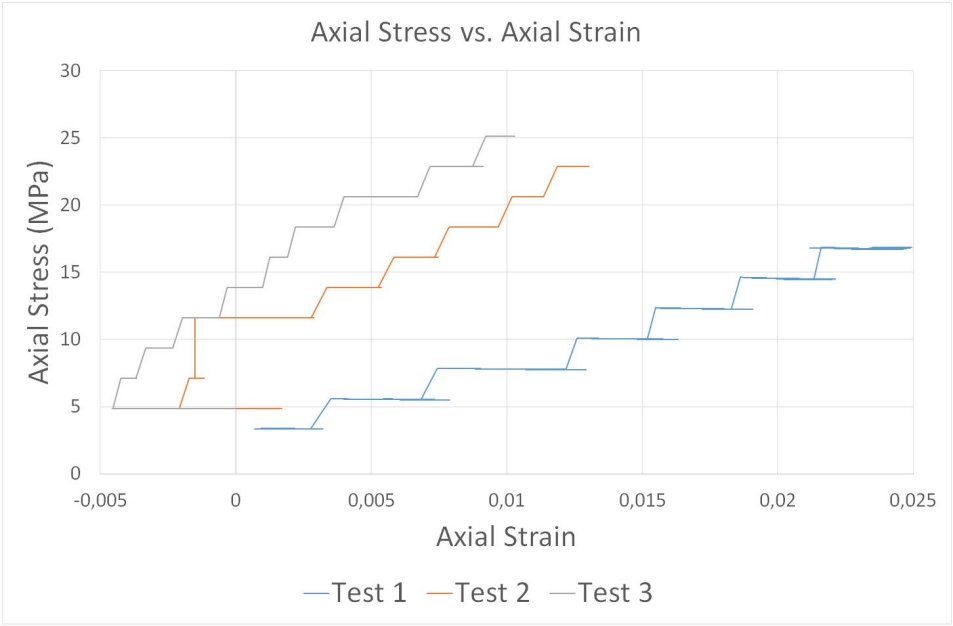

Figure 4.12: The axial stress for each test plotted versus axial strain.

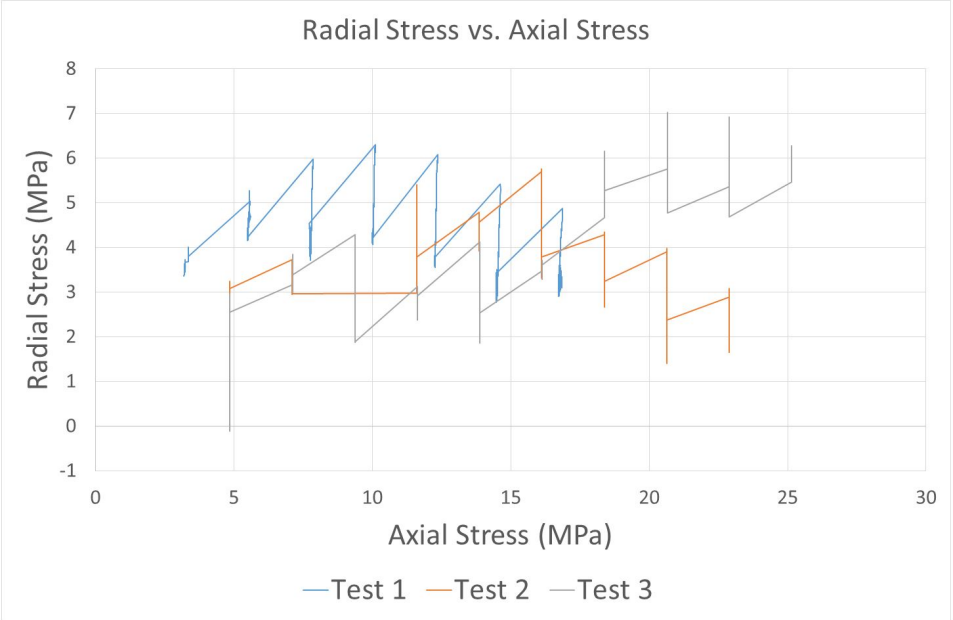

Figure 4.13: The radial stress for each test plotted versus axial stress.

4.5 Creep and Deformation Rate

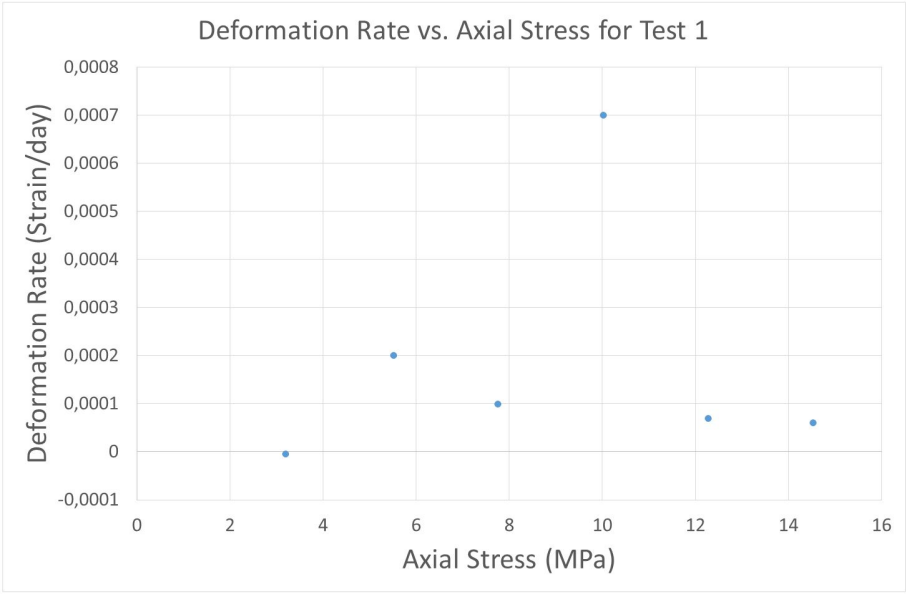

Figure 4.14: Deformation rate plotted versus axial stress for the first test.

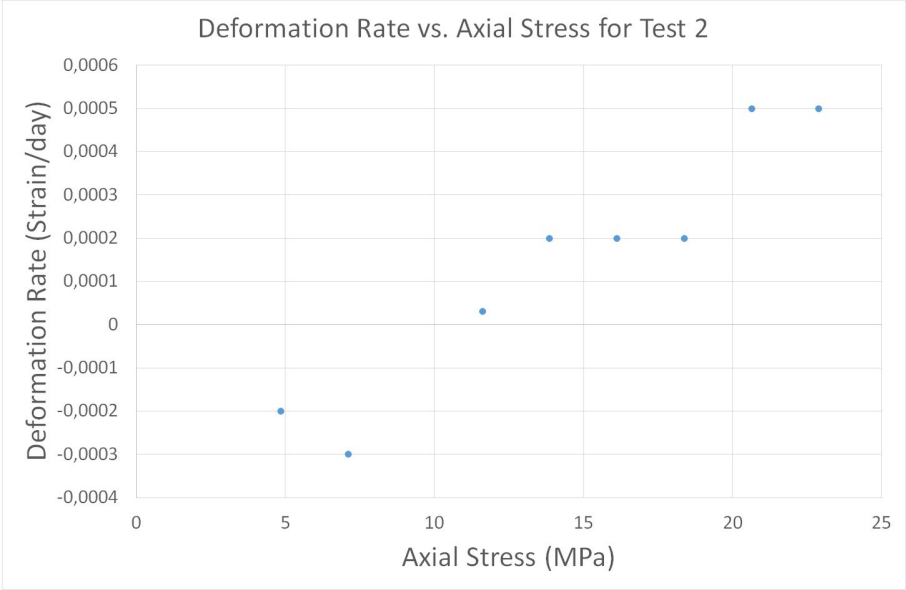

Figure 4.15: Deformation rate plotted against axial stress for the second test.

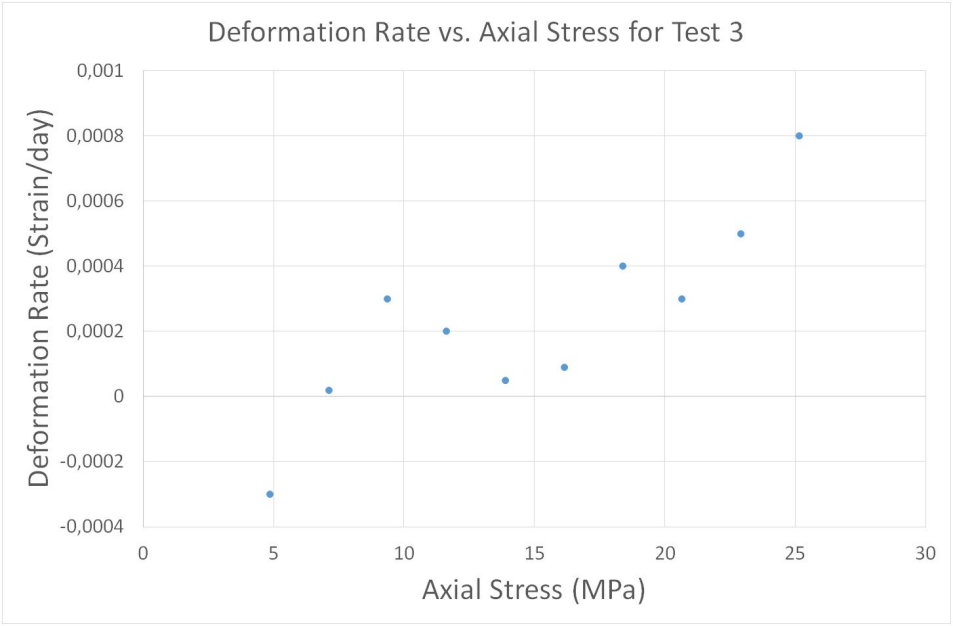

Figure 4.16: Deformation rate plotted against axial stress for the third test.

The deformation rate was plotted against the axial stress for each test, as can be seen in Figure 4.14, 4.15 and 4.16. These were calculated according to Section 3.4. A Table with the results and more plots can be found in Appendix C.

4.6 Permeability Measurements

Equation 3.8 was used to calculate the permeability during each test. For all three tests, a graph of the average differential pressure versus time was plotted and is attached in Appendix C. Figure 4.17 and 4.18 shows plots of the permeability versus the axial stress for the second and third test. In Appendix C, Tables with all the values used for each permeability calculations are also attached.

Only one differential pressure test was done in the first test, resulting in a permeability of approximately 6.8 mP. For the second and third test, several differential pressure tests were done throughout the duration of the tests.

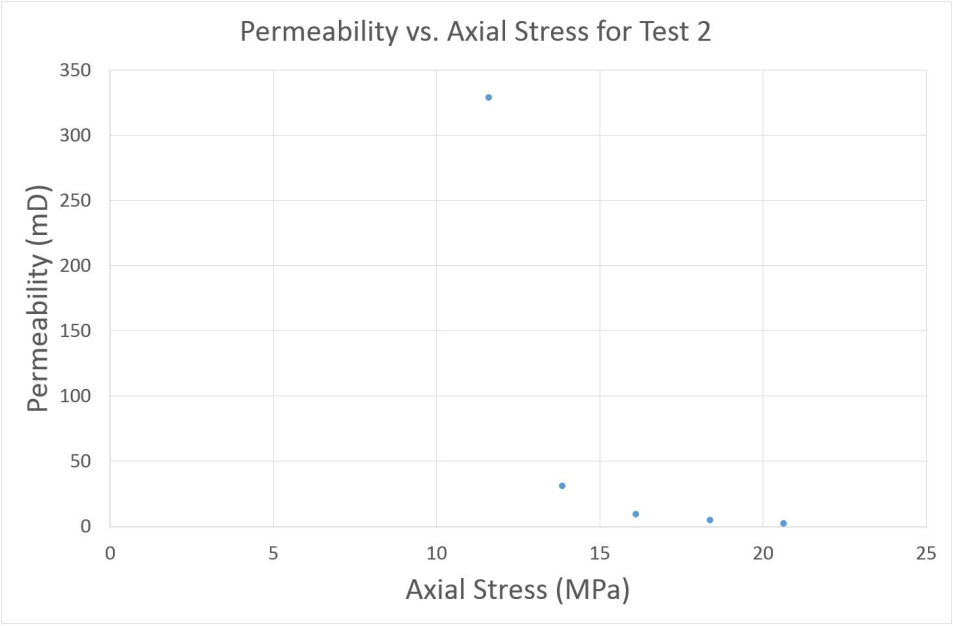

Figure 4.17: Permeability during the second test plotted against axial stress.

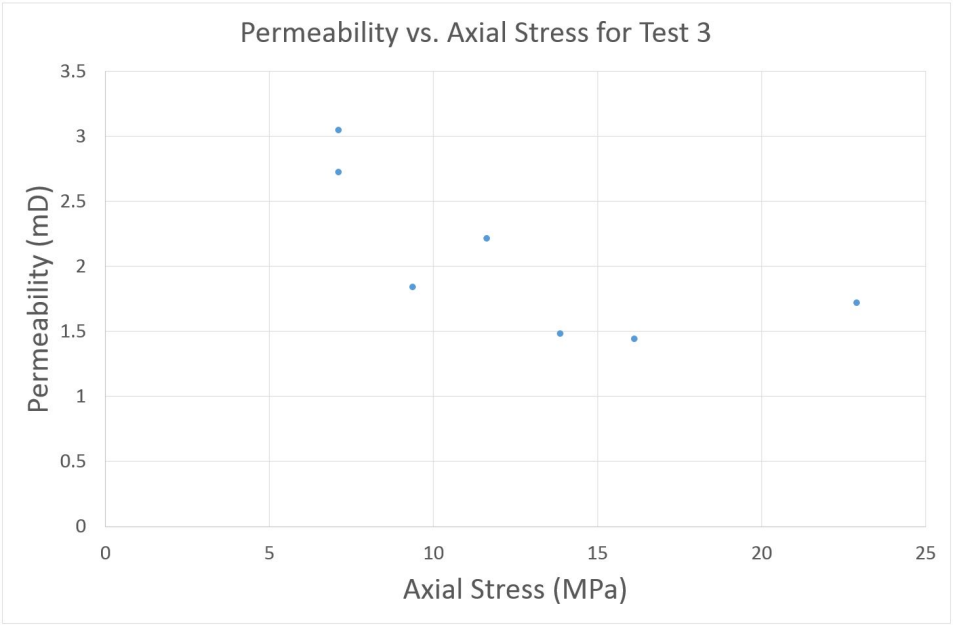

Figure 4.18: Permeability during the third test plotted against axial stress.

4.7 Ultrasound

The velocities calculated from the travel times of the transduced P- and S-waves are displayed in this section. Several P and S-wave frequencies were transduced for all three tests. They were all interpreted and the ones giving the best results are shown here. More plots and interpretation tools are attached in Appendix C. For all the vertical velocity calculations the travel time from the sintered disks were subtracted from the resulting arrival time to be able to get an as accurate result as possible for the shale itself. An electrical cut on the sixth day of the first test created problems with the logging and affected the results. Therefore the data from the first part of the first test was lost.

Horizontal P-wave

A horizontal P-wave of frequency 1 MHz was transduced for the first test while 500 kHz was transduced for the second and third test. A horizontal P-wave response was found for all three tests. They were plotted against time and axial stress as can be seen in Figure 4.19 and 4.20, respectively. More plots for each individual test can be found in Appendix C.

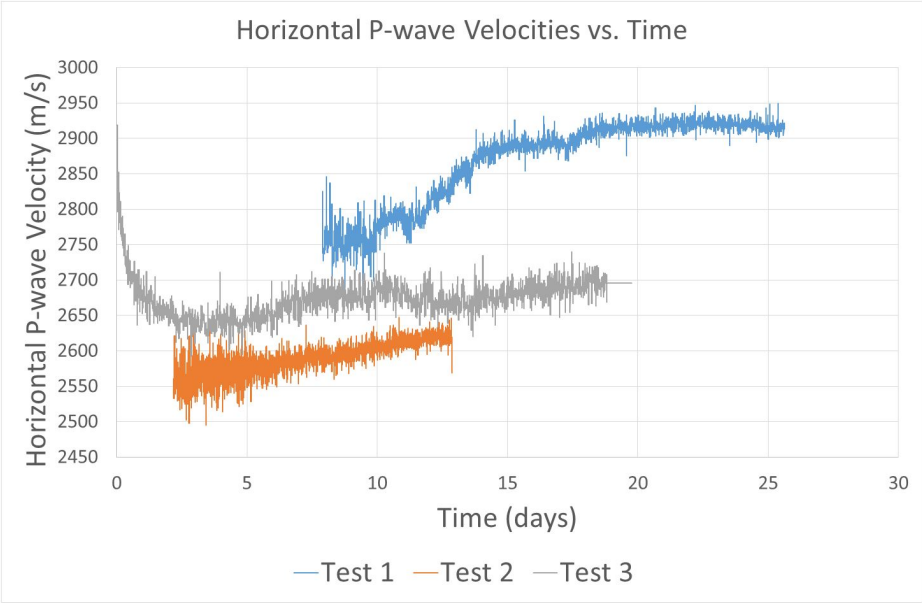

Figure 4.19: Horizontal P-wave velocities for the three tests versus time.

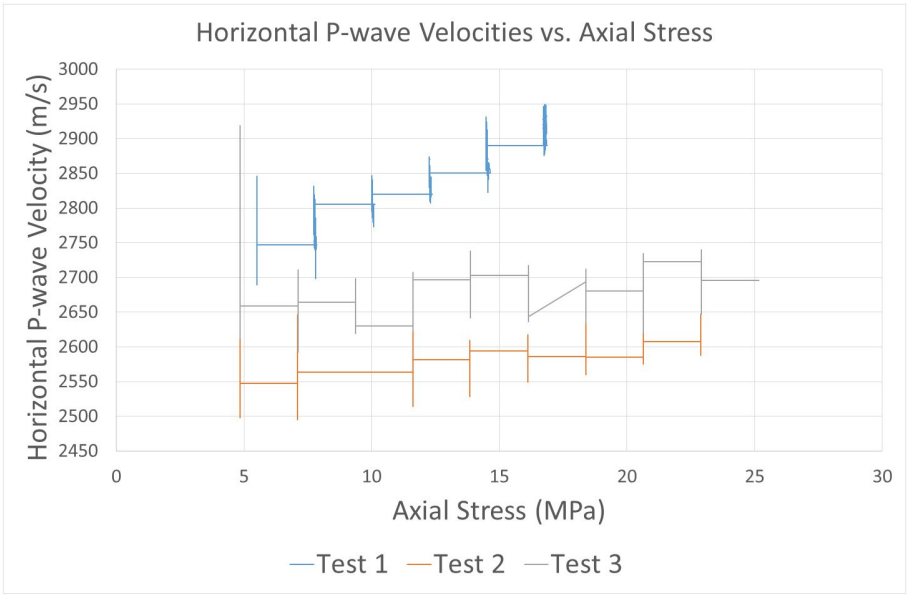

Figure 4.20: Horizontal P-wave velocities for the three tests versus axial stress.

Vertical P-wave

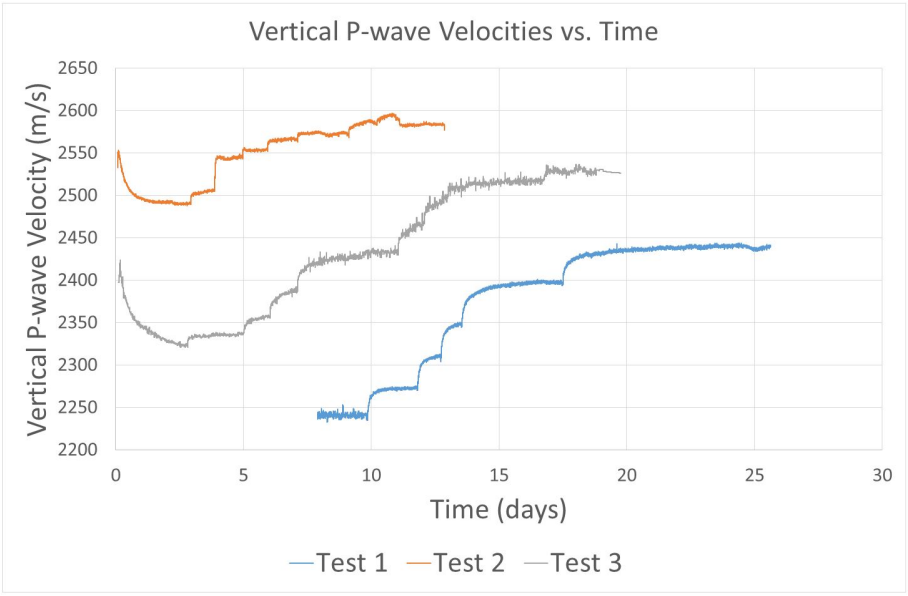

Figure 4.21: Vertical P-wave velocities for the three tests versus time.

A vertical P-wave of 500 kHz was transduced for all three tests. A vertical P-wave response was found for all three tests and was plotted against time and axial stress in Figure 4.21 and 4.22, respectively. More plots for each individual test can be found in Appendix C.

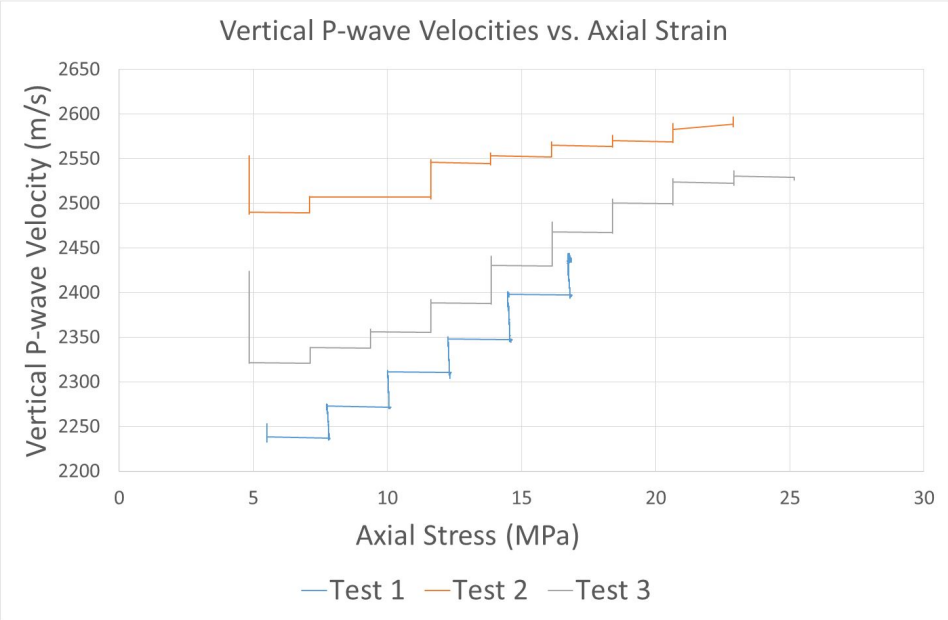

Figure 4.22: Vertical P-wave velocities for the three tests versus axial stress.

Vertical S-wave

A 250kHz vertical S-wave was transduced for the first test while 75 kHz, 125 kHz and 250 kHz was transduced for the second and third test. No S-wave was found for the first test (see Appendix C for further analysis) while an S-wave may have been found for the second and third test.

Figure 4.23 and 4.24 shows the vertical S-wave velocities plotted against time and axial stress, respectively. More plots for each individual test can be found in Appendix C.

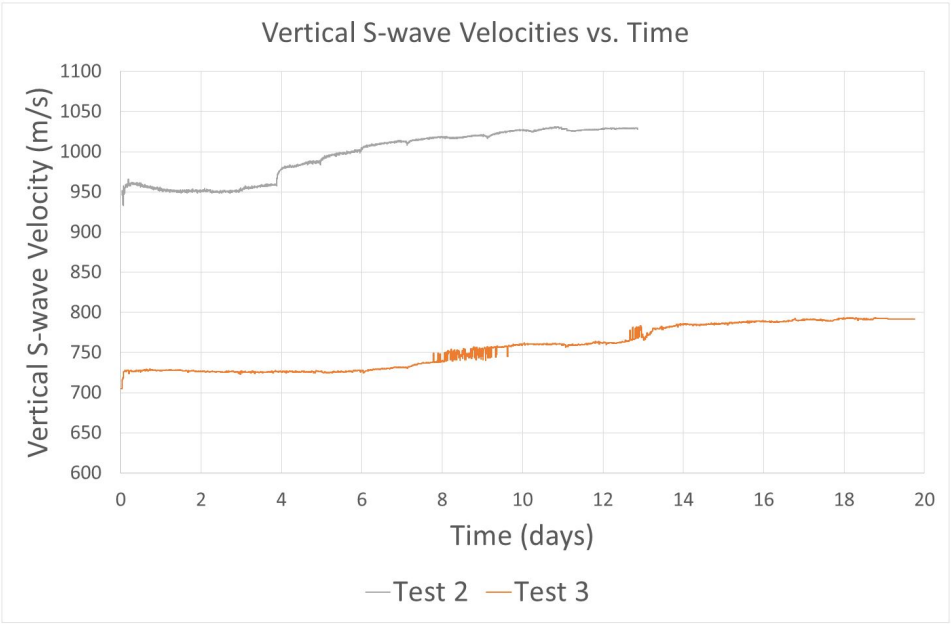

Figure 4.23: Vertical S-wave velocities versus time.

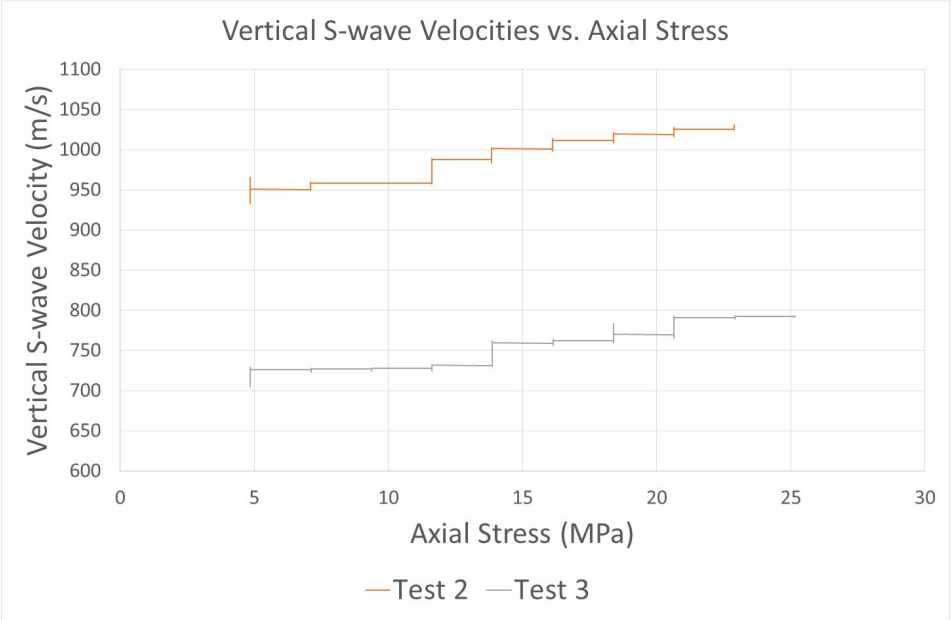

Figure 4.24: Vertical S-wave velocities versus axial stress.

4.8 Elastic Properties

The impedance, bulk moduli, shear moduli, Poisson's Ratio and Young's moduli were all calculated for the tests were P- and S-waves were found. The equations used can be found in Section 2.3. Only the results with a meaningful correlation are displayed in this section. Further calculations can be found in Appendix C.

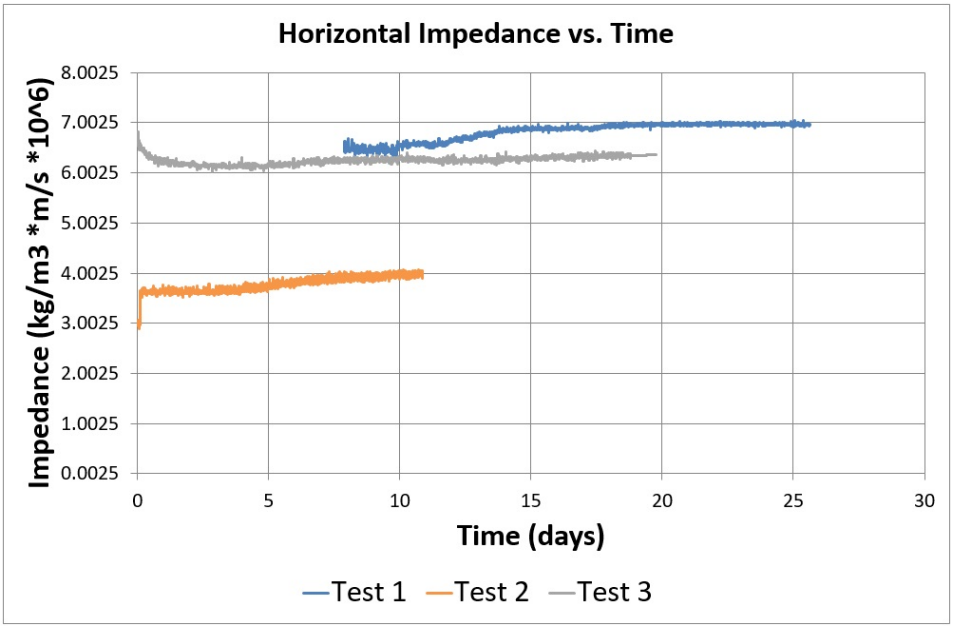

Figure 4.25: The horizontal P-impedance of the three samples.

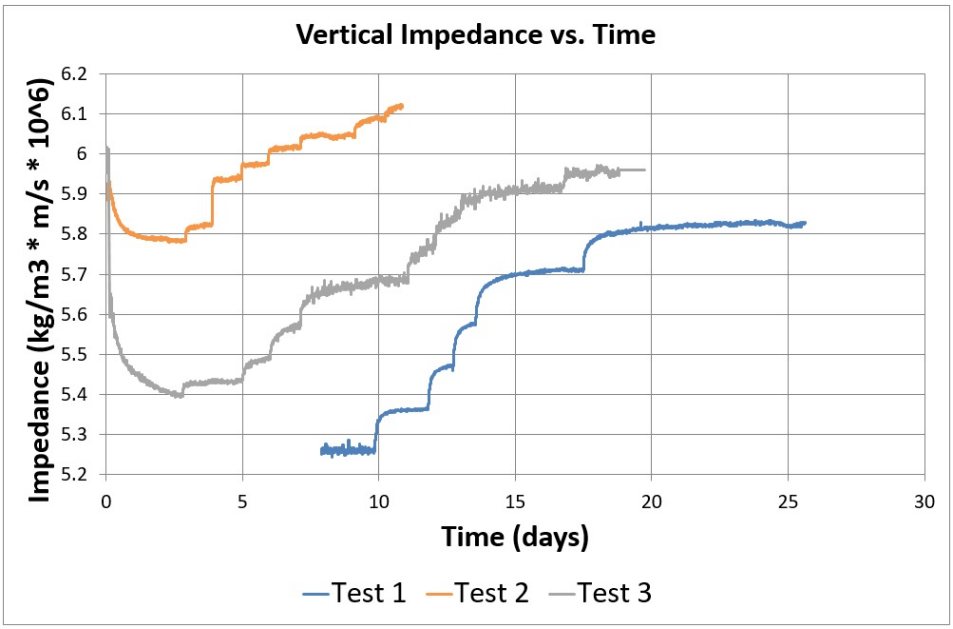

Figure 4.26: The vertical P-impedance of the three samples.

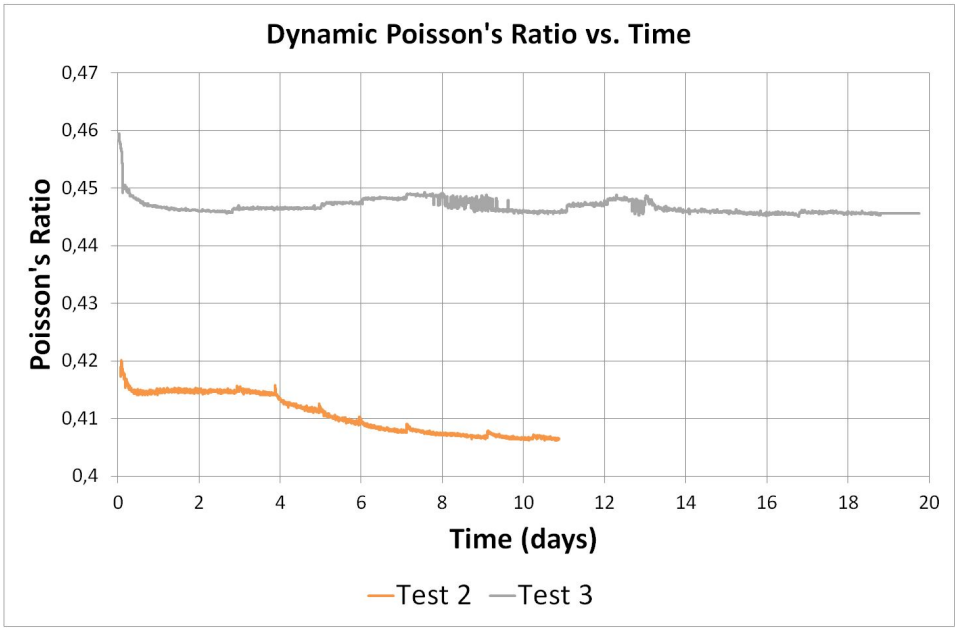

Figure 4.27: The results of the dynamic of Poisson's Ratio.

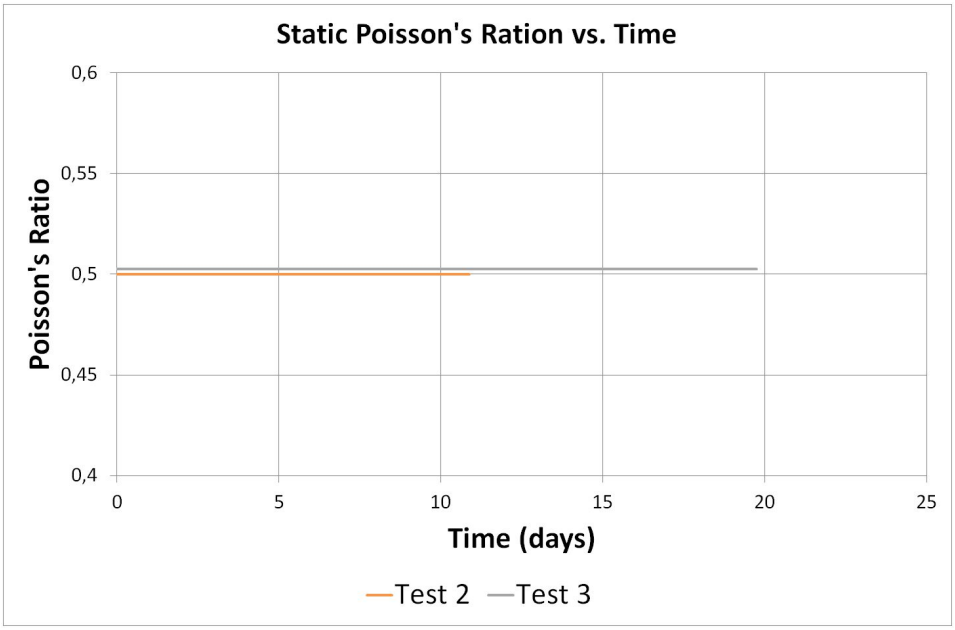

Figure 4.28: The results of the static of Poisson's Ratio.

Chapter 5

Discussion

This section will discuss what is thought to be the most important results from this experiment. The tests themselves can be difficult to execute precisely and analyzing the data can be complex. Several factors have to be taken into account and it is important to view the measurements relative to each other in order to see if there are some correlations between them. There were several potential sources of error that will be discussed later in this section.

5.1 Sample Material

The CT scans were taken to see how heterogeneous the samples were. Mineralogy affects the results of the experiments and it was important to see if the samples were very different as the tests were to be compared with each other. The scans were also done to see if fractures would be created or sealed off during the stepwise loading tests or when exposed to the different fluids.

As the third sample was the only one scanned before testing, it will be used as a reference for all the tests by assuming the samples were quite similar. In Figure (b) 4.1 to 4.4 the dark grey areas around the sample represents the plastic container the samples were stored in and are therefore not part of the samples.

As can be seen in Figures 4.1 to 4.4, areas of bright white are present within the samples. These are probably minerals of a higher density than the surrounding

minerals. When looking at the vertical cross sections it is also possible to see some horizontal layering throughout all of the samples that indicates that the material is anisotropic. The three samples seem within range of what is comparable.

The first sample was exposed to 3.5% NaCl and several fractures are observed (Figure 4.1) after testing. On the vertical cross sections it seems the fractures are denser towards the sides of the sample than in the middle. The possible exception is the lower third of the sample. This can also be seen on the horizontal cross sections. A higher density of short fractures can be observed on the edges of the samples. The vertical cross sections do not show a high density of fractures on the edges. The fractures on the sides of the samples were probably created due to the pore pressure changes within the sample.

The second sample was exposed to 20% KCl and one can observe a much higher density of fractures (Figure 4.2) compared to the sample from the first test. In this sample the fractures propagated all the way to the center, which can be seen on both the horizontal and the vertical cross sections. There does not seem to be any small fractures on the edge of the samples.

The third sample prior to testing shows one distinct fracture traversing the sample more or less horizontally on the vertical cross section (Figure 4.3(a)). Some smaller fractures are also present in the top part of the sample. These fractures were probably created either when extracting the material from the well or when drilling out the sample from the material. The vertical cross section also show that the lower parts of the sample were more or less free from fractures before testing while the upper part was not.

After having been exposed to fresh water and axial stress increase, the fracture density of the third sample changed significantly (Figure 4.4). Several new fractures are now present throughout the whole sample. The big fracture observed across the sample before testing did not seal itself off. Along the sides of the sample one can see small fractures propagating a short distance towards the center of the sample. The density of the fractures on the edges is higher than in the rest of the sample.

Many of the fractures seem to propagate diagonally through the samples, indicating shear failure. Some fractures are also horizontal and some vertical. When looking at the vertical cross sections, fractures in all the samples seem to propagate alongside the edges of the samples. This indicates that pore pressure changes have occurred in all three tests.

One can see that the sample exposed to KCl has a higher density of fractures than the other two samples after testing. The fractures also seem to propagate deeper towards the center than in the other two cases. As the total axial stress applied to the three samples were quite similar, it indicates that the KCl breaks up the sample more than NaCl and freshwater.

The NaCl and fresh water sample have a higher density of smaller fractures on the edges than the KCl. The fractures are short but dense and can indicate that a greater chemical reaction occurred in this samples compared to the test using KCl as a fluid.

The bench top acoustic measurements were done to see how horizontally heterogeneous the material was prior to testing. As can be seen in Figure 4.5, the velocity changes with the orientation of the sample. This means there is a horizontal anisotropy. As no stress analysis was done on the material it is difficult to know whether the anisotropy is a result of *in situ* stresses or deposition. Open fractures in the sample may also have affected the ultrasound response.

5.2 Creep Test with Stepwise Loading Path

Figure 4.6, 4.7 and 4.8 shows an overview of all three tests. In all the Figures, the light blue lines show the results from the uniaxial deformation sensors that represent the radial stress of the samples. The green lines show the axial displacement of the sample while the yellow lines show the axial stress. The orange lines show the differential pressure measurements done throughout the differential pressure tests, while the grey lines show the temperature of the laboratory close to the oedometer cylinder. The dark blue lines show the manually set pore pressure.

The first test used 3.5% NaCl as fluid. The idea was to use the same fluid as the initial pore fluid, but based on the results from previous experiments there is an uncertainty as to exactly what that is.

Some data from the first few hours of the first test is missing so it is difficult to know exactly when the sample had contact with the wall of the oedometer cylinder (Figure 4.6). Since the radial stress was already at 3.5 MPa after a few hours, it is assumed that the sample was in contact with the cylinder walls very quickly. The radial stress increased when the second load increment was put on but then started to steadily decrease before it stabilized in the last part of the test. This

was first thought to be a defect on the strain gauges. Since the strain gauges seem to react every time a new load is put on, there has to be some contact between the wall of the oedometer cylinder and the strain gauges. This gave reason to believe that the radial stress response is accurate.

The increase in radial stress may be related to pore pressure changes. When a new load is put on the sample, a pressure buildup is created. It may take some time before the sample finds a new pore pressure equilibrium that eventually will result in a decrease in pore pressure. Another explanation may be that advection occurred after a certain amount of time. The sample may have broken up sufficiently under stress to increase the flow through the sample, giving the material a better exposure to the fluid. A water and/or ion exchange may then have happened more easily, causing the sample to shrink. This would eventually result in a decrease in the radial stresses. The observation of the samples before testing and the CT scan after testing both show the presence of a fracture that traverses the whole sample approximately horizontally. This may have played a role in the radial stress changes of this sample. Figure 4.6 shows a correlation between the temperature of the laboratory and the radial stress.

The calculated axial strain shows a stepwise increase in total strain. The change in strain decreases towards the end of the test compared to the beginning of the test (Figure 4.9). The first strain step has a strain increase of approximately 6 $milliStrain$ while the last strain step only has a strain increase of 2 $milliStrain$. The first strain step increases fast and then flattens out while the other strain steps show slightly different trends.

The deformation rate throughout the test is quite stable (Figure 4.14). Strain 3 and 4 likely gives a different deformation rate than if they had had longer time to stabilize. Looking at Figure 4.9 (b), several of the strain steps show a slight increase in slope. Based on this some creep is believed to happen in this test. Had the test been run for a longer time, the sample been exposed to a higher axial stress or exposed longer to the fluid, the creep rate may have increased.

Only one differential pressure test was taken during the first test (Figure 16. It was at the end of the test and gave a permeability of 6.8 mD. It is difficult to know how the permeability changed throughout the test.

The second test used 20% KCl as fluid, which has a high concentration of K^+ ions. Exposure to potassium is known to cause large contractions which generally

has a stabilizing effect on shale material. However, there have been field experiences where higher concentrations of potassium have led to a decrease in stability. A high concentration was therefore used in this test to see if it could result in destabilization and creep.

In the beginning of the test the radial stress increased stepwise with the stepwise loading path (Figure 4.7). Then, approximately at day six, the radial stress started to decrease even though the axial stress applied continued to increase. This was again thought to be a defect in the strain gauges, but the sand check (3.2.5) showed a normal behaviour of the strain gauges.

The LVDT measurements show that axial swelling occurs at the start of the test. This suggests to believe the sample swelled radially as well, resulting in an increase in radial stress. The swelling may have occurred because the sample was badly saturated and a pore pressure built up when exposed to the KCl. After the sample reached new pore pressure equilibrium the radial stress would decrease.

Another reason for the decrease in radial stress may be that it took some time before the potassium started to react with the shale. As seen on the CT scan the sample had a lot of fractures after testing. When the sample broke up the potassium would flow more easily through the sample. It would then react with the shale and result in a reduction in radial stress as the sample started to shrink. Figure 4.7 definitely shows a correlation between the temperature and the radial stress.

Except for the swelling in the start of the test (Figure 4.10), the change in strain for the last five strain measurements are quite similar, approximately 1.5 *milliStrain*. The first and second strain step show a decrease in strain as the sample swells axially. The third strain step had a much higher strain change than any other strain step (approximately 4 *milliStrain*) that is probably due to the high increase in axial stress that happened at this point (see Figure 4.7). Where the first five strain steps seem to flatten out over time, the last three steps show a more unstable trend. This made it difficult to find an accurate trend line for the deformation rate. Overall the deformation rate seem to increase over time, indicating that the sample became increasingly fractured and unstable. None of the strain steps in Figure 4.10 seem to indicate creep although Figure 4.15 show a greater deformation rate than the first test. The last couple of steps may show a tendency for creep although not enough time was given for each step to see a certain creep trend.

Differential pressure tests were done throughout the second test (Figure 4.17). The results show a significant difference in permeability between the first and last test. The first differential pressure test resulted in a very high permeability which quickly decreased. The permeability slowly decreased from this point on. Sintered disks were not used for this test which may have affected the differential pressure tests and the general distribution of fluid. The decrease in permeability indicates that the sample shrinked throughout the test.

The third test used fresh water as fluid, which is known to make shales swell. Since the activity of the pore fluid in the shale is lower than the activity of water, water would presumably be sucked into the shale and make the shale swell.

Due to what seemed to be a correlation between the temperature and the radial stress in the first and second test, a correction of the strain gauges was made prior to the third test. This way the radial stress could be corrected although some correlation may still occur.

The radial stress measurements for the third test shows a more consistent increase throughout the test (Figure 4.8). After increasing in the beginning of the test, the radial stress decreases a bit before it increases again. The decrease in radial stress in the middle of the test may be explained by pore pressure changes. As can be seen from the axial displacement the sample swells in the beginning of the test, indicating that this sample was not fully saturated when the test started as well. The sample probably swelled radially as well. When the sample got more saturated, pore pressure equilibrium was reached. This resulted in the compaction of the sample and the radial stress decreased.

In the beginning of the test the sample swelled drastically (approximately -4.5 $milliStrain$) before enough axial force was applied for it to start to compact (Figure 4.11). The strain steps two to six show a low change in strain when axial stress is applied (between 0.5 and 1.5 $milliStrain$) and also have a relatively low deformation rate. The last four strain steps, however, show an increase in deformation rate. As the radial stress also increases towards the end of the test, it may indicate creep behaviour.

Differential pressure tests were done throughout the third test (Figure 4.18). The results show that the permeability decreases as the axial stress increases.

5.3 Ultrasound

Several P- and S-waves were transduced to look at the acoustic properties of the samples. Due to too low signal to noise ratio, a power cut and low availability of the ultrasound equipment, some data from the first part of the first and second tests is missing.

The signal to noise ratio of the horizontal P-wave was very low for all three tests and the arrival time was difficult to pick (see Appendix C). This may be due to bad contact between the transducer and the sample, although precautions were made to make sure the contact was good. Grease was put on the transducers to enhance the contact and they were tightened as hard as possible into their sleeve. The bad signal may otherwise be due to a bad connection between the sample and the oedometer wall, although other measurements show good contact between these two early in every test.

The response was picked at approximately 20 μs, which after correction was close to the rough calculations done in Section 2.5. All three horizontal P-wave velocities increased throughout each test. Since some data is missing from the beginning of the first and second test it is difficult to compare the start velocities. Preferably these should be close but differences in the samples heterogeneity may have affected the initial velocity. The horizontal P-wave velocity from the test using KCl was the slowest, followed by the fresh water test and the NaCl test (Figure 4.19. The salinity of the KCl could increase the P-wave velocity but in this case it is believed to affect the sample more by compacting it and create fractures. The CT scan shows that the sample has many fractures. The first test using NaCl had a much bigger compaction than the two other tests that may be the reason for why the horizontal P-wave velocity was the fastest. The horizontal P-wave velocity of the third test started very high before it slowed down drastically and stabilized at a slower speed. An explanation for the high velocity in the start could be that it was a response from the steel oedometer cylinder, or a combination of steel and shale response, which would have a faster travel time than through the shale alone. This test used fresh water as a fluid, which should affect the P-wave velocity to be slower rather than faster. The first test has the biggest change in velocity. The two other tests show a rather small change in velocity.

Figure 4.20 showed that the first test (NaCl) had a bigger response to the change in axial stress than the two other tests. The second test (KCl) shows a slow, steady

increase in velocity as the axial stress increases, while the third test (fresh water) has variation in velocity change as axial stress increases.

The signal to noise ratio is much higher for the vertical P-wave (Figure 4.21). In the vertical direction, the second test using KCl as a fluid has the fastest P-wave velocity, followed by the third and first test. This is the opposite of the horizontal P-wave velocities, indicating that different properties affect the vertical P-wave velocities in this direction. If it is assumed that the NaCl and KCl salts have the same impact on P-wave velocity, it would explain the high velocity if the second test (KCl) as this test used a higher concentration. The high concentration of fractures may also have affected the velocity as fluid may have been present in these fractures. The first test (NaCl) shows an unexpectedly low velocity compared to the two other tests. NaCl should also have a positive impact on a P-wave velocity. A higher velocity for the first test would also have been expected due to the greater compaction compared to the two other tests. Another explanation could be that different pistons were used for the first test. This should not be of importance, but may have affected the results.

The high reduction in the vertical P-wave velocity in the beginning of the second (KCl) and third (freshwater) test is probably a result of the swelling of the samples. A lot of water was probably absorbed into the samples as the pore pressure changed, reducing the velocity. When the samples started to compact, the water got pushed out or reacted with the material, resulting in an increase in the vertical P-wave velocity.

The first (NaCl) and third (fresh water) tests show a greater increase in velocity throughout the tests than the second test (KCl). As the KCl concentration in the pore fluid was high it may have increased the vertical P-wave velocity, although it is thought to affect the compaction more than the velocity. The potential increase may therefore have been lower than for the two other tests that were less affected by ions.

Although quite similar to the third test (fresh water), Figure 4.22 shows that the first test (NaCl) had a bigger vertical P-wave response to the change in axial stress than the two other tests. The second test (KCl) also shows a slow, steady increase in velocity as the axial stress increases.

A vertical S-wave was not expected to be found for either of the tests and turned out to be difficult to locate. Several frequencies were transduced to enhance the chance

of finding a satisfying result. Different interpretation methods within Speedy were used, see Appendix C for complementary Figures.

No S-wave was found for the first test (NaCl). Unfortunately none of the interpretation tools showed a response that could fit an S-wave response. See Appendix C for graphs. Because of the lack of S-wave response, the pistons in the oedometer cylinder were changed in case they were the issue. For the second test a response was likely found (Figure 4.23). As the first arrival time was difficult to pick, the zero crossing was used to get the most accurate pick of the response as possible (see Appendix C). The coloured amplitude of the waveforms shows a changing trend at the location of where the arrival time was picked, which enhances the likelihood for actually having an S-wave response (see Appendix C). The wave picked seems to correlate well with the axial displacement measurements and the velocity calculated is close to the expected values (Section 2.5).

A vertical S-wave was also picked for the third test. This was more difficult to find and resulted in a slower vertical S-wave velocity than the second test, although it was not far from the expected velocity. It is uncertain if this is an S-wave response or not, especially since it does not seem to correlate as well with the applied axial stress as the S-wave picked for the second test (see Appendix C).

Several dynamic and static elastic properties were calculated but not all gave expected correlations. Only the impedance and Poisson's ratio seem to be within the expected range (see Appendix C for results of Young's moduli, shear moduli and bulk moduli). The horizontal impedance is slightly lower than the vertical impedance. Both are in the lower spectrum of what was expected for this shale (see Section 2.3). Poisson's ratio was calculated both dynamically and statically. The dynamic calculations show a slightly lower result than the static, but they are both close to 0.5 that may indicate that the material is well saturated.

5.4 Summary

The setup used for this experiment is supposed to simulate downhole conditions. As the deformation in this setup is happening outwards to close a gap between a sample and the oedometer cylinder, it is not directly comparable to an annulus where the formation creeps inwards. Results will vary with setup, but hopefully some results can be used from this setup to get a better understanding of what

mechanisms may affect creep behaviour of this specific shale.

All three samples have an enhanced density of fractures after testing than prior to testing. Both the deeper fractures and the small fractures on the edges of the samples indicate this. It is difficult, however, to know if it is axial stress, reaction with fluid or a combination of these that creates the fractures. The small fractures on the edges may have been created by a fluid reaction, while the longer, deeper fractures may have been created by the axial stress. The longer fractures may have opened for the fluid to flow further into the samples.

The first (NaCl) and second (KCl) test showed an increase in radial stress followed by a decrease while the third test (fresh water) showed an increase. As the first and second tests used fluids with equal or higher salinity than the initial pore fluid of the sample this may explain the reduction in radial stress when the pore pressure equilibrium had stabilized. The third test used fresh water that has a higher activity than the samples pore fluid. This should result in swelling which it seems it did. The first and second tests both resulted in a radial stress of 4.6 MPa while the third test resulted in 6.5 MPa.

It is interesting to see how the reduction in radial stress happens for all tests around day six. It may be an indication that the samples took some time to create new pore pressure equilibrium. Although the response is smaller for the third sample using fresh water it is still present. As the sample compacts more the radial stress increases.

Figure 4.12 shows that the strain change of the first test is much higher compared to axial stress than for the two other tests. This could be because the NaCl brine used is closer in composition to the initial pore fluid than the two other tests and that the sample therefore took shorter time to find new pore pressure equilibrium. The swelling would then stop earlier and compaction would begin.

The deformation rate calculations are difficult to interpret as it is difficult to find a good fit for the trend lines. Most of the strain steps did not have enough time to stabilize or showed too large variations within one step. A sense of how much the sample deformed could all the same be found by looking at the deformation rate results and the slope of the change in strain for each step. The deformation rate results show that the third test has the biggest deformation rate, followed by the second and then the third test. The slope of the strain steps indicates that all three tests have a tendency to creep towards the end of each test. This indicates

that the samples were close to failure or had just reached it.

At the end of each test the permeability was calculated to be 6.8 mD, 2.5 mD and 1.7 mD for the first, second and third test, respectively. The first test shows a higher resulting permeability than the two other tests, which is strange when it is taken into account that this sample was more compacted than the two other samples. Sample three shows the lowest permeability although this sample was the least compacted. The fracture density may have affected the measurements. It is unfortunately difficult to see how the fractures propagate solely based on the CT scans but the second sample (KCl) had the largest density of fractures and should therefore theoretically show a higher permeability than the other samples. But the fractures may not be connected and would therefore not have an impact on the permeability.

The horizontal P-wave velocities indicate that there was contact between the sample and the oedometer walls quite early in the second (KCl) and third (fresh water) test. Except for the third test, the horizontal P-wave velocity is higher than the vertical P-wave velocity. This may indicate that anisotropy is higher in the vertical direction than the horizontal, which was expected. It may also indicate that the vertical P-wave velocity of the first test was wrongly picked. The first test showed the greatest compaction, which should increase the P-wave velocity. On the other hand, the permeability shows that the sample was more saturated than the other samples, which may have slowed down the P-wave velocity. This may also be the reason for why an S-wave was not found for this sample.

5.5 Sources of Error

When conducting experiments in the laboratory it is important to consider all possible sources of error that might have an impact on the final results. This section discusses the sources of error thought to be the most critical to this experiment.

Measurements of Sample

A slide caliper was used to measure the samples length and diameter. The diameter and length can vary throughout one sample depending on where measurements are performed. This can be taken into account by taking several measurements of the

same sample to determine an average diameter and length.

Desiccation of Sample

The shale formations rock properties can drastically change if the sample dries out. If it does the sample will have weakened and reach failure much faster than if properly saturated. Therefore it is important to keep the sample saturated at all times. In this case Marcol Oil was used.

For this experiment, the most critical stage regarding dry out would be when pictures of the sample were taken. Heat from the lights could easily affect the sample, so it was important to be quick and to put the core back into the fluid container as fast as possible. Another critical stage is when the sample is put in the oedometer cylinder and the rest of the setup has to be prepared before fluid can flow into the oedometer cylinder. As much as possible was therefore prepared before the placement of the sample so that this exposure time would be as short as possible.

Setup

There are different aspects of the experimental setup that should be taken into account to eliminate potential sources of error. It is important that the rotation screw placed in the intersection of the weight arm and the sample setup is oriented in such a way that the sample is centered under the arm. It is also of great importance that the cylinder, load cell and extensions are perfectly centered relative to each other and the weight arm.

Although the setup was created to exert a constant load on the sample, a tilt in the weight arm would slightly change the force applied. For each test the goal was therefore to have a horizontal weight arm.

Temperature Effects

A temperature sensor was placed as close as possible to the oedometer cylinder but may not represent the exact temperature of the cylinder. Unfortunately the radial stress measurements for the first and second test seem to follow the changes in temperature in the laboratory. It is not believed that the samples themselves

were affected by the temperature changes as they were not big enough, but the strain gauges definitely can be. This is unfortunate for the interpretation of the data as it gives a false image of what happens to the sample itself. Trends could fortunately be observed and these were used for the interpretation of the data.

LVDT

It is essential that the LVDT is placed in such a way that it stays within its linear range to ensure the accuracy of the measurements of the axial deformation. It is also important that its sleeve is attached properly to the setup so that it will not move during the test.

Noise from Uniaxial Deformation Sensors

The uniaxial deformation sensors were glued to the cylinder and covered with tape so that they would not be too affected by noise from the room. Some noise would still affect the sensors. It is also possible that the stickers are not glued onto the oedometer cylinder well enough. This would give inaccurate measurements and should be checked prior to each experiment.

Differential Pressure

Different pore pressures were set for the three tests due to various reasons. This may have affected the way the samples reacted to the applied stress and fluid exposure. The Validyne Demodulator was coupled out between each differential pressure test to decrease the possibility of affecting other measurements. It can create a magnetic field that may create noise.

Ultrasound

The signal transmitted from the ultrasound setup travels through several couplings on its way to the sample and back. Some energy can get lost on the way.

Sampling Rate

The sampling rate for this experiment was generally set to be every ten seconds. This could affect the interpretation of the data as a lot of potentially important measurements between each registration could be lost.

Time Increments

During this experiment each load step was not carried out for the same length of time. The data collected from each step would vary, and thus the comparison of the data gathered will not be as accurate as it could have been using the same duration for each step.

Wire Connections

All the measurements were connected to the amplifier with thin electrical wires. The wires are fragile and had to be handled with care. A little rupture in a wire or a bad connection could affect the measurements.

Chapter 6

Conclusion

The focus of the research for this thesis was shale as a barrier. A hole must be permanently plugged and abandoned (PP&A) at the end of a its lifetime. Regulations require that the annulus is properly sealed off so that no migration of hydrocarbons to the surface will occur at any time in the future. Norwegian authorities have outlined strict requirements for sealing barriers in PP&As on the Norwegian Continental Shelf (NCS). A minimum of two independent barriers in addition to the surface/environmental barrier must be in place, requiring a full cross-sectional barrier also for the annulus. The operation is both costly and time-consuming. By using the existing technology, it has been estimated that 15 rigs will be needed for approximately 40 years of full time operation to plug and abandon existing wells on the NCS (Straume, 2014). Attention has been drawn towards sections where the annulus is not filled with cement and shale formations have moved towards the casing creating a natural barrier. Several studies have been outlined in recent years and indicates that the time-delayed deformation of the shale is most likely related to consolidation and creep (Williams et al., 2009).

Three triaxial loading tests with different fluids (3.5% NaCl, 20% KCl and fresh water) were successfully executed in order to see how the shale material behaved when axial load was applied. Different fluids were used to see if the material would behave differently when exposed to different fluids. Axial displacement, radial stress, temperature and differential pressure measurements were achieved in order to qualify and quantify the behaviour of the material. An ultrasound setup was connected to the setup to see if existing logging tools can be used in the evaluation

of the natural barriers.

The major findings for this experiment showed that the shale tested creeps when exposed to NaCl, KCl and freshwater. More axial load is required to make the shale creep when exposed to NaCl and KCl than freshwater. The sample exposed to KCl shows a greater density of fractures throughout the sample than the two other samples. The permeability for each sample decreases when exposed to axial load and fluids, although the sample exposed to NaCl had a higher permeability at the end of the test than the two other tests. The ultrasound measurements confirm the results found in the triaxial tests and can be used to see if there is contact between the formation and the casing. The P-wave velocity of the sample exposed to KCl was greater than the samples exposed to NaCl and freshwater. An S-wave was likely found for two of the tests. Some elastic properties can be found through velocity analysis but the difficulty in locating an S-wave complicates the findings.

Future Work

An increasing number of studies are done to qualify and quantify shales that can be used to seal off the annulus. A step in the right direction to understand the process would be to gather an overview of all the shale types on the Norwegian Continental Shelf and discover what would distinguish creeping shales from others.

A greater effort can be put into the CT Scan to see how fractures propagate through the sample when exposed to axial load and fluids. Fracturing is an important parameter and to be able to see how the fractures are connected is of great use. It would be of great interest to see how the fracture density changes during a test and see if correlations could be made to other key measurements.

In order to ascertain whether the triaxial setup is able to provide easy access to creep behaviour, the test procedures and discussed uncertainties must be significantly improved. If new tests are to be done on this setup, it would be beneficial to spend longer time on each test to reach creep state, as well as to carefully monitor and coordinate the duration of each load step applied to the sample. It would also be beneficial to establish initial pore pressure before testing, as it would give a more accurate result compared to *insitu* shales.

Bibliography

Allouche, M., Guillot, D., Hayman, A. J., Butsch, R. J., and Morris, C. W. (2005). *Well Cementing, Chapt. 15 Cement Job Evaluation.*

Atkinson, J. and Bransby, P. (1978). *The Mechanics of Soils, An Introduction to Critical State Soil Mechanics.*

Austbø, L. E. (2016). Laboratory testing to study initiation and evolution of shale barriers.

Ballard, T. J., Beare, S. P., and Lawless, T. A. (1994). Fundamentals of shale stabilization: Water transport through shales. In *SPE Formation Evaluation.*

Bjørlykke, K. (2010). *Petroleum Geoscience.*

Brun-Lie, C. (2016). Shale as a barrier: Literature study and initial laboratory experiments on sele formation.

Chenevert, D. M. (2017). Water activity and shale stability. In *AquaLab.*

Cristescu, N. D. and Hunsche, U. (1998). *Time Effects in Rock Mechanics.*

DeBruijn, G., Elhancha, A., Khalilova, P., Shaposhinkov, P., Tovar, G., and Sheperd, P. (2016). An integrated approach to cement evaluation. *Oilfield Review 28.*

Departement, N. P. (2016). Norsok standards.

Detrounrey, E. and Cheng, A. H.-D. (1993). *Comprehensive Rock Engineering: Principles, Practice and Projects, Chap. 5: Fundamentals of poroelasticity.*

Dracy, H. (1856). *Les fontaines publiques de la ville de Dijon.*

Dusseault, M. (2011a). Coupled pocesses and petroleum geomechanics. *Earth Sciences*.

Dusseault, M. (2011b). Geomechanical challenges in petroleum reservoir exploitation. *Journal of Civil Engineering*.

Eslinger, E. and Pevear, D. R. (1988). *Clay Minerals for Petroleum Geologists and Engineers*.

ExxonMobil (2003). *Marcol Oil 82*.

Fjær, E. (1999). *Static and dynamic moduli of weak sandstones. In Rock Mechanics for Industry. Amadei et al. (eds), p-675-681*.

Fjær, E. (2006). Golden rocks. In *Modeling the stress dependence of elastic wave velocities in soft rocks*.

Fjær, E., Folstad, J., and Li, L. (2016). How creeping shale may form a sealing barrier around a well. In *50th US Rock Mechanics/Geomechanics Symposium*.

Fjær, E., Holt, R. M., Thorsrud, P., Raaen, A. M., and Risnes, R. (2008). *Petroleum Related Rock Mechanics*.

Fjær, E. and Ruistuen, H. (2002). Impact of the intermediate principal stress on the strength of heterogeneous rock. *Journal of Geophysical Research*, 107(B2).

Halliburton (2017). Potassium chlorite (kcl).

Haynes, W. M. (2016). *Handbook of Chemistry and Physics*.

Helffrich, G. R. and Wood, B. J. (2001). The earth's mantle. *Nature*.

Holt, R. M. (2016). Personal communication.

Holt, R. M. (2017). A couple of (old/new) thoughts on shale barriers & fluids. In *Shale as a Barrier*.

Holt, R. M., Sønstebø, E. F., Horsrud, P., and Skaflestad, R. (1996). Fluid effects on acoustic wave propagation in shales. *Eurock*.

Horsrud, P. (2001). Estimating mechanical properties of shale from empirical correlations. *SINTEF*.

Industry, N. P. (2004). *NORSOK Standard D-010*.

IRIS and USGS (2017). Seismic signatures.

Josh, M., Esteban, L., Piane, C. D., Sarout, J., Dewhurst, D., and Clennell, M. (2012). Laboratory characterisation of shale properties. *CSIRO Earth Science and Resource Engineering*.

King, M. (1969). *Rock Mechanics - Theory and Practice, Chapt. 19: Static and Dynamic Elastic Moduli of Rocks under Pressure*.

Kristiansen, T. G. (2015). Why shale could be used as a permanent well barrier element. In *P&A Forum*.

Lashkaripour and Dusseault (1993). *Relationships among principal shale properties*.

LTD, A. N. (2017). Ultrasonic velocity chart.

Lyu, Q., Ranjith, P., Long, X., Kang, Y., and Huang, M. (2015). A review of shale swelling by water absorption. *Elviser*.

Marsden, I., Wu, B., Hudson, I., and Archer, I. (1989). Investigation of peak rock strength behaviour for well bore stability application. *International Society for Rock Mechanics*.

Mavko, G. (2017a). Basic geophysical concepts.

Mavko, G. (2017b). Conceptual overview of rock and fluid factors that impact seismic velocity and impedance.

MX840B, Q. (2017). The 8-channel iniversal amplifier with compact size.

O'Brien, D. E. and Chenevert, M. E. (1973). Stabilizing sensitive shales with inhibited, potassium-based drilling fluids. *Journal of Petroleum Technology*.

Odom, I. E. (1984). Smectite clay minerals: Properties and uses. *The Royal Society*.

of Washington, U. (2017). Thick walled cylinders.

Renaissance, H. S. (2009). Measuring earthquakes.

Sato, H., Fehler, M. C., and Maeda, T. (2012). *Seismic Wave Propagation and Scattering in the Heterogeneous Earth*.

Schlemmer, R., Friedheim, J., Growcock, F., Bloys, J., Headley, J., and Polnaszek, S. (2003). Chemical osmosis, shale, and drilling fluids. In *SPE 86912*.

Sherwood, J. D. and Bailey, L. (1994). Swelling of shale around a cylindrical wellbore. *Proceedings*.

Skjerve, K. (2013). Evaluation of shale formations as barrier element for permanent plug and abandonment of wells. Master's thesis.

STEP and API (1998). *Recommended Practices for Core Analysis*.

Stovas, A. and Hao, Q. (2015). Seismic waves, lecture notes course tpg4125.

Straume, M. (2014). Behov for ny kostnadseffektiv p&a teknologi på norsk sokkel. In *Plug and Abandonnement Forum (PAF), Sintef Seminar*.

Sønstebø, E. F. and Holt, R. M. (2001). Brine exposure effects on a tertiary north sea shale. *SINTEF*.

Tao, Q. and Ghassemi, A. (2006). Optimization of mud properties for drilling in shale using coupled chemoporo-thermoelasticity. In *American Rock Mechanics Association*.

Tiomin, A., Lungershausen, D., and Kravets, P. (2014). Microannulus and cement evaluation: Effectiveness of cement evaluations using sonic and ultrasonic technologies in wells with microannulus between casing and cement sheath. In *SPE Annual Caspian Technical Conference and Exhibition*.

UCL (2017). Clays and minerals.

Weems, J. B. (1903). *Chemistry of Clays*.

Weerakkody, D. Y. and Morgan, D. M. A. (2012). Acoustic impedance.

Williams, S., Carlsen, T., Constable, K., and Guldahl, A. (2009). Identification and qualification of shale annular barriers using wireline logs during plug and abandonment operations. In *SPE/IADC Drilling Conference and Exhibition*.

Xu, H., Zhou, W., Xie, R., Da, L., Xiao, C., Shan, Y., , and Zhang, H. (2016). Characterization of rock mechanical properties using lab tests and numerical interpretation model of well logs. *Mathematical Problems in Engineering Volume 2016*.

Zhao, X. L. and Roegiers, J. C. (1995). Creep crack growth in shale. *The University of Oklahoma*.

Zimmer, M. (2003). *Seismic Velocities in Unconsolidated Sands*. PhD thesis.

Zoback, M. (2007). *Reservoir geomechanics.*

Appendix A

Thermoelasticity

Most materials expand or compact when exposed to temperature changes. The axial thermal strain, ϵ_a, which results form a temperature change is given by:

$$\epsilon_a = -\alpha_T(T - T_0) \tag{1}$$

where α_T is the linear thermal expansion coefficient, T_0 is the initial temperature and T is the new temperature (Fjær et al., 2008). The minus sign ensures that α_T is positive for the cases of expansion, thus for temperature increases.

Borehole instability in deep, low strength shale formations is a problem that may occur, especially when drilling deep wells where the pressure and temperature increases with depth. The instability can be caused by the high compressive effective stress or tensile stress due to pore pressure increase and the stress concentration while drilling (Tao and Ghassemi, 2006). In deeper sections the temperature differences between the formation temperature and the production phase are usually small and the effect is not believed to have significant contribution to shale displacement (Williams et al., 2009). In shallower sections however, thermal response could escalate the displacement process.

Chemical Effects

When a rock is exposed to fluid, a chemical equilibrium between the pore water and the solid material will be established over time. This means that the minerals dissolve and precipitate at the same rate. The presence of a freely moving fluid in a rock therefore modifies its mechanical response (Detrounrey and Cheng, 1993). If the pore fluid is altered, dissolution or deposition of minerals may occur. Several rock components, like salts and some clay and carbonate minerals, are dissolvable in water.

When external fluids which could strongly affect the material properties are exposed to formations, deterioration of the cement of the rock is one possible outcome. This will typically reduce the rock strength by 30-100% (Fjær et al., 2008). The effect on clay minerals may result in a complete change in framework moduli (change in shear and bulk modulus) as they soften or dissolve in water. The acidity (pH-value) of the water might also affect the solubility of minerals in pore water. Therefore,

if the changes are given enough time to react, it is expected that the strength of certain rocks may be sensitive to parameter changes. These effects might initiate or alter a displacement process in a given formation.

An example of alteration in fluid is when a formation is exposed to drilling fluids. To stabilize an open hole during drilling, a drilling fluid with properties that restrict displacement in the formations is often used. This process has been proven to be difficult to reverse, meaning the chemical effect to encourage advantageous displacement after drilling will often not be possible after such a treatment. However it is not yet known if time may be an important factor in this regard. It is yet to be fully understood if an equilibrium between the surrounding, natural conditions will happen over time and thus reverse the induced material response.

Williams et al., 2009, (Williams et al., 2009) suggest that chemical effects is not a major contributor to the displacement processes after drilling. This is based on the observation that log responses show that bonding appears regardless of the type of drilling fluid that is used.

Failure Mechanisms

Shear, tensile and compaction failures (Figure 1) are failure mechanisms that imply that a rock can change its shape permanently if sufficiently large stresses are applied to it. In petroleum related rock mechanics, rock failure is often the reason for problems such as unstable boreholes and solid production (Marsden et al., 1989).

The stresses causing failure are applied to the framework of the rock. Rock strength is defined as the stress level a framework typically can endure before it fails and sometimes breaks apart (Fjær and Ruistuen, 2002). The effective stresses are a combination of the external stresses and the fluid inside the framework. The orientation of the failure usually depends on the weakest plane of the rock.

Failure mechanics are seen in many different wellbores, mostly in shale sequences that require a higher mud weight than the pore pressure to remain stable (Williams et al., 2009).

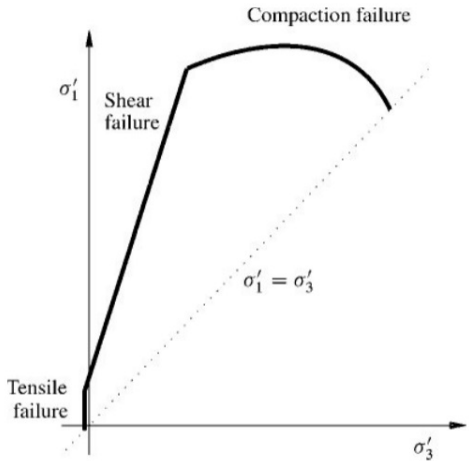

Figure 1: Location of the different failure mechanics (Modified from (Fjær et al., 2008))

Shear Failure

Shear failure is the most common mode of failure. It is caused by extreme shear stress and initiates when the shear stress along a plane in the rock is high enough to create a fault zone along the failure plane. The two sides of the failure plane will move relative to each other, creating a frictional process (Fjær et al., 2008).

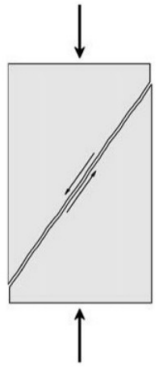

Figure 2: Shear failure (Modified from Fjær et al. (2008))

Since the frictional force acting against the relative movement of the two bodies is dependent on the force that pushes them together, it is assumed that the critical

shear stress τ_{max} for which the failure occurs, depends on the normal effective stress σ' acting on the failure plane (Fjær et al., 2008):

$$|\tau_{max}| = f(\sigma') \tag{2}$$

This assumption is called Mohr's hypothesis, and defines that the pure shear failure only depends on the maximum ($\sigma_H = \sigma_1$) and minimum ($\sigma_h = \sigma_3$) principal stresses.

Specific parameters of the function $f(\sigma')$ can be chosen to obtain different criteria for shear failure. The Tresca criterion is known as the simplest one, stating that the material will yield when a critical level of shear stress is reached:

$$\tau_{max} = \frac{1}{2}(\sigma'_1 - \sigma'_3) = S_0 \tag{3}$$

where S_0 is the inherent shear strength, also known as cohesion, of the material (Zoback, 2007). A more popular criterion is the Mohr-Coloumb criterion, which assumes that $f(\sigma')$ is a linear function of σ':

$$|\tau| = S_0 + \mu\sigma' \tag{4}$$

where μ is the internal friction coefficient. By simplifying the equation using assumptions and approximations, Mohr-Coulomb can be written in terms of the minimum and maximum principle stresses:

$$\sigma'_1 = C_0 + \sigma'_3 tan^2\beta \tag{5}$$

where $C_0 = 2S_0 tan\beta$ is the uniaxial compressive strength (UCS) and $\beta = \frac{\pi}{4} + \frac{\phi}{2}$ is failure angle, with ϕ as the friction angle (Fjær et al., 2008).

Tensile Failure

Tensile failure is also a very common failure mode, although not in the depth of the earth (Zoback, 2007). It occurs when the effective tensile stress across a plane in the rock goes above the critical limit known as tensile strength, T_0. T_0 has the same units as stress and is a characteristic property of the rock material (Fjær et al., 2008).

The tensile strength is very sensitive to preexisting cracks in the material that are oriented more or less perpendicular to the tensile stress. Most sedimentary rocks

have a relatively low tensile strength, generally just a few MPa or less. The failure criterion identifies the location of the failure surface in principal stress space and specifies the stress condition for when tensile failure will occur (Fjær et al., 2008):

$$\sigma' = -T_0 \tag{6}$$

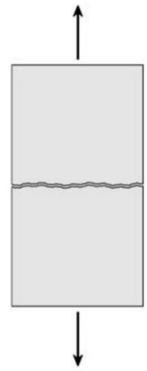

Figure 3: Tensile failure (Modified from Fjær et al. (2008))

Compaction Failure

Compaction is a failure mode that generally occurs in highly porous media, as it is the result of pore collapse (Fjær et al., 2008). The pore collapse is usually caused by an important hydrostatic stress that is applied to the grain skeleton of the rock. Compaction often results in a closer packing of the material (Figure 4), as grains loosen and break as they are pushed and twisted into the open pore space (Williams et al., 2009).

Although pore collapse may occur under pure hydrostatic loading, failure happens due to local excessive shear forces acting through the grains and their contacts (Fjær et al., 2008). Grain crushing may also happen under hydrostatic loading, resulting in fractured grains. The damage either way will be permanent, and the compaction leads to a denser packing of the structure. The load carrying capacity of the rock may increase due to the denser packing. This is not the case after shear or tensile failure (Zoback, 2007).

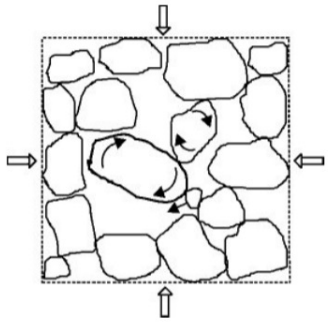

Figure 4: Reorientation of grains as a result of compaction (Modified from Fjær et al. (2008))

Consolidation

Consolidation is a result of a change in stress state of a rock that induces pore pressure changes. It takes time to re-establish pore pressure equilibrium after a pressure alteration, as it involves the flow of pore pressure through a porous medium. Darcy's Law describes viscous flow in a porous rock (Dracy, 1856):

$$\vec{Q} = -A\frac{k}{\eta_f}\Delta p_f \tag{7}$$

where $\vec{Q}$ is the fluid flow rate, Δp_f is the pore pressure gradient, k is the permeability of the rock and η_f is the dynamic viscosity of the fluid. A is the surface the fluid flows through.

Darcy's law can be combined with the strain parameter ζ and others. By making several assumptions, in this case that $K_{fr}, G_{fr} \ll K_s$, one can find an expression for the diffusion constant C_D. This is a measure of how far a pore pressure disturbance can propagate during a given time (Fjær et al., 2008):

$$C_D \approx \frac{kK_f}{\eta_f \phi}[1 + \frac{K_f}{\phi(K_{fr} + \frac{4}{3}G_{fr})}] \tag{8}$$

where K_{fr} and G_{fr} are the drained bulk modulus and the shear modulus of the frame, respectively and K_f is the bulk modulus of the fluid.

The diffusion constant C_D is physically a measure of how far a pore pressure disturbance can propagate during a certain amount of time. It is important to note that the characteristics of the fluid flow also depends on the elastic properties of the rock, not only the fluid parameters.

The behavior of consolidation described above does not take inelasticity of the rock framework into account. This means its behavior is reversible (Fjær et al., 2008), which generally is not the case.

Thermal consolidation will occur in shales that contain large amounts of hydrated clays when they are exposed to high temperatures. The kinetic thermal energy overcomes the weak absorbed water bonding, resulting in a shrinkage (Dusseault, 2011b) in the vertical direction. This means a compensation has to be made in the horizontal direction, which results in an expansion.

Geological History

Figure 5: The three main segments on the Norwegian Continental Shelf (modified from (Departement, 2016))

The core material was extracted from a field on the Norwegian Continental Shelf. The area is known to be a good producer of hydrocarbons and a lot of research has been done on the geological environment. Since this shale is confidential, only a general geological description will be given for the whole area.

The Norwegian Continental Shelf consists of three main segments (Bjørlykke, 2010):

- The North Sea
- The Norwegian Sea
- The Barents Sea

These segments were part of a large epicontinental sea lying between the continental masses of Fennoscandia, Svalbard and Greenland. Later, the continental break-up and onset of seafloor spreading would divide them (Bjørlykke, 2010). The segments therefore have many stratigraphic similarities as well as geological evolution but there are also important differences, in particular during Cretaceous-Cenozoic period.

When complete separating of the continent took place in early Cenozoic, a series of post Caledonian rift episodes developed sedimentary basins at the connected continental margins of Norway and Greenland, as well as in the adjacent shallow seas, the North Sea and the western Barents Sea (Bjørlykke, 2010). The Norwegian Margin consists of a deep offshore rifted volcanic margin that travels along the Norwegian coast line and along the western Barents Sea and Svalbard to the north. The Norwegian margin consists of a continental shelf and slope that vary considerably in width and morphology (Bjørlykke, 2010).

Lithostratigraphic charts of the Norwegian Continental Shelf reveal the important amount of marine to deep marine deposits in the areas (Figure 6). These deposits could potentially be of interest to the topic of sealing shale.

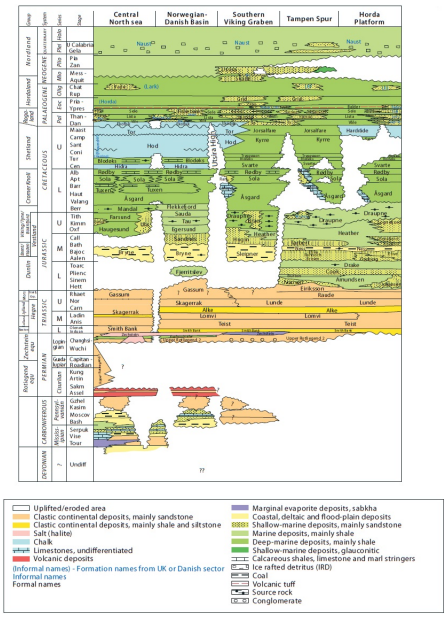

Figure 6: Lithostratigraphic chart of the Norwegian North Sea (modified from (Departement, 2016))

Appendix B

Calibration of Uniaxial Deformation Sensors

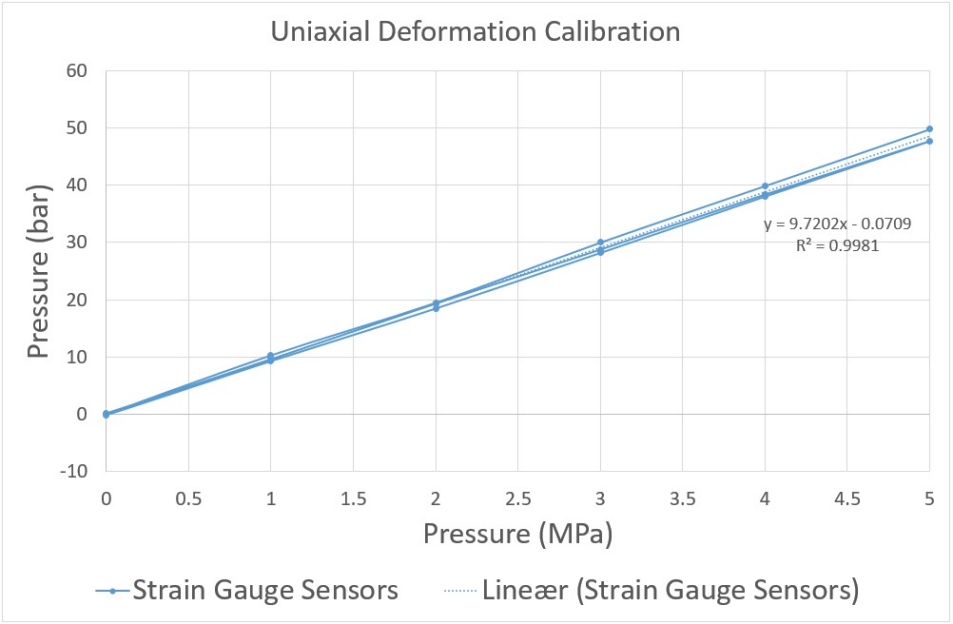

Figure 7: Hysteresis of calibration of strain gauges

MPa	Sensor 1 (bar)	Sensor 2 (bar)
5	49.78	50.08
4	39.88	39.84
3	30.00	30.15
2	19.50	19.84
1	10.32	10.54
0	-0.057	-0.075
1	9.32	10.85
2	18.50	21.58
3	28.21	32.52
4	38.05	42.95
5	47.73	53.50
4	38.42	42.79
3	28.80	31.99
2	19.36	21.49
1	9.65	10.71
0	0.21	0.12

Table 1: Values from the uniaxial deformation calibration.

Calibration of Linear Variable Differential Transformer (LVDT)

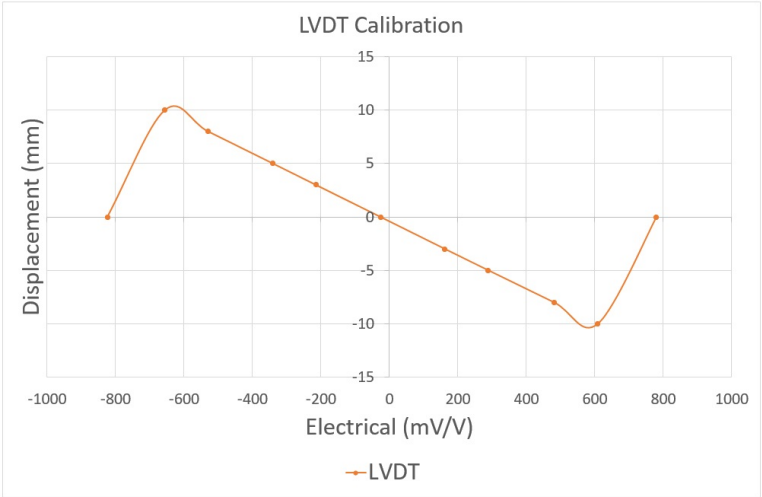

Figure 8: Hysteresis of LVDT calibration

	mV/V	mm
P1	-823,7	12,7
P2	-655,8	10
P3	-529,3	8
P4	-340,1	5
P5	-214,9	3
P6	-26,28	0
P7	162,2	-3
P8	288,8	-5
P9	480,7	-8
P10	608,7	-10
P11	779,8	-12,7
P12	779,8	-12,7
P13	608,8	-10
P14	480,8	-8
P15	288,9	-5
P16	162,3	-3
P17	-25,95	0
P18	-214,6	3
P19	-340,0	5
P20	-529,0	8
P21	-655,7	10
P22	-823,6	12,7

Table 2: Values from the LVDT calibration.

Correction of Sintered Disks

	Travel Time (μs)		
	Maximum	Minimum	Zero Crossing
P-wave 500kHz	1.405	1.138	1.306
S-wave 250kHz	3.213	1.744	2.161
S-wave 125kHz	2.096	2.246	1.993
S-wave 75kHz	1.535	1.992	2.492

Table 3: Travel time of the sintered disks for P- and S-waves of each frequency

Calibration of Load Cell

mV/V	Total Load (kg)	Total Load (kN)
-0.01472	0.0	0.0
-0.04956	25.84	0.25323
-0.08468	51.73	0.50695
-0.11978	77.49	0.75940
-0.15359	103.19	1.01244
-0.18529	129.01	1.26430
-0.15214	103.19	1.01244
-0.11675	77.49	0.75940
-0.08254	51.73	0.50695
-0.04795	25.84	0.25323
-0.01417	0.0	0.0

Table 4: Values from the calibration of the load cell.

Correction of Ultrasound Setup

	Correction (μs) Wave Pick				
	Test 1		Test 2 and 3		
	Maximum	Minimum	Maximum	Minimum	Zero Crossing
Horizontal P-wave 1MHz	5.16	5.72	5,72	5,16	-
Horizontal P-wave 500kHz	5.36	6.06	6,06	5,36	-
Vertical P-wave 500kHz	6.96	8-09	15,83	14,68	-
Vertical S-wave 250kHz	-	-	36,20	34,17	-
Vertical S-wave 125kHz	-	-	37,23	34,71	-
Vertical S-wave 75kHz	-	-	37,28	34,97	36,34

Table 5: Corrections for the ultrasound responses for test 2 and 3

Correction of Bench Top Ultrasonic Setup

	P-wave Velocity (m/s)	Diameter (mm)	Correction (μs)
Peek	2562.5	38.05	-1.10861

Table 6: Correction found from the Peek reference.

Risk Assessment

Hazards	What may happen	Likelihood	Consequences	Initiatives
Pressurized air	Hoses may loosen from the mountain point to the pump	Low	Low	Check all mounting points and hoses; make sure the pump receives steady flow
Weights	Drop on feet	Low	Low	Use protective footwear; concentrate on task
Fluid pressures	Leakage; corrosion damage	Medium-high	Medium	Constant cumulative volume; check the system, lubricate O-rings, screws thoroughly; wear protective goggles
People	Disturbance during the experiment	Low	Medium	Put up sign that experiment is ongoing

Appendix C

CT Scan

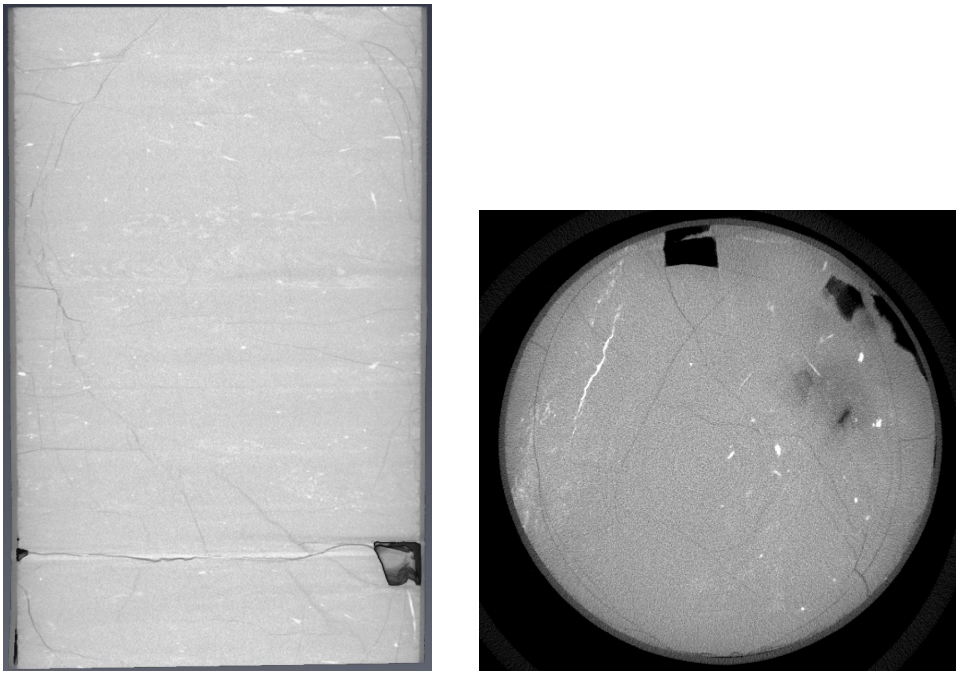

(a) One vertical and one horizontal cross section of sample 1 after testing.

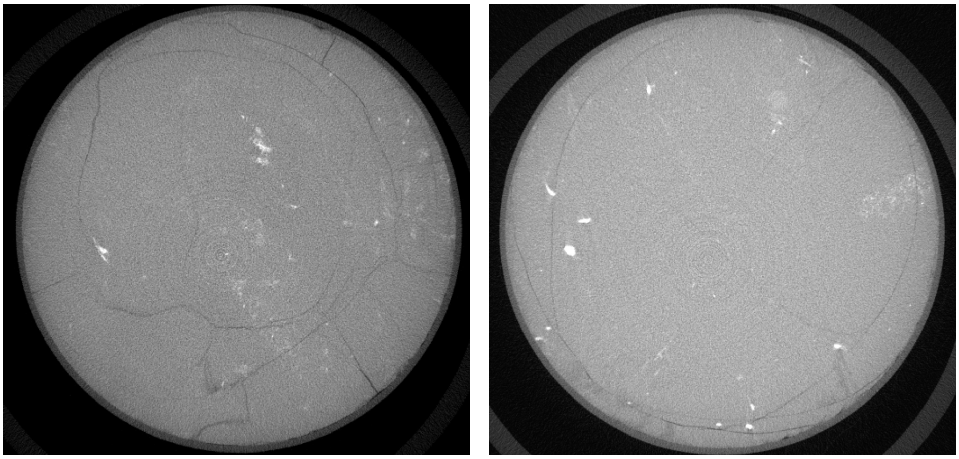

(b) Two horizontal cross section of sample 1 after testing.

Figure 9: Cross sections from different locations of sample 1 after testing.

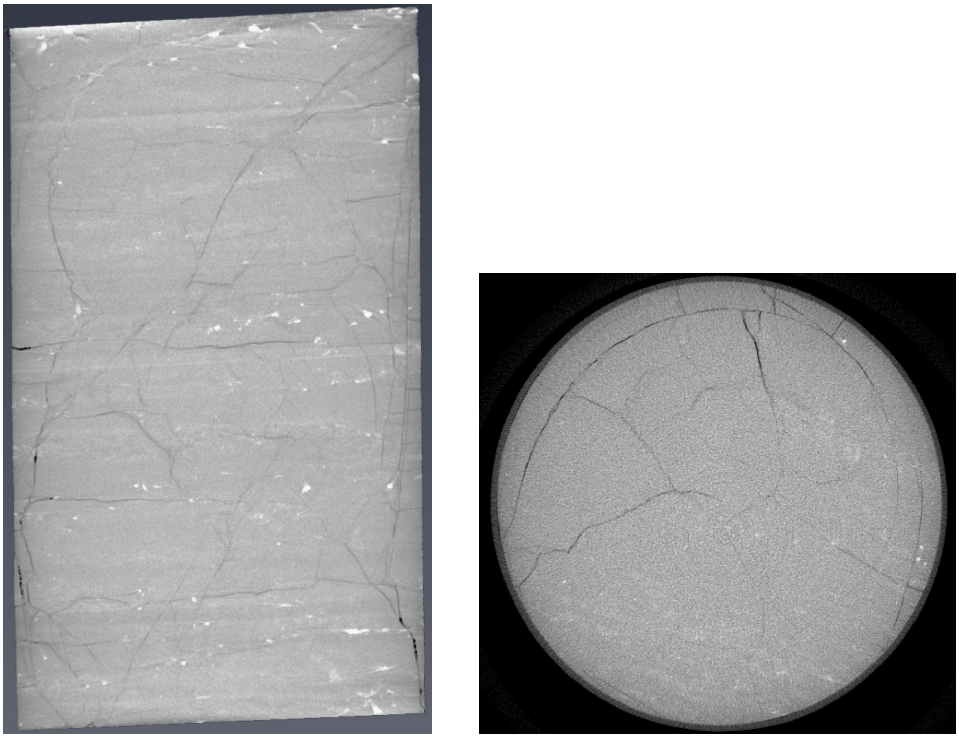

(a) One vertical and one horizontal cross sections of sample 2 after testing.

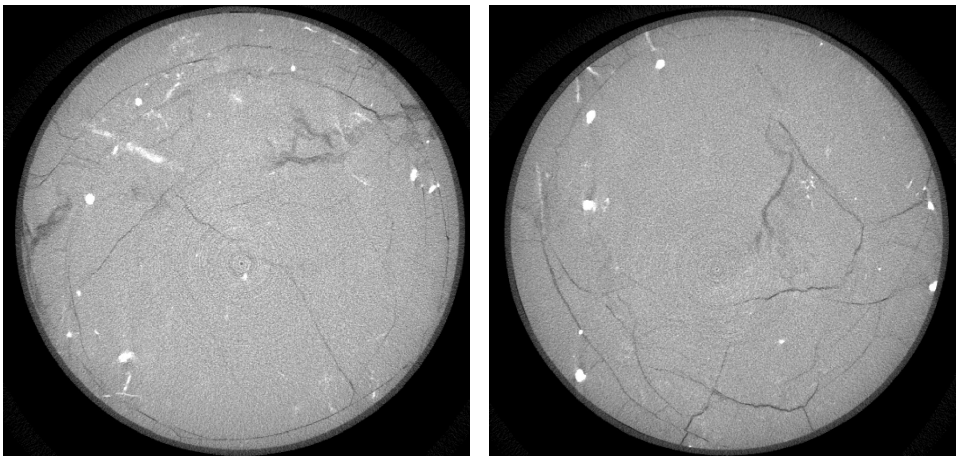

(b) Two horizontal cross sections of sample 2 after testing.

Figure 10: Cross sections from different locations of the second sample after testing.

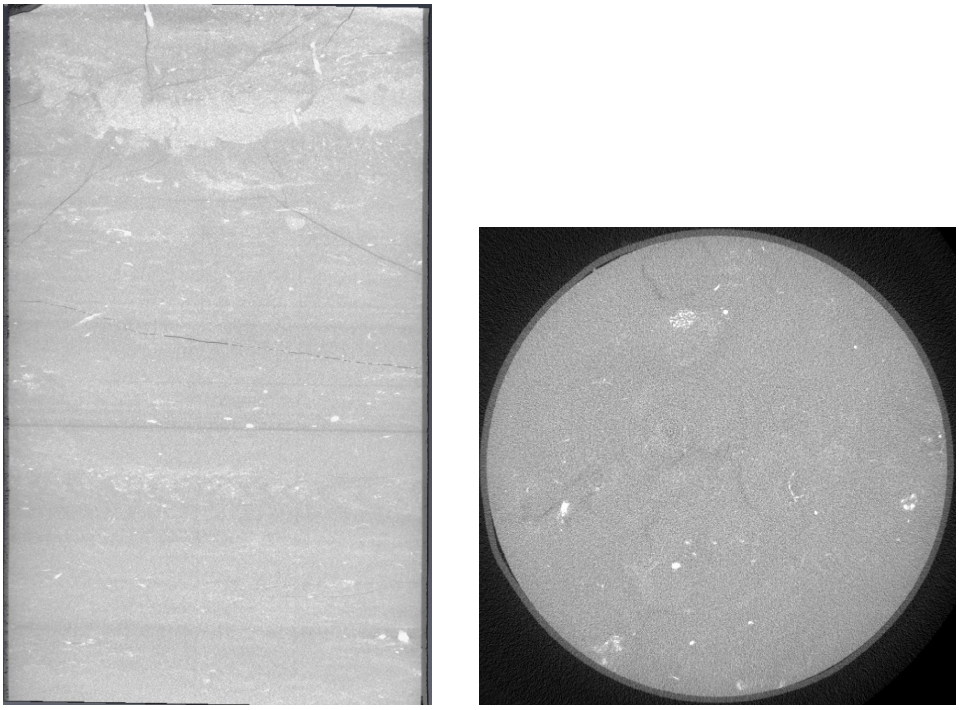

(a) One vertical and one horizontal cross sections of sample 3 before testing.

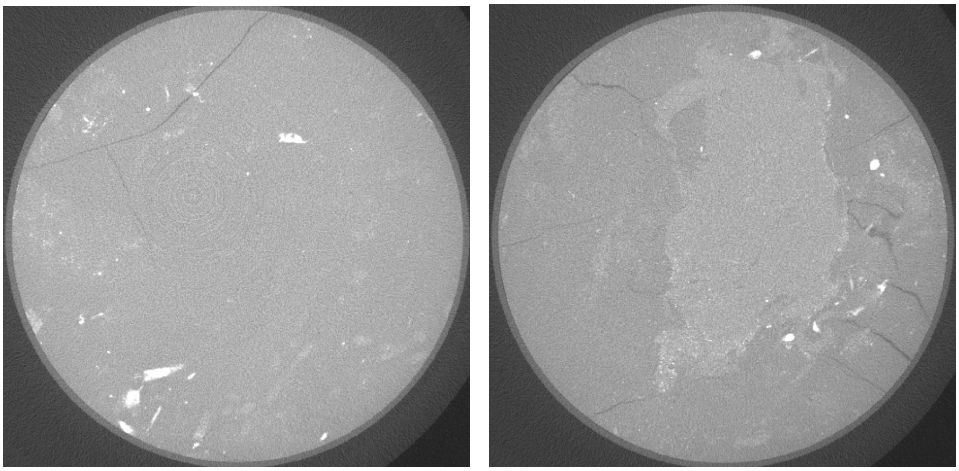

(b) Two horizontal cross sections of sample 3 before testing.

Figure 11: Cross sections from different locations of the third sample before testing.

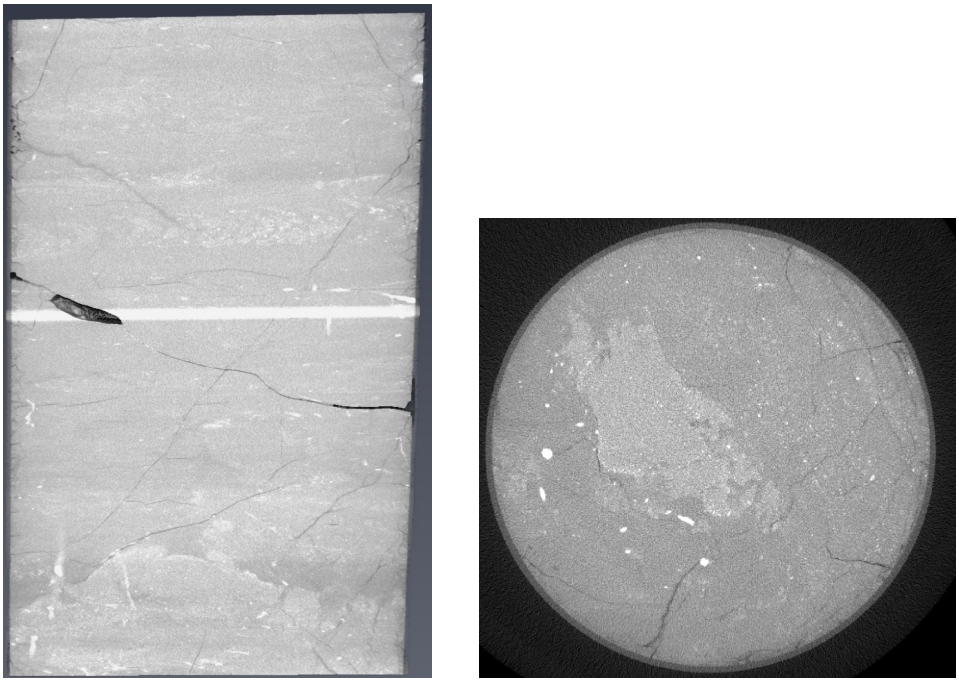

(a) One vertical and one horizontal cross sections of sample 3 after testing.

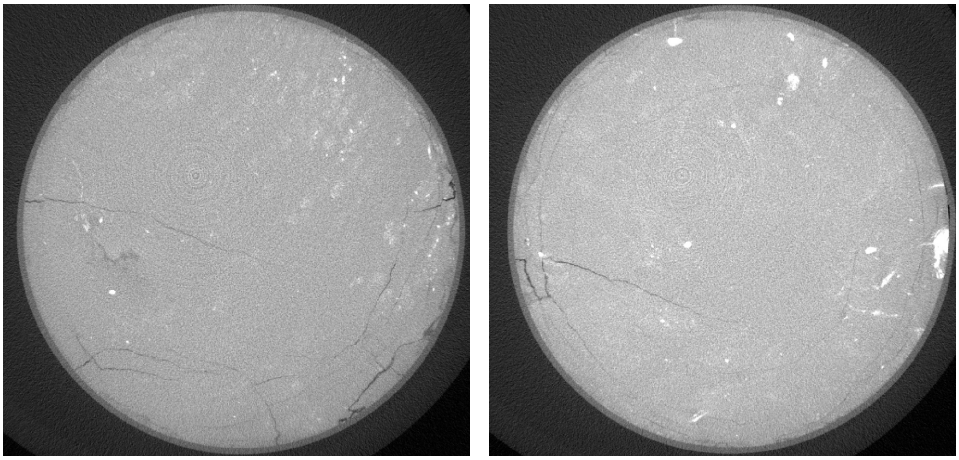

(b) Two horizontal cross sections of sample 3 after testing.

Figure 12: Cross sections from different locations of the third sample after testing.

Deformation Rate

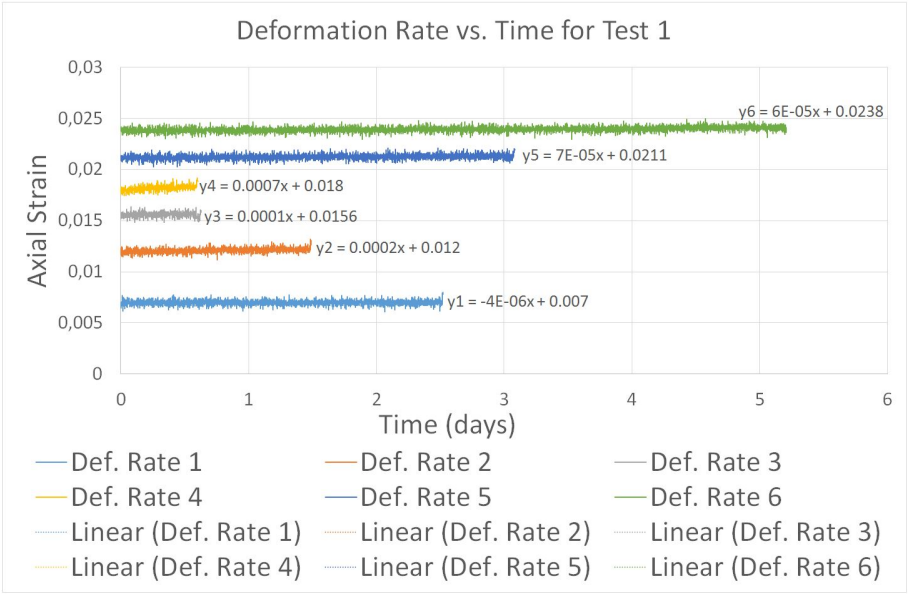

Figure 13: Deformation rate during the first test.

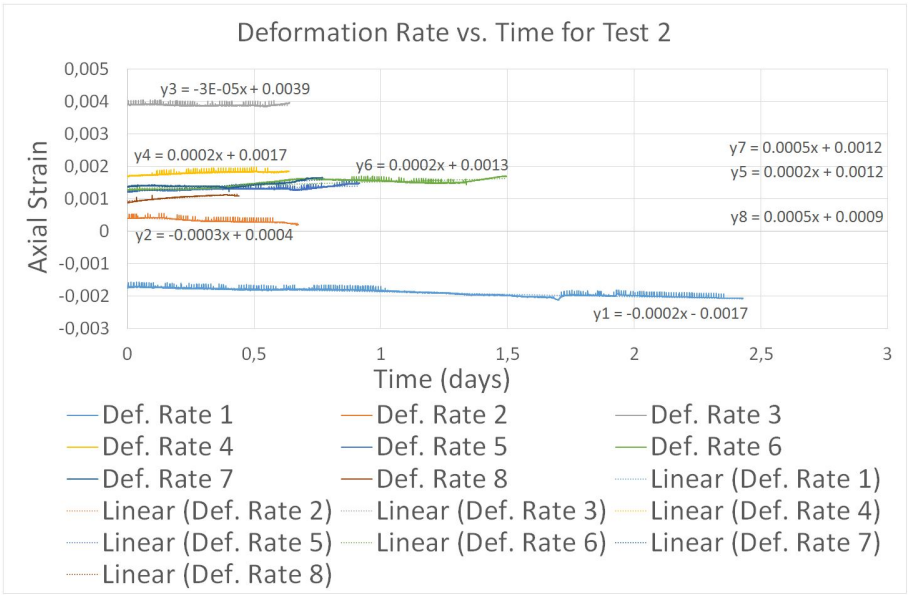

Figure 14: Deformation rate during the second test.

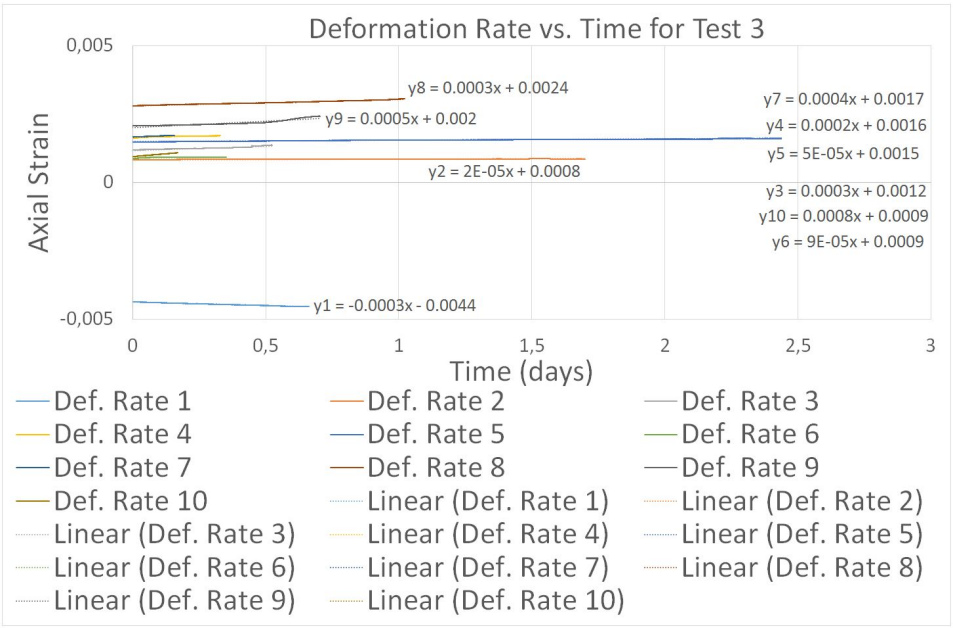

Figure 15: Deformation rate during the third test.

Test 1		Test 2		Test 3	
Axial Stress (MPa)	Deformation Rate (mStrain/day)	Axial Stress (MPa)	Deformation Rate (mStrain/day)	Axial Stress (MPa)	Deformation Rate (mStrain/day)
3.2		4.8	-0.0002	4.9	-0.0003
5.5	-0.000004	7.1	-0.0003	7.1	2.00E-05
7.8	0.0002	11.6	0.00003	9.4	0.0003
10.0	0.0001	13.9	0.0002	11.6	0.0002
12.3	0.0007	16.1	0.0002	13.9	5.00E-05
14.6	0.00007	18.4	0.0002	16.1	9.00E-05
16.7	0.00006	20.6	0.0005	18.4	0.0004
		22.9	0.0005	20.7	0.0003
				22.9	0.0005
				25.2	0.0008

Table 7: Deformation rate for the different tests compared to the axial stress.

Permeability Measurements

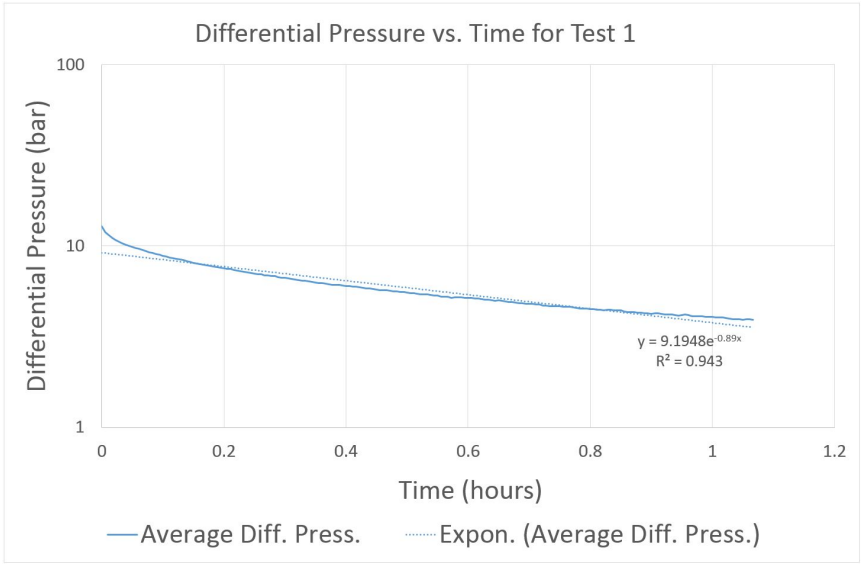

Figure 16: The average differential pressure for the first test with an exponential trend line to find alpha.

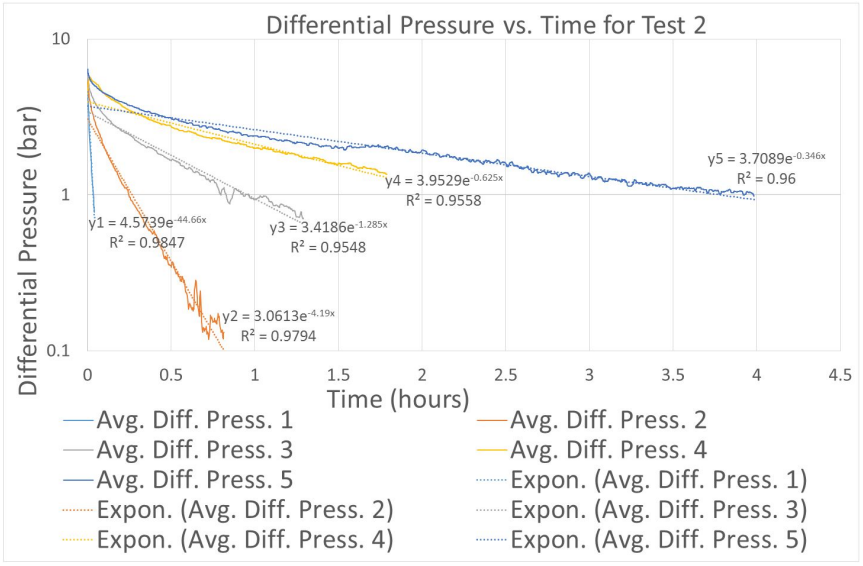

Figure 17: The average differential pressure for the second test with an exponential trend line find alpha.

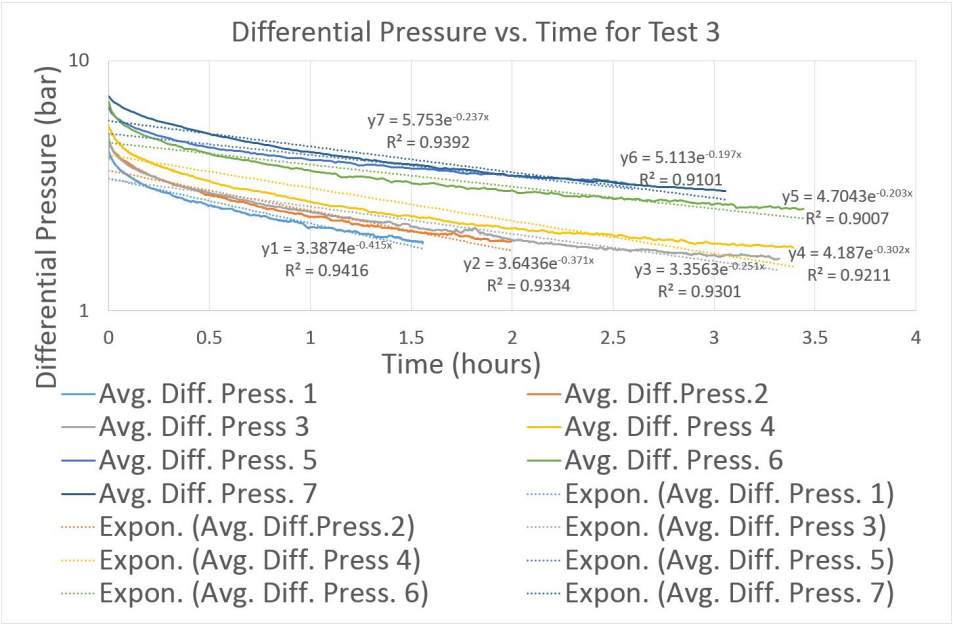

Figure 18: The average differential pressure for the third test performed with an exponential trend line to find alpha.

	Perm. Test 1
Thickness (mm)	66.4
Diameter (mm)	37.8
Mass (gram)	179.86
Bulk Density (gram/cm^3)	2.414
Area (m^2)	$11.34 \cdot 10^{-4}$
Temperature (C)	24.8
Pore Pressure (MPa)	2
Dynamic Viscosity (Pa $\cdot$ s)	0.00106
K_m (pa/m^3)	$4.16 \cdot 10^{12}$
Alpha (1/s)	0.89
Permeability (m^2)	$6.709 \cdot 10^{-15}$
Permeability (mD)	6.8

Table 8: Test 1: The values used to calculate the permeability from the differential pressure test and its result

	Perm. Test 1	Perm. Test 2	Perm. Test 3	Perm. Test 4	Perm. Test 5
Thickness (mm)	67.1	66.95	66.81	66.66	66.54
Diameter (mm)	37.8	37.8	37.8	37.8	37.8
Mass (gram)	177.63	177.63	177.63	177.63	177.63
Bulk Density (gram/cm^3)	2.359	2.364	2.369	2.375	2.379
Area (m^2)	$11.34 \cdot 10^{-4}$	$11.34 \cdot 10^{-4}$	$11.34 \cdot 10^{-4}$	$11.34 \cdot 10^{-4}$	$11.34 \cdot 10^{-4}$
Temperature (C)	25.2	25.8	25.8	27.8	26.4
Pore Pressure (MPa)	2	2	2	2	2
Dynamic Viscosity (Pa·s)	0.001012	0.001012	0.001012	0.001012	0.001012
K_m (pa/m^3)	$4.16 \cdot 10^{12}$	$4.16 \cdot 10^{12}$	$4.16 \cdot 10^{12}$	$4.16 \cdot 10^{12}$	$4.16 \cdot 10^{12}$
Alpha (1/s)	44.66	4.19	1.285	0.625	0.346
Permeability (m^2)	$3.248 \cdot 10^{-13}$	$3.040 \cdot 10^{-14}$	$9.305 \cdot 10^{-15}$	$4.515 \cdot 10^{-15}$	$2.495 \cdot 10^{-15}$
Permeability (mD)	329.1	30.8	9.4	4.6	2.5

Table 9: Test 2: The values used to calculate the permeability from each differential pressure test during test 2 and its results

	Perm. Test 1	Perm. Test 2	Perm. Test 3	Perm. Test 4	Perm. Test 5	Perm. Test 6	Perm. Test 7
Thickness (mm)	67.56	67.55	67.46	67.34	67.23	67.17	66.69
Diameter (mm)	37.8	37.8	37.8	37.8	37.8	37.8	37.8
Mass (gram)	178.16	178.16	178.16	178.16	178.16	178.16	178.16
Bulk Density (gram/cm^3)	2.359	2.364	2.369	2.375	2.379		
Area (mm^2)	11.34 $\cdot 10^{-4}$	11.34 $\cdot 10^{-4}$	11.34 $\cdot 10^{-4}$.	11.34 $\cdot 10^{-4}$	11.34 $\cdot 10^{-4}$	11.34 $\cdot 10^{-4}$	11.34 $\cdot 10^{-4}$
Temperature (C)	24.7	24.4	23.9	24.4	24.0	24.6	23.4
Pore Pressure (MPa)	2	2	2	2	2	2	2
Dynamic Viscosity (Pa·s)	10.02 $\cdot 10^{-4}$	10.02 $\cdot 10^{-4}$	10.02 $\cdot 10^{-4}$	10.02 $\cdot 10^{-4}$	10.02 $\cdot 10^{-4}$	10.02 $\cdot 10^{-4}$	10.02 $\cdot 10^{-4}$
K_m (pa/m^3)	4.16 $\cdot 10^{12}$	4.16 $\cdot 10^{12}$	4.16 $\cdot 10^{12}$	4.16 $\cdot 10^{12}$	4.16 $\cdot 10^{12}$	4.16 $\cdot 10^{12}$	4.16 $\cdot 10^{12}$
Alpha (1/s)	0.415	0.371	0.251	0.302	0.203	0.197	0.237
Permeability (m^2)	3.01 $\cdot 10^{-15}$	2.69 $\cdot 10^{-15}$	1.82 $\cdot 10^{-15}$	2.18 $\cdot 10^{-15}$	1.47 $\cdot 10^{-15}$	1.42 $\cdot 10^{-15}$	1.70 $\cdot 10^{-15}$
Permeability (mD)	3.1	2.7	1.8	2.2	1.5	1.4	1.7

Table 10: Test 3: The values used to calculate the permeability from each differential pressure test during test 3 and its results

Horizontal P-wave Test 1

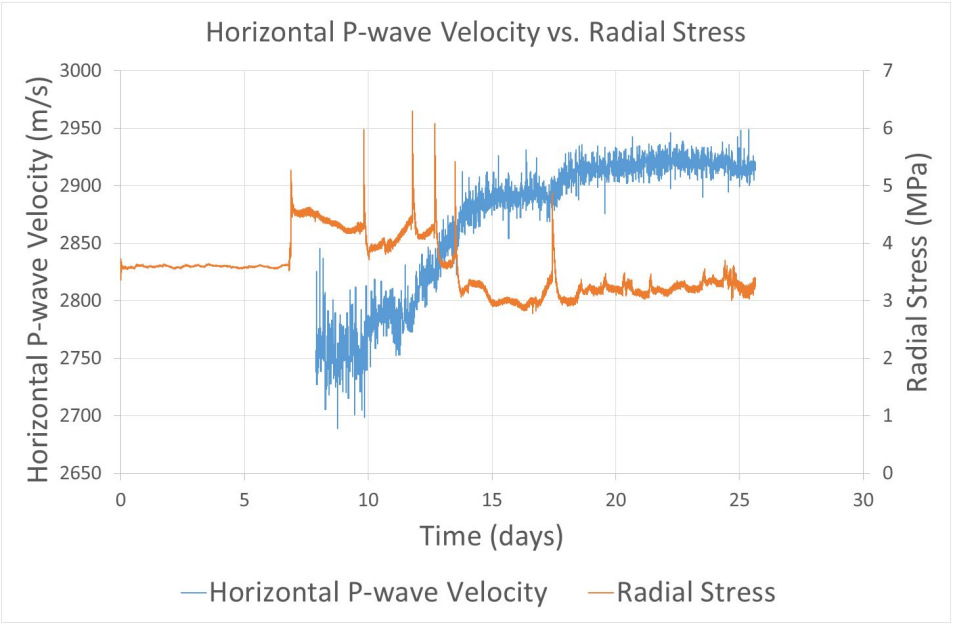

Figure 19: The horizontal P-wave velocity against radial stress for the first test.

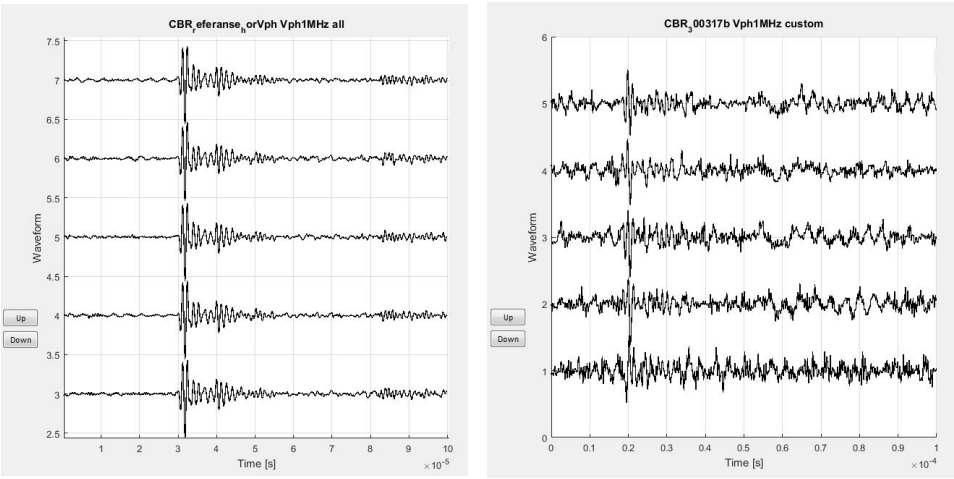

(a) (b)

Figure 20: (a) Reference waveforms of the horizontal P-wave and (b) a selection of waveforms of the horizontal P-wave of the first test.

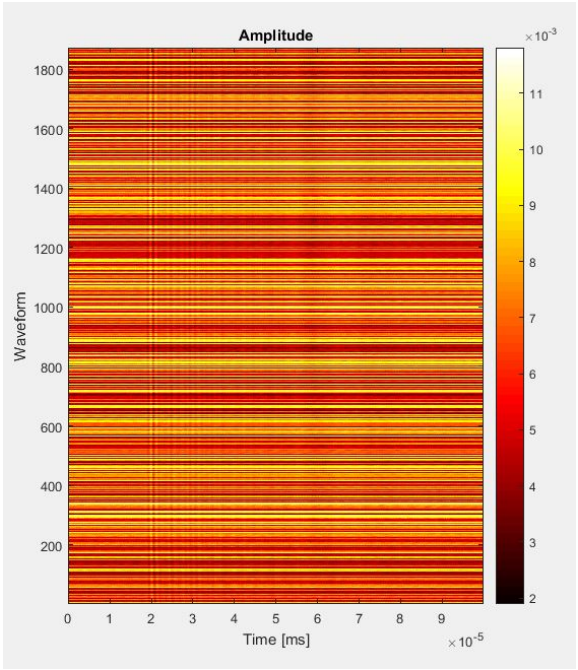

Figure 21: The amplitude of the waveforms of the horizontal P-wave signal of parts of the first test.

Horizontal P-wave Test 2

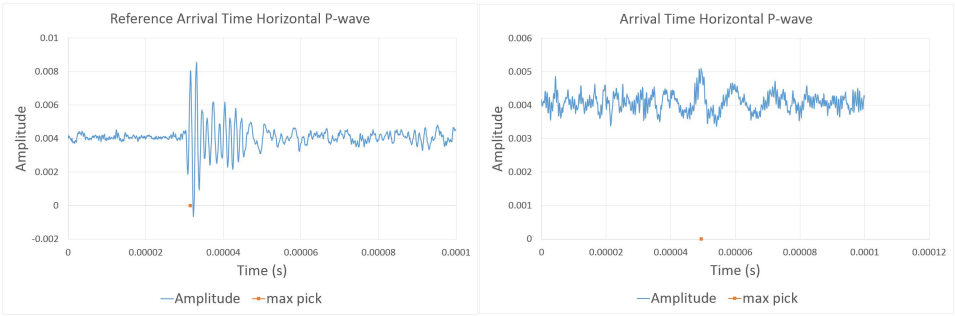

(a) (b)

Figure 22: (a) Reference wave pick of the 500kHz horizontal P-wave and (b) wave pick of the 500kHz horizontal P-wave from the test

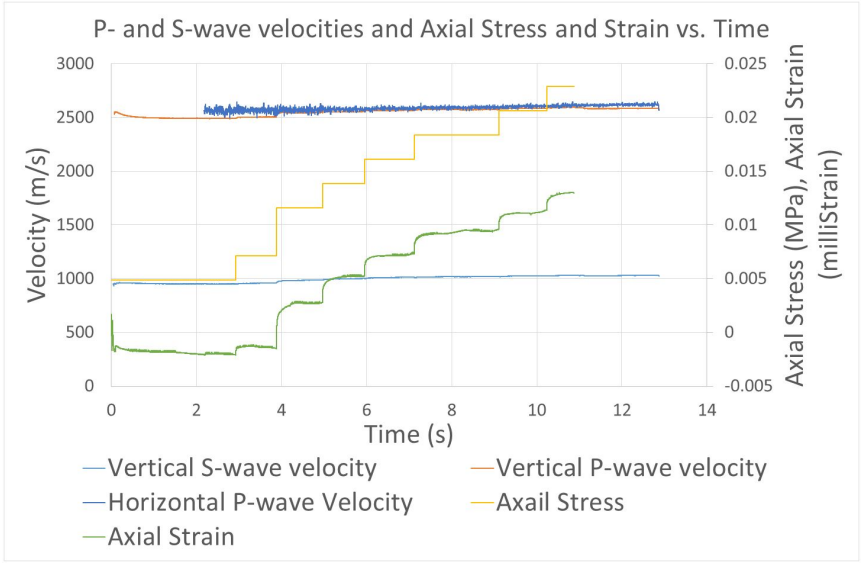

Figure 23: P- and S-wave velocities for each step using the axial deformation measurements for comparison TEST 2

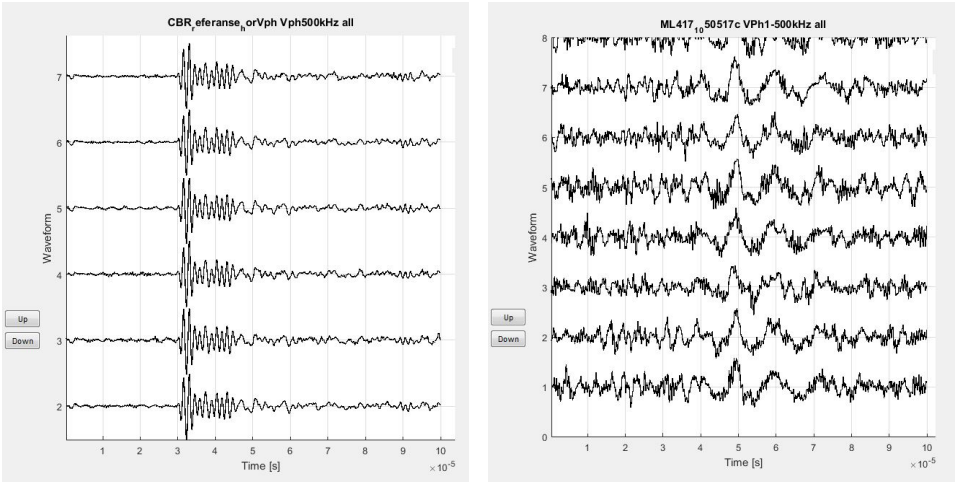

(a) (b)

Figure 24: (a) and (b) shows the difference in waveform signature from the reference and the 500kHz horizontal P-wave from the test

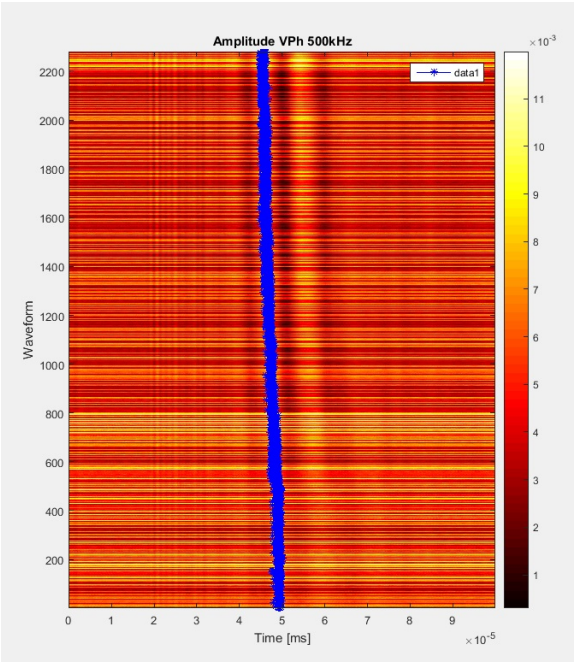

Figure 25: The amplitude of the waveforms of the last half of the test

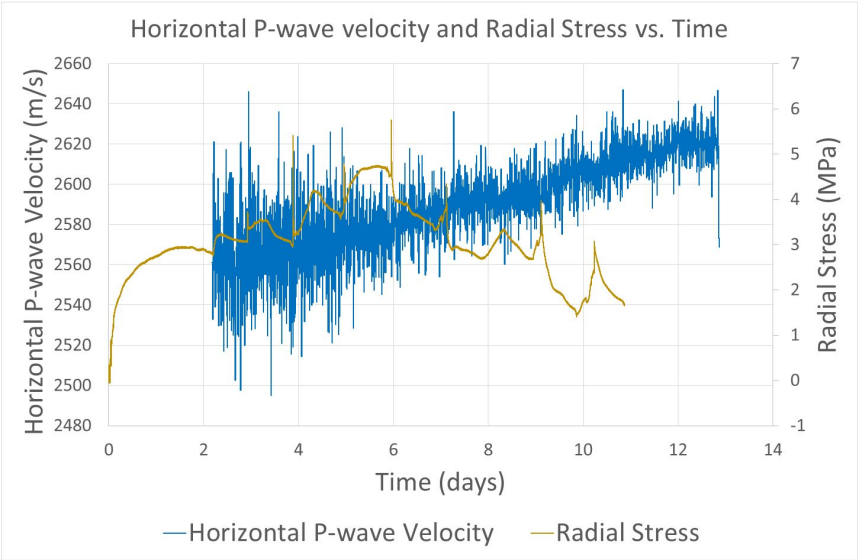

Figure 26: The horizontal P-wave velocity using the axial deformation measurements as reference

Horizontal P-wave Test 3

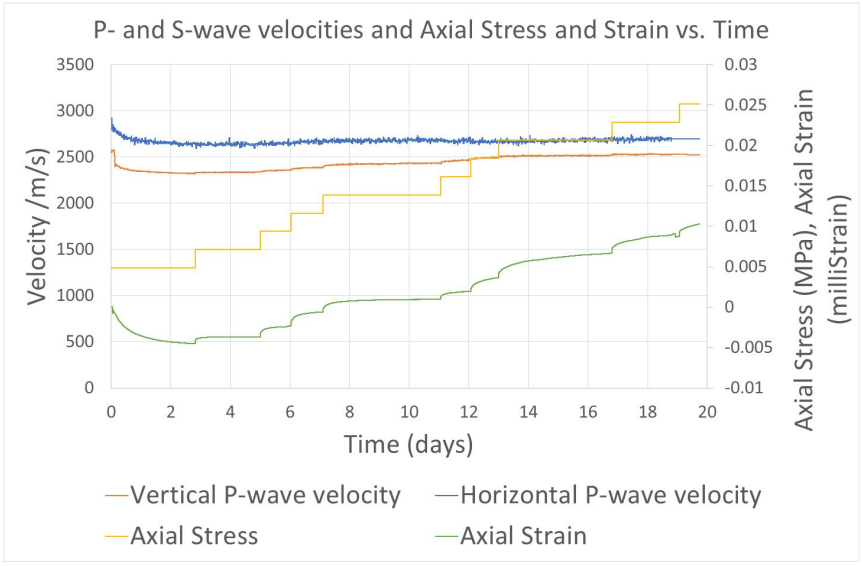

Figure 27: P- and S-wave velocities for each step using the axial deformation measurements for comparison

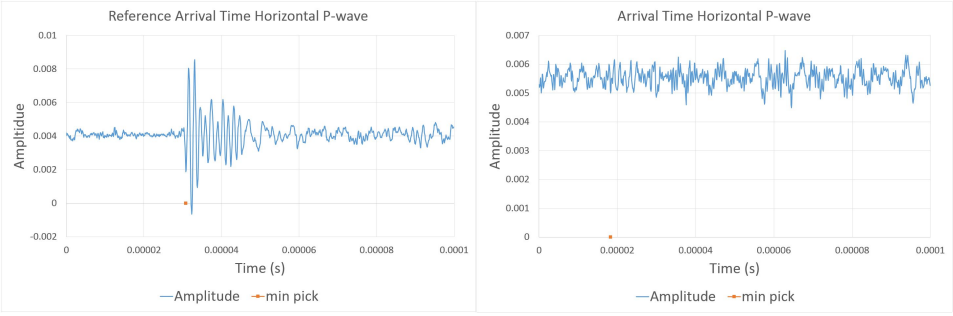

(a) (b)

Figure 28: (a) Reference wave pick of the 500kHz horizontal P-wave and (b) wave pick of the 500kHz horizontal P-wave from the third test

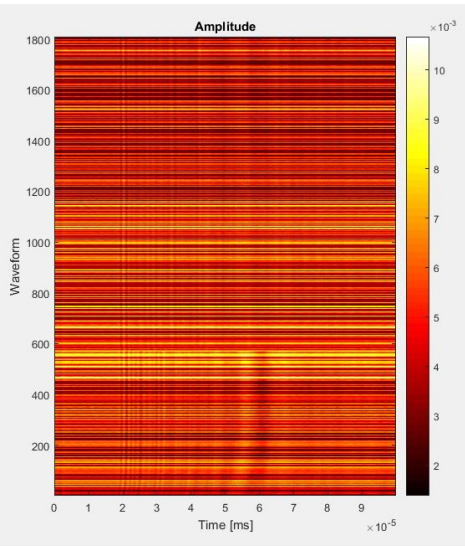

(a) Amplitude

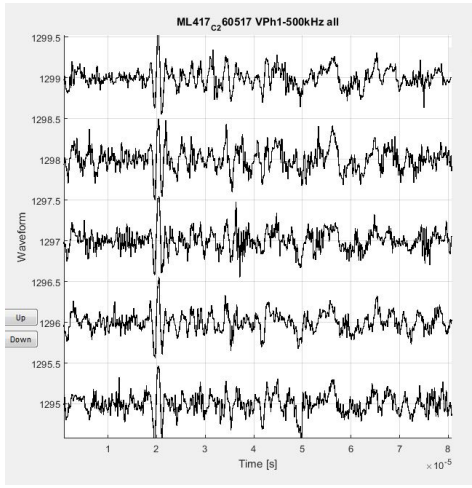

(b) Waveforms

Figure 29: (a) amplitude of the waveforms; (b) waveform showing the bad signal to noise ratio

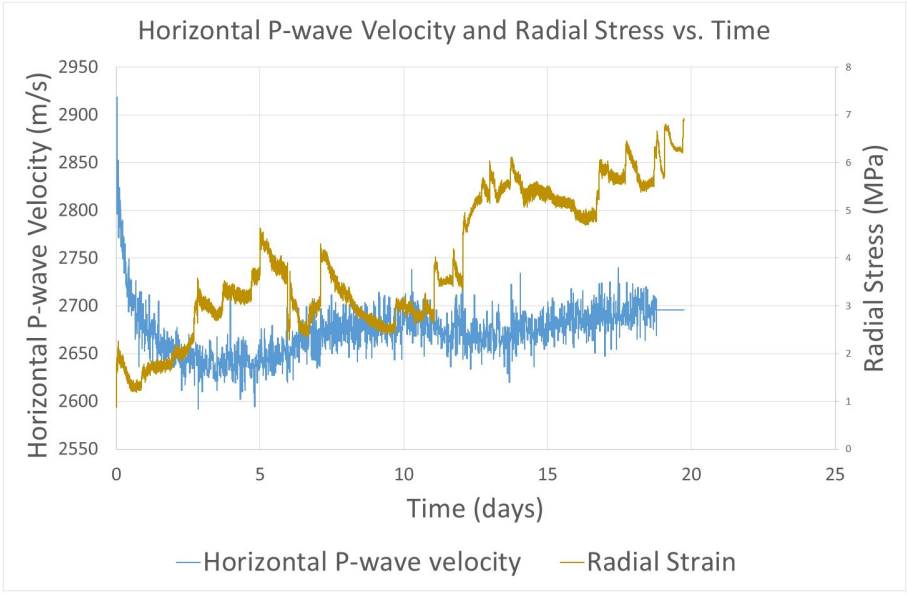

Figure 30: The horizontal P-wave velocity using the axial deformation measurements as reference

Vertical P-wave Test 1

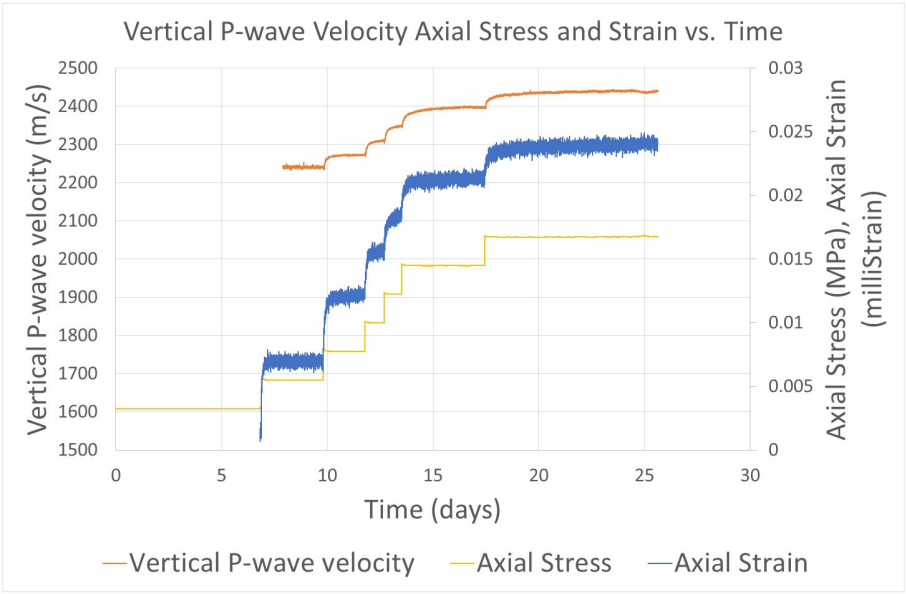

Figure 31: The vertical P-wave velocity from the first test plotted with the axial stress and strain

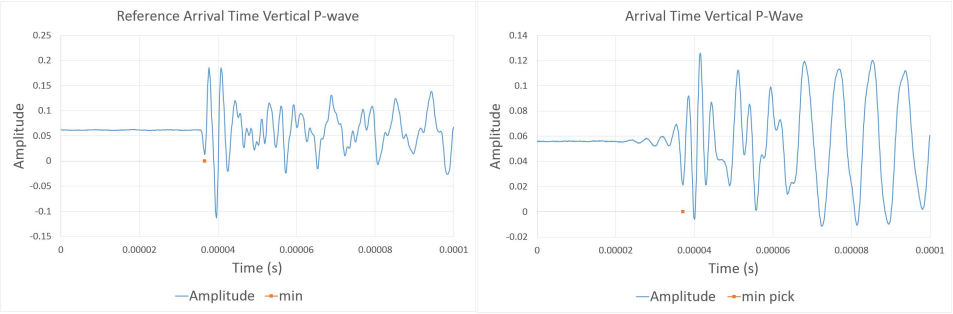

(a) (b)

Figure 32: (a) Reference wave pick of the vertical 500kHz P-wave and (b) an example wave pick of the vertical 500kHz from the first test

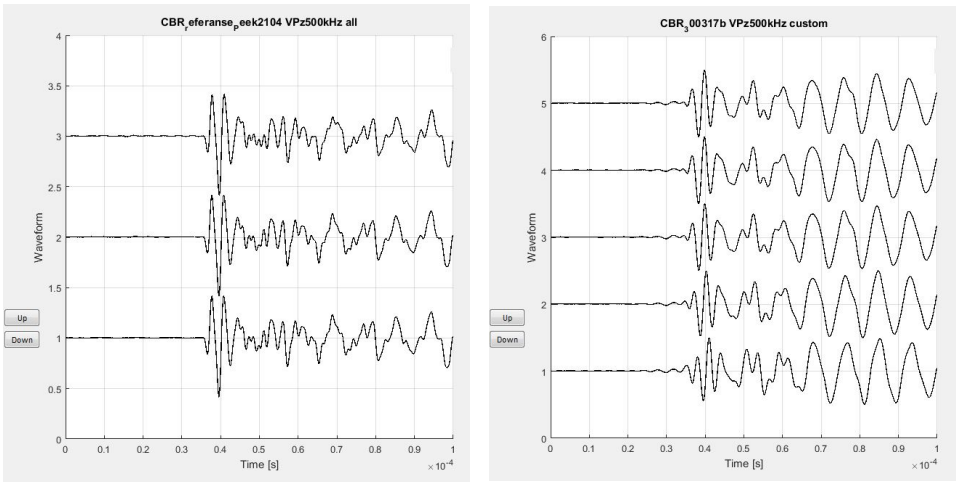

(a) (b)

Figure 33: (a) Reference waveforms of the vertical 500kHz P-wave and (b) example waveforms of the vertical 500kHz from the first test

Vertical P-wave Test 2

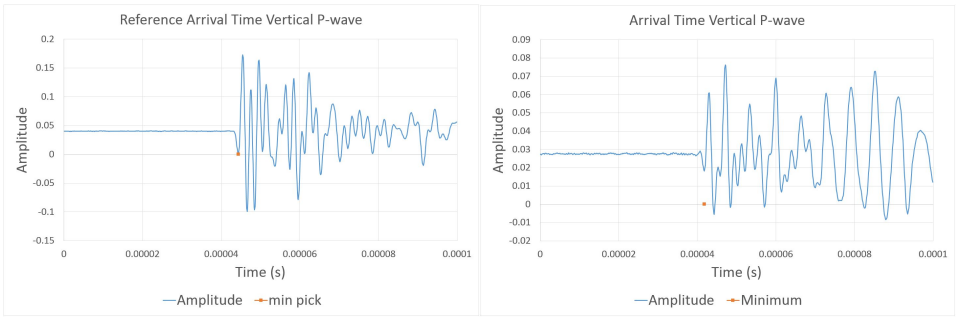

(a) (b)

Figure 34: (a) Reference wave pick VPz 500kHz and (b) Wave pick VPz 500kHz

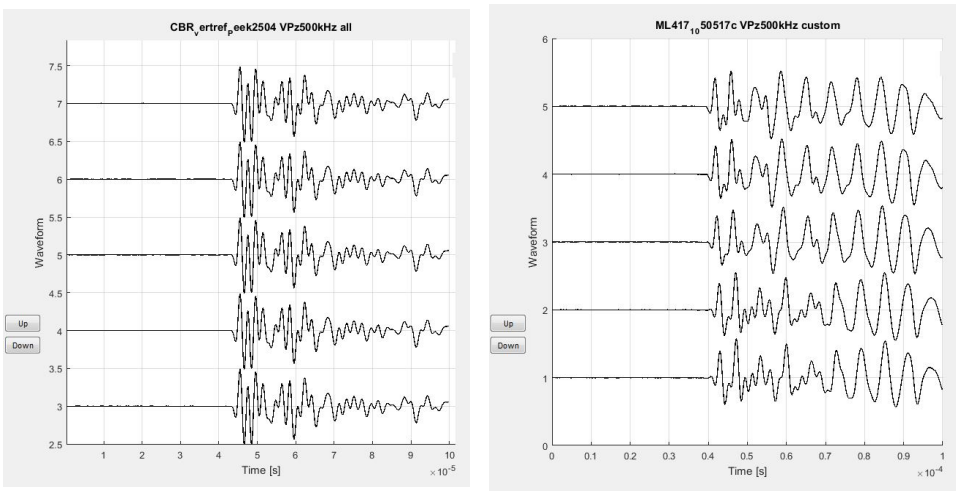

(a) (b)

Figure 35: (a) Reference waveform of the 500 kHz vertical P-wave and (b) shows random waveforms of the vertical 500 kHz waveform from the actual test

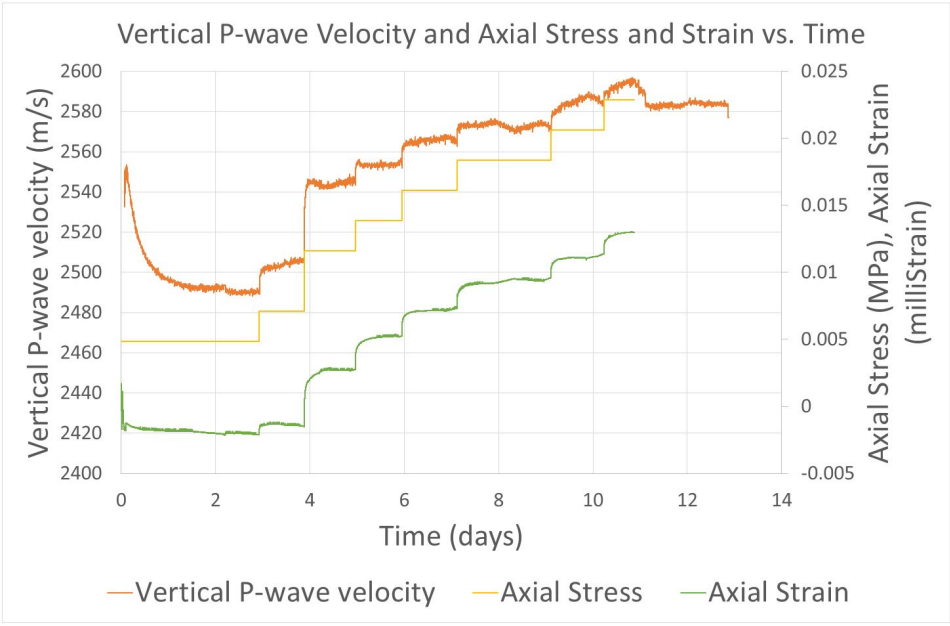

Figure 36: Vertical P-wave velocity using the axial deformation measurements as reference

Vertical P-wave Test 3

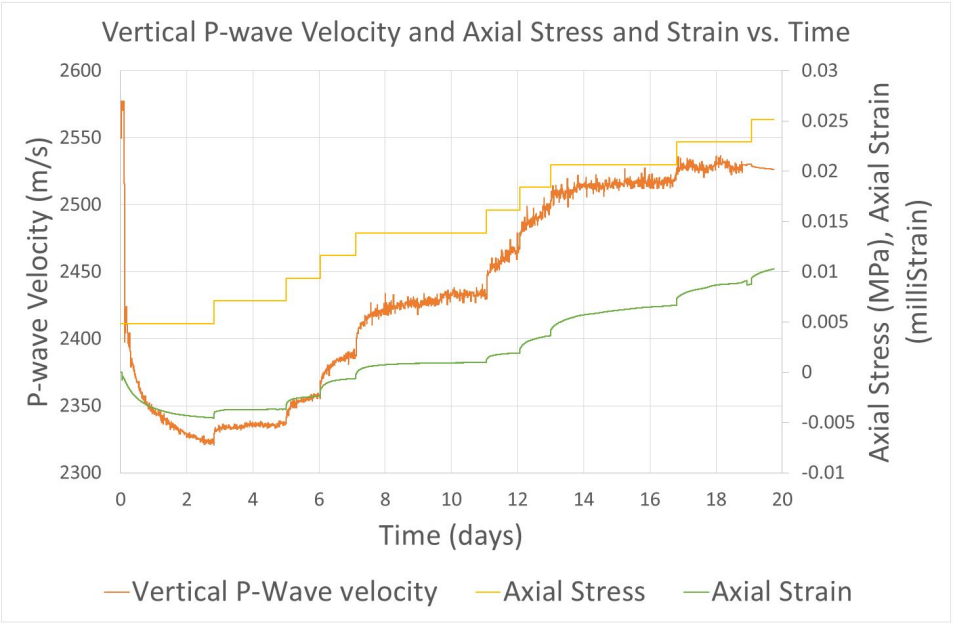

Figure 37: Vertical P-wave velocity of the third test plotted with axial stress and strain.

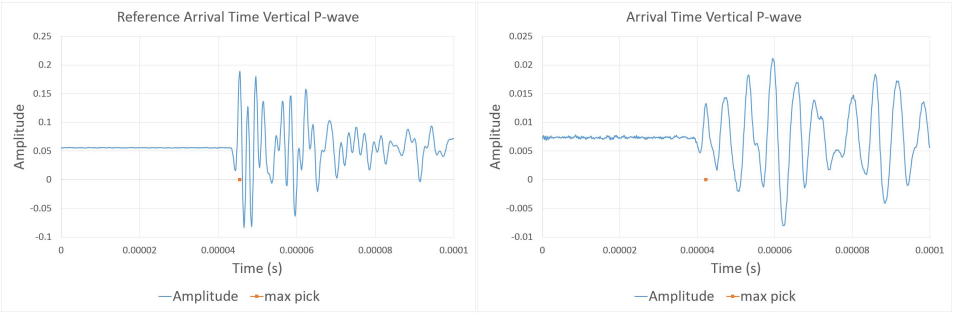

(a) (b)

Figure 38: (a) Reference wave pick of the vertical 500kHz P-wave and (b) an example wave pick of the vertical 500kHz from the third test

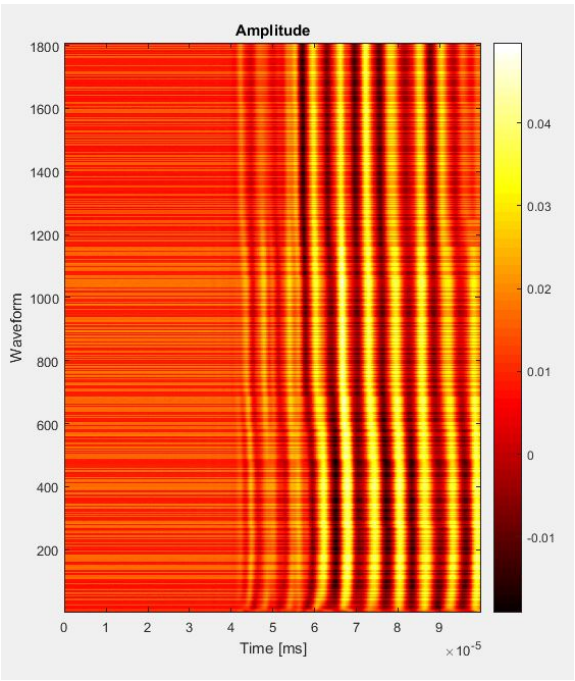

Figure 39: The amplitude of the waveforms of the vertical P-wave signal of the third test.

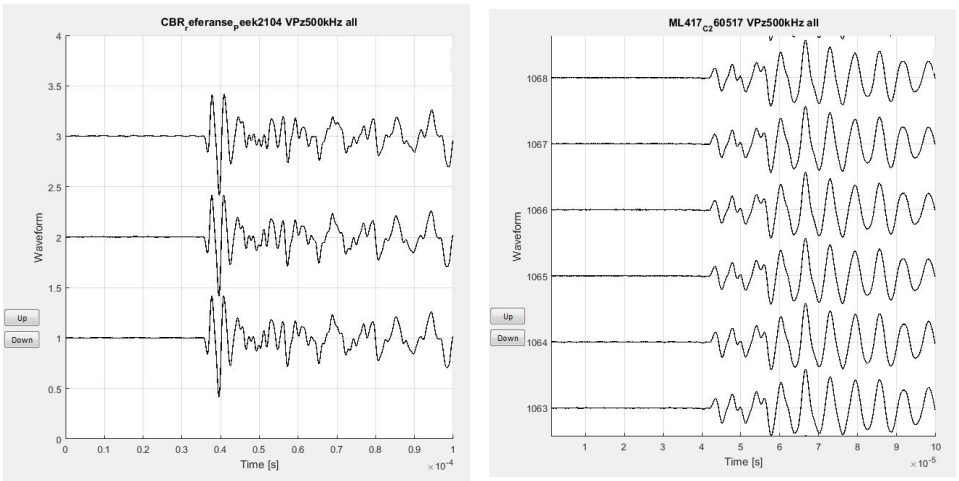

(a) Amplitude Spectrum

(b) Waveforms

Figure 40: (a) Reference waveforms of the vertical P-wave and (b) a selection of waveforms of the vertical P-wave of the third test.

Vertical S-wave Test 1

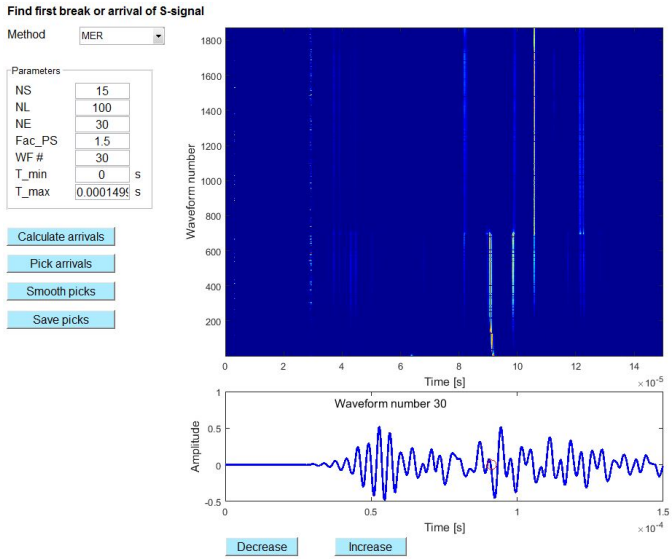

Figure 41: First break or arrival of S-wave analysis performed in Speedy.

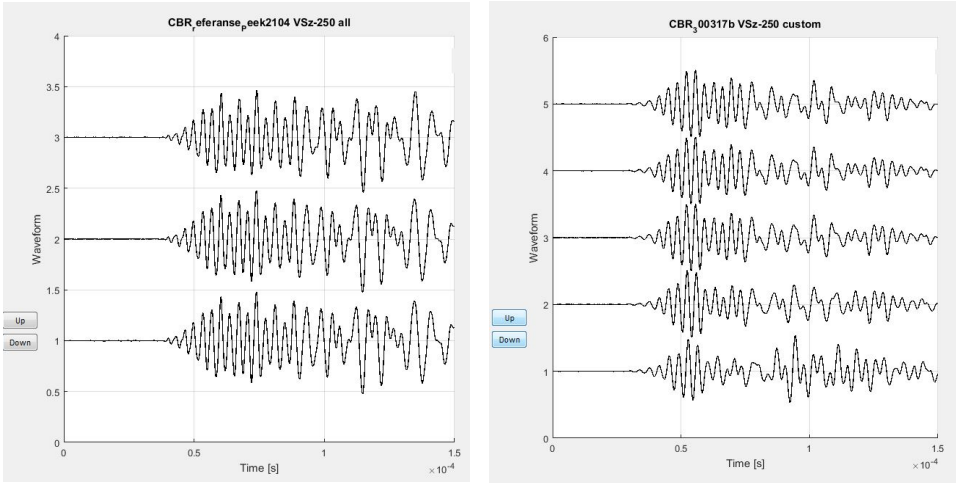

(a) (b)

Figure 42: (a) Reference waveform of the vertical S-wave and (b) a selection of random waveforms of the vertical S-wave of test 1.

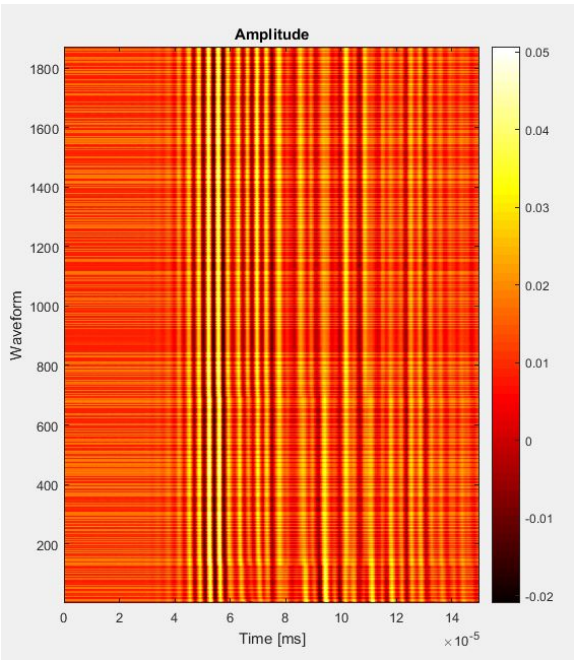

Figure 43: The amplitude spectrum of the vertical S-wave signal recorded.

Vertical S-wave Test 2

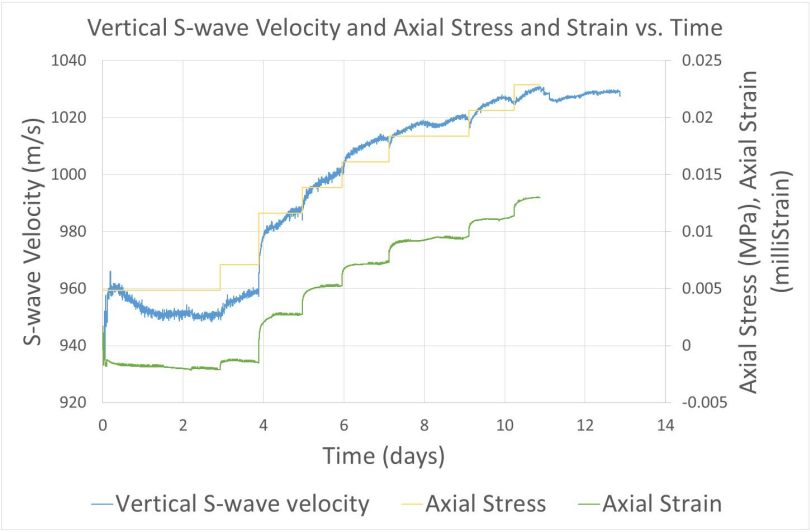

Figure 44: Vertical S-wave velocity for the second test plotted with axial stress and strain.

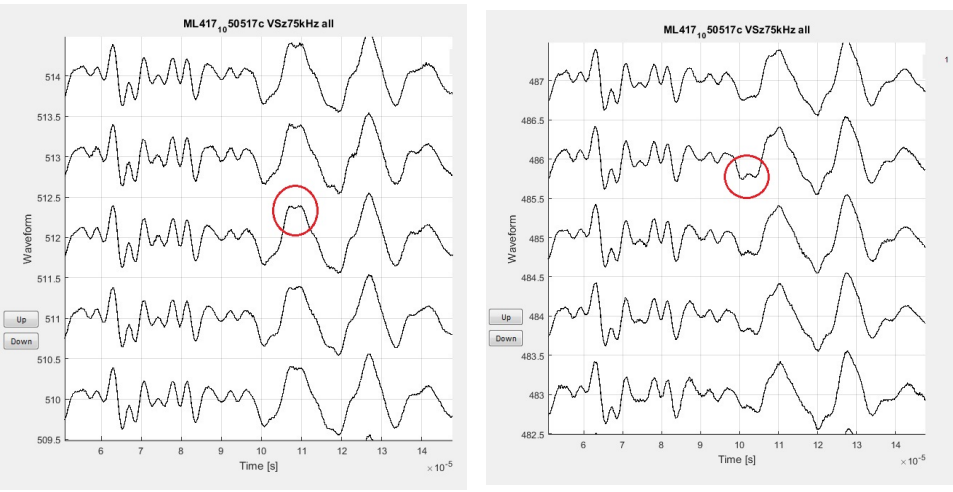

(a) Maximum pick

(b) Minimum pick

Figure 45: Examples of difficult picks for the maximum and minimum first arrival of S-wave of test 2

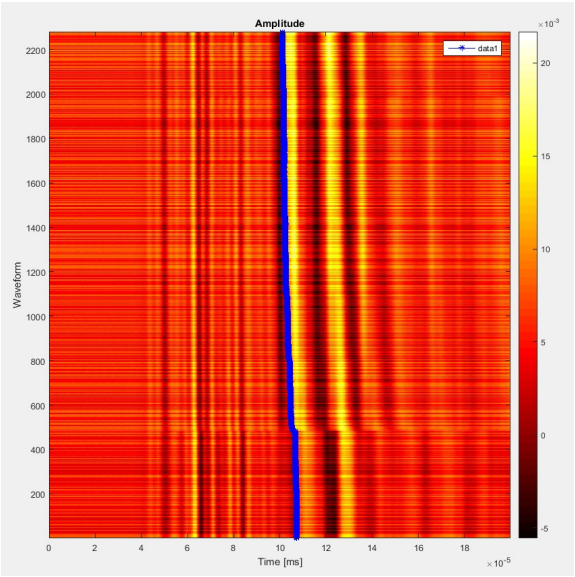

Figure 46: The amplitude of the waveforms of the vertical S-wave and the location of the plotted wave picked for the second test.

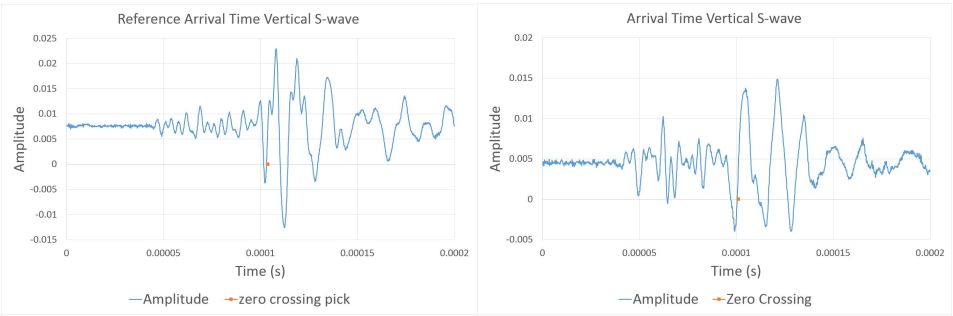

(a) (b)

Figure 47: (a) The wave picked for the S-wave of the reference sample and (b) the S-wave picked for the second test.

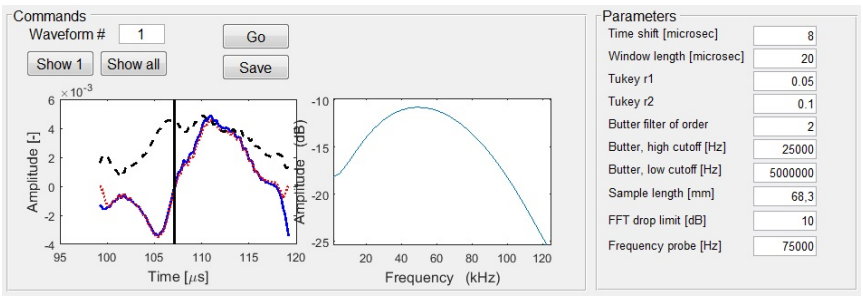

Figure 48: Frequency analysis of the picked S-wave of test 2

Vertical S-wave Test 3

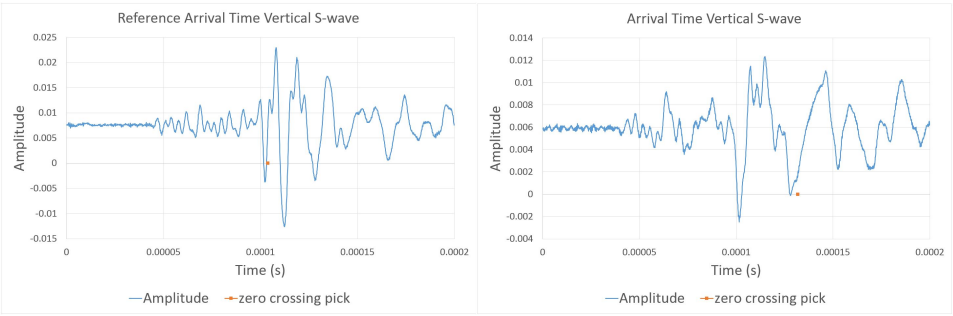

(a) (b)

Figure 49: (a) Reference wave pick VSz 75kHz and (b) Wave pick VSz 75kHz

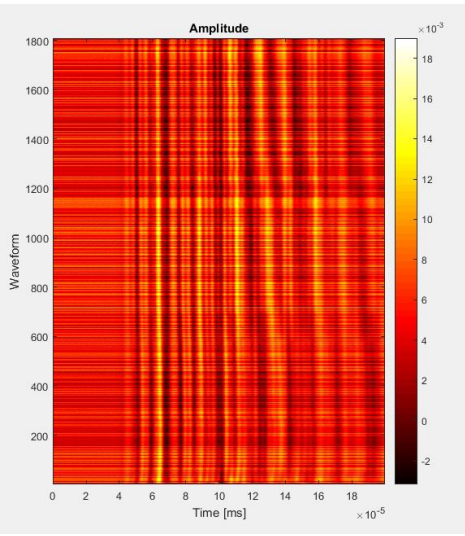

(a) Amplitude

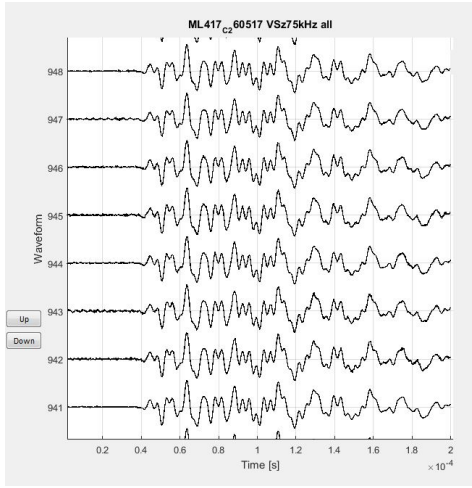

(b) Waveforms

Figure 50: (a) amplitude of waveforms; (b) waveforms of the vertical S-wave.

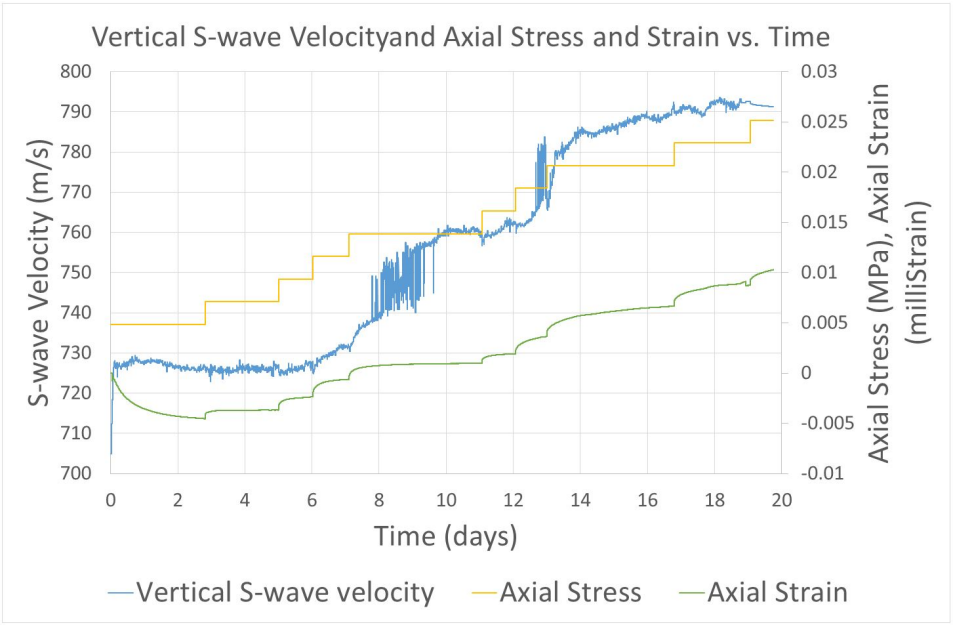

Figure 51: Vertical S-wave velocity using the axial deformation measurements as reference

Young's Moduli

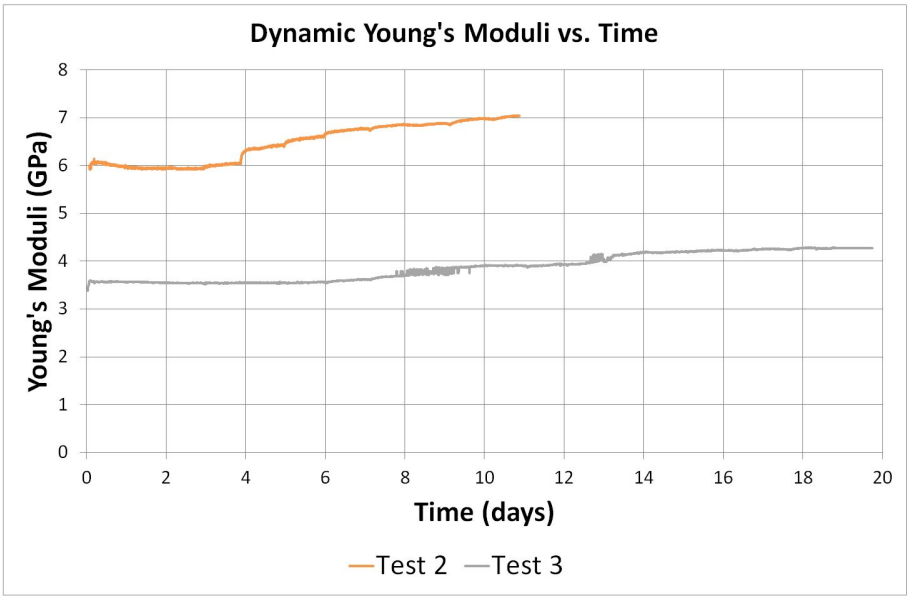

Figure 52: The results of the dynamic Young's moduli.

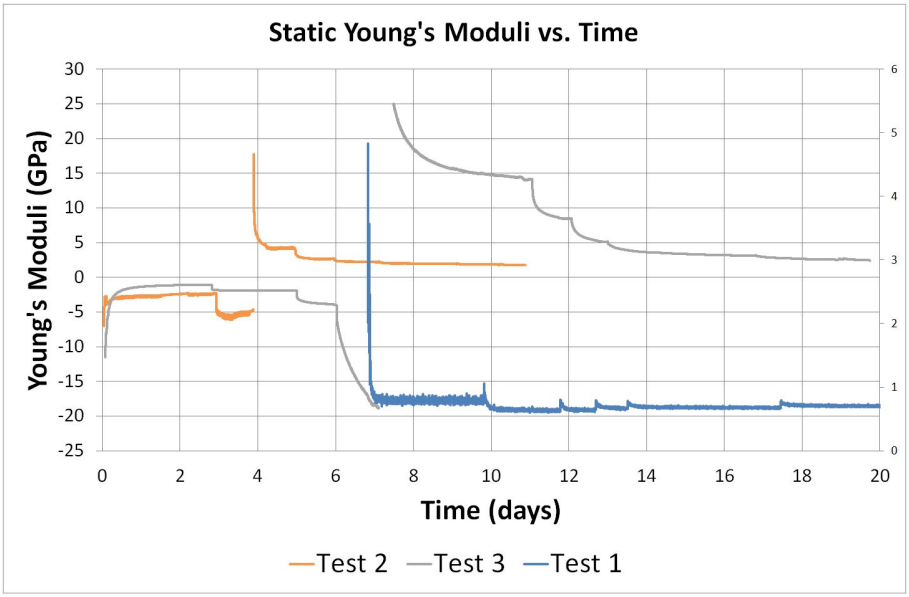

Figure 53: The results of the static Young's moduli.

Dynamic Shear Moduli

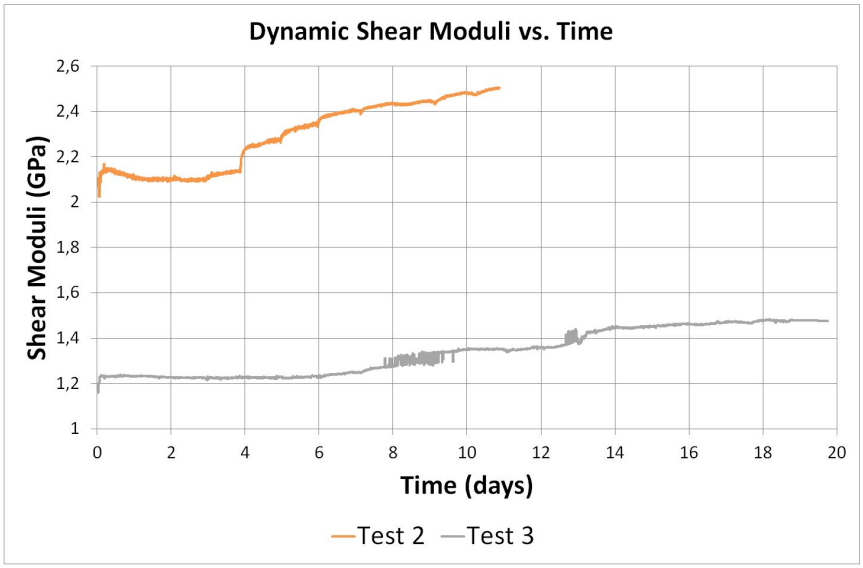

Figure 54: The results of the dynamic shear moduli.

Dynamic Bulk Moduli

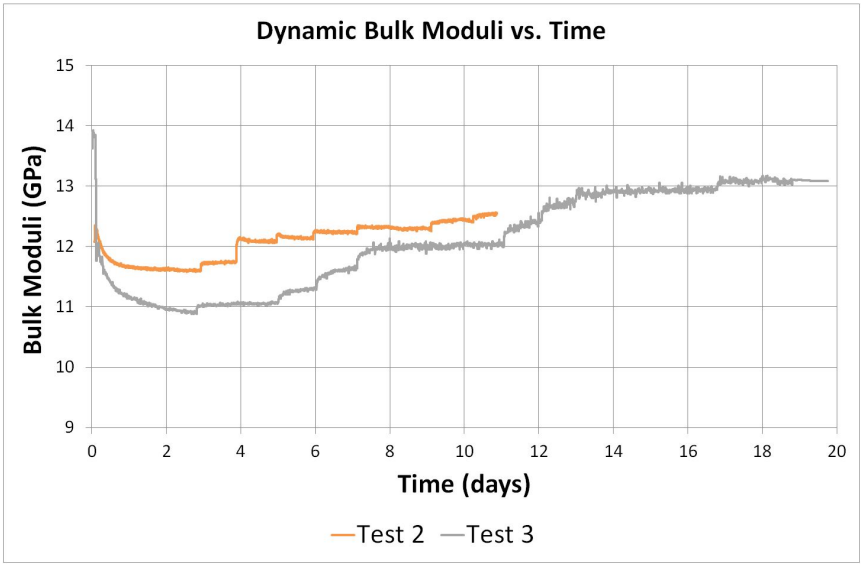

Figure 55: The results of the dynamic bulk moduli.

Vertical Impedance versus Axial Stress

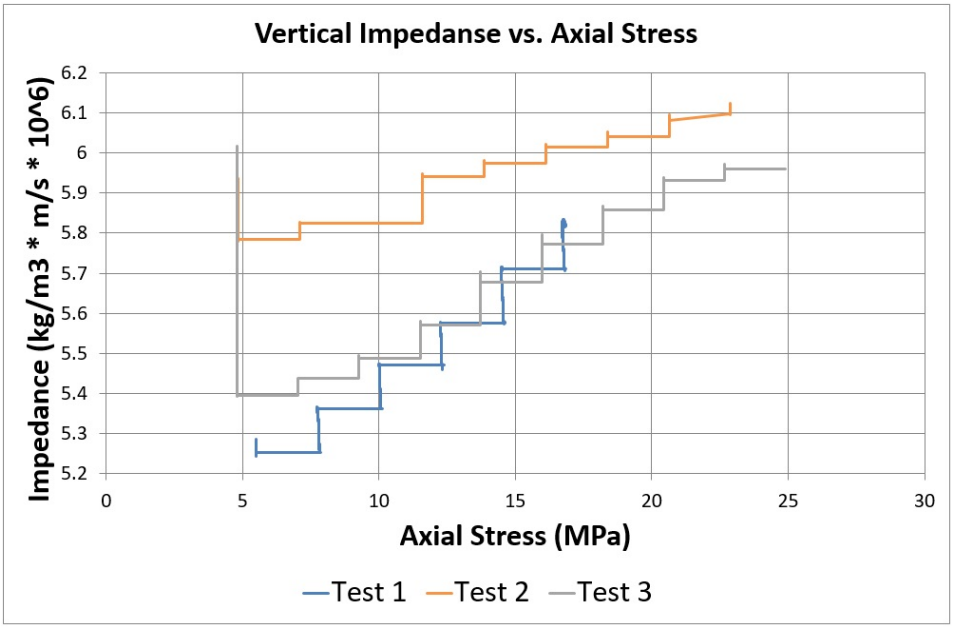

Figure 56: The vertical P-impedance versus axial stress.